UNIVERSITE BRETAGNE SCIENCES LOIRE POUR L'INGENIEUR

UNIVERSITÉ DE NANTES

THESE DE DOCTORAT DE

L'UNIVERSITE DE NANTES
COMUE UNIVERSITE BRETAGNE LOIRE

ECOLE DOCTORALE N° 602
Sciences pour l'Ingénieur
Spécialité : « Energétique-Thermique-Combustion »

Par

« Ketaki MISHRA »

« From the determination of thermal properties of fibers to multiscale modeling of heat transfer in composite »

Thèse présentée et soutenue à « Nantes », le « 09/10/2019 »
Unité de recherche : Laboratoire de Thermique et Energie de Nantes (UMR 6607)
Thèse N° :

Rapporteurs avant soutenance :

Christophe PRADERE Directeur de recherche, I2M CNRS UMR 5295
Chung-Hae PARK Professeur des universités, IMT Lille Douai

Composition du Jury :

Président : Prénom Nom Fonction et établissement d'exercice (9)*(à préciser après la soutenance)*
Examinateurs : Nathalie TRANNOY Professeur des universités, Université de Reims Champagne-Ardenne

Dir. de thèse : Steven LE CORRE Professeur des universités, Université de Nantes
Co-dir. de thèse : Bertrand GARNIER Chargé de recherche, Université de Nantes
Co-enc de thèse : Nicolas BOYARD Chargé de recherche, Université de Nantes

Acknowledgements

Dr. Ketaki Mishra! It still feels like a dream that came into reality due to the various support and appreciations I got throughout my doctoral degree journey.

First and foremost, I want to express my deep appreciation to the members of the jury for accepting to evaluate the thesis work. I thank Chung Hae Park and Christophe Pradere for reviewing this work as the reporter of the thesis dissertation. In particular, Nathalie Trannoy-Orban for chairing the defense of my dissertation works. I thank them for their various remarks, questions, and advice that allowed me to improve the quality of the final work and also the advancements that we can implement in future research.

I would like to thank the director of my thesis, Steven Le Corre, for his guidance and support throughout the time of my thesis. His immense knowledge in solving a scientific problem has always inspired me to give my best to unravel various prospects of the thesis. I want to show an eternal thanks to Bertrand Garnier for his continuous involvement in my thesis and motivating me each day with his warm words and discussions. He has always helped me in overcoming numerous obstacles that we had during our experimental measurements. Many thanks to Nicolas Boyard for his insightful comments and encouragement throughout my Ph.D.

I am also grateful to the members of LTeN, starting with the director of the lab Cathy Castelain for her continuous support. I also thank Brigitte, Christine, Michèle-Anne, and Amandine for their continuous help in the various administrative work. I would like to particularly thank Julien Aubril and Jérôme Delmas for involving their expertise in building the experimental setups that facilitated me finally get beautiful results. A special thanks to Nathalie for her help in my silly computer problems.

The time of my doctoral degree has given me some lovely friends from the lab that I can cherish throughout my life. In particular, I would like to thank Mariam (I didn’t forget), Eliane, Arthur, Juliana, Atin, Rawad, Julien, Rima, Graham, Florian, Violaine and many others for all the fun despite many stressful times. They are the best colleagues that I could ever get. I would also like to thanks many friends who were and are always there for me through all the successes and failures of my life.

Last but not least, I would like to dedicate my Doctoral degree to my lovely family and this degree was impossible without their continuous appreciation and encouragement. Specially Nibedita (my mother and my energy source), Niranjan (my father), Rajib (my love and life partner), Priya (my sister), Sai, Shyam (my nephews), Dulu (my mother-in-law), Gopal (my father-in-law). I am lucky and happy to have them as my support system in all my journeys of life.

Table of Contents

General Introduction…….……..1

Chapter 1: Measurement of axial thermal conductivity for single carbon fibers

1. Introduction 6
1.1 Carbon Fibers 7
2. Literature Review 8
2.1 Thermal conductivity measurement techniques for single fiber 8
2.2 3ω method 13
3. Models for determining fiber thermal conductivity from 3ω response 15
3.1 Analytical Model 15
3.2 Pre-requisites for the validity of analytical model 19
3.3 Numerical Finite Difference Model 20
3.4 Comparison of Analytical and Numerical model 22
4. Sensitivity Analysis 24
5. Experimental Setup and Materials 26
5.1 Experimental Setup 26
5.2 Materials 29
5.3 Specimen Preparation 30
5.4 Measurement Procedure 31
5.5 Temperature Coefficient of Resistance 31
6. Uncertainty Analysis 33
7. Thermal Conductivity Measurements for Single Fiber 33
7.1 Validation with Chromel Wire 33
7.2 PAN Carbon Fibers 35
7.3 Thermal Contact Resistance between sample and copper electrodes 36
8. Partial Conclusions 38
References 40

Chapter 2: Application of the 3ω method to the Radial Thermal Conductivity of single carbon fibers

1. Introduction 45
2. Literature review 45

3. 3ω method **47**
4. Models for determining radial thermal conductivity **47**
4.1 Analytical 1D Radial Model 47
4.2 Numerical Finite Difference 1D Model 51
4.3 Numerical Finite Element 2D Model 53
4.4 Comparison between analytical, numerical 1D and numerical 2D 54
5. Sensitivity Analysis **55**
6. Experimental test for radial thermal conductivity **56**
6.1 Fitting with 1D analytical model 56
6.2 Fitting with 2D finite element model 57
7. Partial Conclusion **59**
References **60**

Chapter 3: Thermal modeling of fibrous composite for estimating effective thermal conductivity tensor

1. Introduction **63**
2. Homogenization **64**
2.1 Mesoscale/Macroscale 64
2.2 Representative elementary volume (REV) and scale separation 64
3. Theoretical Models and Homogenization **66**
3.1 Modeling based on real microstructures 67
3.2 Basic concept of Homogenization and Asymptotic expansions 69
3.3 Effective Thermal conductivity estimation for imposed boundary conditions 71
4. Development of Framework for Effective conductivity tensor calculation **72**
4.1 Geometrical modeling 72
4.2 Boundary conditions 74
5. Results on Square Packed CFRC **76**
5.1 Influence of Length on different Boundary conditions 76
5.2 Representative elementary volume of uniform square cell 79
5.3 Influence of Volume fraction 81
6. Results on Random distributed fibers in CFRC **82**
6.1 Influence of Randomization and Clustering 82
6.2 REV and Homogenization in tapes 83
7. Partial Conclusion **86**
References **87**

Chapter 4: Thermal behavior of tapes in automated tape placement at the scale of fibers

1. Introduction **92**

2. Literature Review on AFP **93**

2.1 Typical AFP process: 93

2.2 Thermoplastic over thermoset matrix: 94

2.3 Temperature driven AFP process: 95

2.4 Literature on thermal modeling of the AFP process: 96

3. Experimental Setup **97**

3.1 Measurement of Average Top Surface Temperature 99

4. Micro-scale numerical modelling on the tapes **100**

4.1 Motivations 100

4.2 Image Processing 101

5. Heat source distribution **104**

6. Numerical model **105**

6.1 Material Properties 106

6.2 Averaging technique for temperature measurement by numerical model 107

6.2 Mesh and Time Convergence 109

7. Results by numerical modeling **110**

7.1 Heat flow by μ-calculation 110

7.2 Temperature variation along the height 112

7.3 Temperature variation of the top surface with time 113

7.4 Influence of rear face contact on temperature measurement on the tops surface 114

9. Partial Conclusion **116**

References **118**

General Conclusion and Perspectives……..…122

Appendices……...……..…127

List of Figures

Figure 1.1: Different textures at the cross-section of a carbon fiber (a) isotropic (b) radial (c) layered (d) onion shaped ----------6

Figure 1.2: Microstructure image by scanning electron microscopy (a) PAN (b) Pitch (c) Rayon precursor----------7

Figure 1.3: Schematic diagram of Angstrom method----------9

Figure 1.4: Schematic diagram of laser flash method----------9

Figure 1.5: Schematic diagram of AC calorimetry ----------10

Figure 1.6: Schematic diagram of T-type probe method ----------11

Figure 1.7: Schematic diagram of periodic heating technique ----------11

Figure 1.8: Schematic diagram of TET method----------12

Figure 1.9: Schematic diagram of the fiber sample with copper holders----------16

Figure 1.10: Schematic diagram for the sample to solve numerical model----------21

Figure 1.11: Numerical and analytical models comparison and effect of convective losses (13.6□m diameter and 1.5mm length of chromel wire)----------23

Figure 1.12: Sensitivity analysis of the V3□ rms to the volumetric heat capacity with varied sample lengths (a) chromel wire (b) FT300B (c) FT800H ----------25

Figure 1.13: Sensitivity analysis of the V3□ rms to the longitudinal thermal conductivity with varied sample lengths (a) chromel wire (b) FT300B (c) FT800H----------26

Figure 1.14: (a) Wheatstone bridge circuit (b) Differential amplifier ----------27

Figure 1.15: Electrical setup for 3ω measurement (a) Schematic (b) Electronic Instruments ---28

Figure 1.16: Variable resistance----------29

Figure 1.17: Block diagram for a LIA ----------30

Figure 1.18: Scanning electron microscopy images for carbon fiber FT300B (a) along the length (b) along the cross-section ----------30

Figure 1.19: (a) Sample holder (b) zoomed image of fiber on the electrode (c) Sample with the electric connector (d) Vacuum chamber----------31

Figure 1.20: Schematic diagram for αemeasurements. ----------33

Figure 1.21: R-R0/R0 vs temperature rise for measuring αe ----------33

Figure 1.22: Measurements for chromel wire with vacuum and atmospheric conditions and fitting with analytical model----------36

Figure 1.23: (a) Measurements for FT300B carbon fiber with vacuum and multiple sample lengths, (b) Measurements for FT800HB carbon fiber with vacuum for a sample length of 1.56mm.----------37

Figure 1.24: Thermal resistance vs length for FT300B ---- 38

Figure 2.1: Simplified schematic diagram of the measurement procedure by Sam Huang et al. 46

Figure 2.2: Illustration of FET Raman method ---- 47

Figure 2.3: Water reservoir used in the thesis of Liang ---- 47

Figure 2.4: Schematic diagram of a fiber in water ---- 48

Figure 2.5: Schematic diagram for numerical model in 1D for the fiber in water ---- 52

Figure 2.6: Geometry for 2D finite element ---- 54

Figure 2.7: (a) V3ω rms at 1Hz with changing the width of the surrounding medium. (b) V3ω rms with frequency for comparing analytical and numerical 1D model with Nnumerical 2d Finite element model. ---- 55

Figure 2.8: (a) Sensitivity analysis of the V3ω rmsvoltage to the radial thermal conductivity with varying kW (b) V3ω rms with frequency for different kR ---- 56

Figure 2.9: Experimental results for FT300B carbon fiber with diameter of 7.3 µm ---- 57

Figure 2.10: (a) Measurements for FT300B carbon fiber with diameter of 7.3 µm (b) Minimization of error between experimental and numerical model for different kR (c) Zoomed region of error for kR between 0.7 – 1.8 Wm-1K-1 ---- 58

Figure 3.1: Multiscale of a fibrous composite……63

Figure 3.2: Schematic representation of homogenization approach d=diameter of the fiber, l= length of REV, L= length of macroscale ---- 65

Figure 3.3: Unit cell approach on small CFRC ---- 68

Figure 3.4: Schematic diagram of embedded cell approach ---- 69

Figure 3.5: Evolution of size of CFRC until REV is determined ---- 70

Figure 3.6: Square packed to random position transformation ---- 71

Figure 3.7: Clustering on vertical position ---- 71

Figure 3.8: Dirichlet boundary condition (a) transversal (b) axial ---- 72

Figure 3.9: Neumann boundary condition (a) transversal (b) axial ---- 72

Figure 3.10: Periodic boundary conditions ---- 72

Figure 3.11: Variation of the effective axial thermal conductivity at different boundary conditions with change in scale division with volume fraction of (a)0.2 (b)0.45 (c)0.6 ---- 73

Figure 3.12: Variation of the effective transversal thermal conductivity at different boundary conditions with change in scale division with volume fraction of (a)0.2 (b)0.45 (c)0.6 ---- 74

Figure 3.13: Temperature gradient on the surface for axial thermal conductivity calculation with (a) small length (20µm). (b) length 100µm (c) length 200µm (c) gradient scaling --- 75

Figure 3.14: Flux on the surface in case of Dirichlet boundar condition ---- 75

Figure 3.15: Variation of the effective axial thermal conductivity at different boundary conditions with the number of fibers at different volume fraction (a) 0.2 (b) 0.45 (c) 0.6 - 77

Figure 3.16: Variation of the effective transversal thermal conductivity at different boundary conditions with the number of fibers at different volume fraction (a) 0.2 (b) 0.45 (c) 0.6 - 77

Figure 3.17: Variation of the effective (a) transversal (b) axial thermal conductivity at different boundary conditions with the volume fraction of fiber. ---------- 78

Figure 3.18: Effect of contrast in thermal property of REV estimation (a) transversal (b) axial thermal conductivity---------- 78

Figure 3.19: Effect of randomization in the fiber position on (a) axial (b) transversal thermal conductvity ---------- 79

Figure 3.20: Effect of clustering of fiber on (a) axial (b) transversal thermal conductivity ------ 79

Figure 4.1: Schematic diagram of AFP process ---------- 88

Figure 4.2: Schematic diagram of the experimental setup ---------- 90

Figure 4.3: Evolution of top surface temperature with time at different points in a tape (a)Solvay (b) Suprem ---------- 92

Figure 4.4: Schematic representation of flux transmission along the contact of tape and bench 93

Figure 4.5: Schematic representation of heating of tape---------- 94

Figure 4.6: Variation of specific heat of the matrix and fiber with temperature. ---------- 95

Figure 4.7: Sample of Solvay and Supreme for optical microscope visualization ---------- 95

Figure 4.8: Microstructure of different section of the Solvay tape (a) Solvay 1 (b) Solvay 2 (c) Solvay 3---------- 96

Figure 4.9: Microstructure of different section of the Suprem tape (a) Suprem 1 (b) Suprem 2 96

Figure 4.10: Hough's algorithm over coins ---------- 97

Figure 4.11: Hough's algorithm over a small section of the tape. ---------- 97

Figure 4.12: (a) Microstructure of Solvay 1 (b) Corresponding mesh ---------- 98

Figure 4.13: Heat source distribution for different microstructure (a) Solvay 1 Frequency and fitting with beta function (b) Different Solvay microstructure (c) Suprem (d) values of x and y for different beta function fitting---------- 99

Figure 4.14: Circular cross section with grids. ---------- 100

Figure 4.15: (a) Cubical geometry for average temperature measurement technic validation (b) Average temperature by Paraview and Grid technique (c) Average temperature on Solvay1 by Grid technique ---------- 100

Figure 4.16: Mesh convergence by estimation of Average temperature at 25ms for different mesh size ---------- 101

Figure 4.17: Temperature and Heat flow in Solvay 2 for (a) 0.5ms (b) 15ms (c) 25ms (d) 50ms (e) Flux lines at 25ms of heating (decreased opacity of the temperature distribution at (c)) (f) Temperature scale---------- 101

Figure 4.18: Heat flow at (a) 0.5ms (b) 10ms (c) 25ms (d) 50ms (e) Heat flux lines showing constriction (f) Temperature scale for the above image ---------- 102

Figure 4.19: Average temperature distribution along y at 25 ms (a) Solvay (b) Suprem ------- 103

Figure 4.20: Comparison of average temperature of the top surface with experimental readings by the Infrared camera (a) Solvay (b) Suprem ---------- 104

Figure 4.21: Influence of RTC over the average temperature of the top surface and comparison with the experimental readings by the Infrared camera ---------- 105

List of Tables

Table 1.1: Literature survey on different methods used for thermal property measurement of carbon fiber…….13

Table 1.2: Longitudinal thermal conductivity and thermal diffusivity values of carbon fiber from literature…..……...13

Table 1.3: Thermal conductivity and heat capacity estimated with and without convective losses……24

Table 1.4: Dimension of the samples used for 3ω measurement……32

Table 1.5: αe for different materials……36

Table 1.6: Thermal properties measured for chromel wire by fitting with the analytical model under vacuum and atmospheric conditions……..36

Table 1.7: Thermal properties estimation for carbon fibers…….37

Table 2.1: Material Properties of fiber and water for the models…….……..54

Table 3.1: Material thermal conductivity……73

Table 4.1: Comparison of properties between thermoset and thermoplastic material……....87

Table 4.2: An overview of mechanism during each step of AFP……88

Table 4.3: Thermal properties implemented in numerical model for fiber, matrix, air and steel…….….95

Nomenclature

α_t	Thermal diffusivity	[m^2s^{-1}]
L	Length of the sample	[m]
Δt	Time step	[s]
$t_{\frac{1}{2}}$	Half rise time	[s]
b_{bundle}	Thickness of the bundle of fiber	[m]
e_{decay}	Decay constant	[-]
f	Frequency	[Hz]
ρ	Density	[kg m^{-3}]
C_p	Heat capacity	[MJ $m^{-3}K^{-1}$]
k	Thermal conductivity	[$Wm^{-1}K^{-1}$]
$\omega = 2\pi f$	Angular frequency	[Hz]
T	Temperature of the sample at position *x* and time *t*	[K]
T_0	Ambient temperature	[K]
I_0	Amplitude of the current	[Amp]
R_0	Electrical resistance of the fiber at T_0	[Ohms]
α_e	Temperature coefficient of electrical resistance	[K^{-1}]
S	Cross sectional area of fiber	[m^2]
$\Delta(x,t)$	Temperature variation from T_o	[K]
$V_{3\omega\, rms}$	3ω root mean square (RMS) response voltage	[V]
I_{rms}	RMS current	[Amp]
h	Heat transfer coefficient	[$Wm^{-2}K^{-1}$]
$\tilde{T}$	Complex expressions of temperature drop	[K]
$\tilde{Q}$	Complex expressions of volumetric power	[Wm^{-3}]
Q	Volumetric power	[Wm^{-3}]
u_P	Unknown parameter	[-]
$X^*_{u_P}$	Sensitivity coefficients of u_P	[-]
R	Resistance at temperature T	[Ohms]
X	Sensitivity coefficient matrix	[-]
W	Variance covariance matrix	[-]
$\sigma_{V_{3\omega\, rms}}$	Variance of measured $V_{3\omega\, rms}$	[-]
σ_{u_P}	Variance of the known parameters u_P	[-]
S_{final}	Matrix of variance and covariance	[-]
k_R	Radial thermal conductivity	[$Wm^{-1}K^{-1}$]
k_w	Thermal conductivity of water	[$Wm^{-1}K^{-1}$]
$\rho_w C_{p\,w}$	Volumetric heat capacity of fiber	[MJ $m^{-3}K^{-1}$]
a	Radius of the fiber	[m]
T_{av}	Average temperature rise	[K]

k	Conductivity tensor of composite	[$Wm^{-1}K^{-1}$]
K^*	Effective thermal conductivity	[-]
	tensor of the composite material	[$Wm^{-1}K^{-1}$]
T^*	Effective temperature	[K]
$\varphi_{x,y,z}$	Local flux fields	[Wm^{-2}]
φ	Average flux	[Wm^{-2}]
v_f	Volume fraction of the fiber	[-]
K_f	Thermal conductivity of fiber	[$Wm^{-1}K^{-1}$]
K_m	Thermal conductivity of matrix	[$Wm^{-1}K^{-1}$]
$K_\perp$	Axial thermal conductivity component of tensor	[$Wm^{-1}K^{-1}$]
$K_\parallel$	Transversal thermal conductivity component of tensor	[$Wm^{-1}K^{-1}$]
Ψ^i	Surface boundaries	[-]
K^*_{axial}	Effective axial thermal conductivity	[$Wm^{-1}K^{-1}$]
$K^*_{transversal}$	Effective transversal thermal conductivity	[$Wm^{-1}K^{-1}$]
p_f	Ratio of shift in the position of fiber to its diameter	[-]
p	Thermal contrast	[-]
e	Thickness of tape	[m]
H	Height of Steel Bench	[m]
Q_{Laser}	Volumetric heat source by the laser	[Wm^{-3}]
β	Beta function	[-]
β_x And β_y	Real number defining the beta function	[-]
T_{avg}	Average temperature of the tape at particular height	[K]

General Introduction

Carbon fiber reinforced composite (CFRC) represent an innovative technological solution for improving and creating more competitive products in various industrial sectors. CFRC stand out for their lightness in weight along with excellent mechanical strength. They are very often an innovative technological solution to improve or create products with more performance in many industrial areas. In advanced fields (nuclear, aerospace, etc.) requiring advanced technologies, high-performance composites are an undeniable asset. They are gradually replacing metals, leading to a continuous and large growth in the demand for the fibrous composite. The last few decades saw the developments of specific processes, especially the automated ones such as automated fiber placement (AFP), which satisfies the need for high production of CFRC with high quality and controlled properties. The quality of the final product depends not only on the behavior of the material at the scale of the composite but also at the scale of individual constituents such as fiber or interface of fiber/matrix and matrix itself. The evolution of the thermal environment of composite structures has an overall impact on the mechanical properties of the products. Therefore accurate thermal characterization of carbon fiber-reinforced composite is extremely crucial to predict its overall quality.

In the present scenario, thermal studies on fibrous composites are gaining the interest of many industries. Each property of the composite, i.e. mechanical/chemical/physical, is strongly dependent on the temperature change. Subsequently, the exact prediction of temperature field is crucial to estimate the overall properties of the final part in a multi-physical approach. Thermal conductivity and volumetric heat capacity are the prime thermal properties in the study of fibrous composite. Moreover, each industry demands a specific role, for example, heat sinks presence at electronic industries or automotive electronic control unit, nuclear fusion reactors require high thermally conductive material contrary to the one used in construction or roof top of automotive with low thermal conductivity. Therefore this further increases the necessity of estimating the thermal property of each component for heat transfer prediction and/or calculation of homogenized property of the composite at the macroscale. In the last few decades, to estimate the effective properties, there is an increased growth in the approaches, experimental or numerical, for thermal property characterization, specifically thermal conductivity of the fibrous composite starting from micro to macro scale.

The basic methodology for thermal conductivity measurement involves solving either steady state or transient heat transfer equation and estimating the thermal conductivity through direct measurement of temperature and/or heat flux. There is a wide research present not only on thermal conductivity but also on heat capacity and diffusivity measurement at the composite scale by methods such as hot guarded plate, flash method, AC calorimetry and many more. However, the challenge of working at the constituent level for CFRC involves the fibers at the scale of 5-8µm, where direct measurement of temperature is very difficult. Besides the thermal conductivity of carbon fiber can vary from 0.1 to 200 $Wm^{-1}K^{-1}$, according to its microstructure. This range of values requires the development of experimental methods for accurate

measurement of thermal properties of a single fiber. The challenge also comes from the anisotropy in the thermal conductivity of fibers. Few studies have systematically and accurately measured the thermal property for single fiber such as 3ω method, periodic heating technique, T-type probe heating method and AC calorimetry method. However, the radial thermal conductivity of the fiber is still a huge challenge to be fulfilled. Therefore, an experimental approach for the accurate measurement of thermal property encountering for the anisotropy is of significant importance.

Furthermore, at the level of fibrous composite, the effective thermal property estimation is achieved through the numerical approach. In this method, to retrieve an internal microstructure that acts as the representative elementary volume (REV) at mesoscale remains an important research issue. This REV should mimic the thermal response of macroscale CFRC, where the required property is constant beyond this volume. Thus solving the partial differential equations on a strongly spatial heterogeneous medium using numerical approaches and then detecting the continuum at which the effective properties are constant is of high importance. Thus, the effective thermal property at the scale of REV can predict the thermal behavior of the composite.

A direct application of the effective property estimation is on the thermal study of a prepreg tape placement process such as AFP in making complex shapes from CFRC. A prepreg tape is a laminating pre-engineered material (fibers are pre-impregnated by the polymer matric, thermoset or thermoplastic) for the manufacturing CFRC at macroscale. In the AFP process, the prepreg tape is heated at high speed by a laser and then subsequently pressed and cooled for bonding with the previously placed tape. This process involves many sub phenomena such as fusion, crystallization, void growth and etc. Each of these involved steps are extremely thermal driven, therefore exact temperature prediction at the scale of a single tape is important as this will ultimately influence the interlayer bonding and ultimately the strength of the laminate.

Commercial thermoplastic tapes are composed of PEEK matrix that acts as semi-transparent material and AS4 carbon fiber that is opaque to the infrared wavelength. The microstructural images of such mesoscale CFRC have shown an intrinsically different distribution of the fibers. Therefore the investigation of REV at the scale of the tape is also very important. Previous research works widely based on the primary assumption of tapes acting as a homogenous material leading to the surface with laser heat projection having the highest temperature. It is crucial to verify this assumption for the exact prediction of the temperature in tapes. This can assist in a thorough quality assessment of the laminate after AFP manufacturing.

In this thesis, the objective starts with the thermal characterization of single carbon fibers at the microscale. Although the interface of matrix/fiber is also important, it's currently out of the scope of this thesis. The study of some REVs behavior is equally essential in order to understand the impact of local parameters on the global thermal response at the mesoscale.

Thus, the central objectives of this thesis are:

- At the microscale, the measurement of longitudinal and radial thermal conductivity and volumetric heat capacity of commercial PAN fibers using 3ω method.
- At the mesoscale, the effective thermal conductivity tensor calculation of fibrous composite and the analysis of the effects of fiber distribution.
- In an advanced manufacturing technique, AFP, the influence of microstructural heterogeneities (fiber distribution, thermal contact resistance) on the thermal behavior at the scale of single fiber.

The manuscript is divided into four chapters, each contributing to one of the above mentioned points along with the literature reviews. Chapter 1 focuses on using 3ω method for simultaneous measurement of longitudinal thermal conductivity and volumetric heat capacity for single fiber. Chapter 2 concentrates on extending the applicability of the 3ω method for radial thermal conductivity measurement by implementing the results from the previous chapter. Chapter 3 is dedicated to the determination of the REV for a mesoscale fibrous composite and estimating the effective thermal conductivity. The presence of REV is verified for commercial tapes, such as Solvay and Suprem, which are crucial as advanced manufacturing technique like automated fiber placement (AFP). Chapter 4 investigates the thermal behavior of these composite tapes, during the AFP process. Each tape has a different distribution of fiber in the microstructure. Thus it helps to understand the influence of fiber distribution or the contact zones between tapes or with metallic substrate on the temperature prediction for each tape.

Chapter 1

Measurement of axial thermal conductivity for single carbon fibers

1. Introduction **6**
2. Literature Review **8**
2.1 Thermal conductivity measurement techniques for single fiber 8
2.2 3ω method 13
3. Models for determining fiber thermal conductivity from 3ω response **15**
3.1 Analytical Model 15
3.2 Pre-requisites for the validity of analytical model 19
3.3 Numerical Finite Difference Model 20
3.4 Comparison of Analytical and Numerical model 22
4. Sensitivity Analysis **24**
5. Experimental Setup and Materials **26**
5.1 Experimental Setup 26
5.2 Materials 29
5.3 Specimen Preparation 30
5.4 Measurement Procedure 31
5.5 Temperature Coefficient of Resistance 31
6. Uncertainty Analysis **33**
7. Thermal Conductivity Measurements for Single Fiber **33**
7.1 Validation with Chromel Wire 33
7.2 PAN Carbon Fibers 35
7.3 Thermal Contact Resistance between sample and copper electrodes 36
8. Partial Conclusions **37**
References **39**

1. Introduction

In the mid-20th century, the interest in carbon fibers was transformed when synthetically produced rayon were carbonized to produce carbon fibers for high thermal stress applications such as missiles[1]. In the current engineering scenario, carbon fibers reinforced composite have found a great place in many high performance industries such as aeronautics, automobile, textile and etc. These high technology industries require a deep knowledge of all the physical phenomena occurring in the composites at micro to macroscale. A huge stack of research is present in the characterization of mechanical properties for the composites but rather less focus was given on the thermal properties. There has been a huge number of research works going on for developing different techniques for measuring the thermal properties such as thermal conductivity, thermal diffusivity and heat capacity at different scales[2–5]. For better thermal design of any phenomena involving fibrous composite, it is necessary to concentrate in measuring the effective properties, which is possible by the correct estimation of each properties at micro scale.

The objective of this chapter concentrates on the measurement of axial thermal conductivity and volumetric heat capacity for a single carbon fiber. In the literature, there are few methods present on bundle of fibers such as laser flash method [6] or Angström method [7], or through single fiber such as T-type probe method [8] or AC calorimetry technique[9] which are described briefly in section 2.

In this thesis, 3ω method is used for estimation of axial thermal conductivity and volumetric heat capacity of the single fiber where the fiber itself acts as heater and sensor resulting in minimum uncertainty. It is a frequency based approach where an alternating current is passed through the sample and the resulting voltage fluctuations with frequency contains the information on thermal properties. A detailed description of the method is portrayed in the upcoming sections. A classical analytical model (section 3.1) is already present in the literature [10] which was used to retrieve the thermal properties of fiber by fitting the experimental data. But it comes with few assumption and pre-conditions (section 3.2) to satisfy the eligibility of analytical model to be successful. A numerical model taking into account lateral heat loss (section 3.3) is developed. Apart from this, previous research works on 3ω method for fiber thermal conductivity measurement has only focused on the implementation of separate analytical models in lower and higher frequency range for estimation of either thermal conductivity or heat capacity. Therefore in this thesis a sensitivity analysis (section 4) of the measured voltage with respect to the unknown parameter over a wide frequency range (10^{-2} -10^{4} Hz) is presented. It can help in fulfilling the objective of using single analytical model for the estimation of both axial thermal conductivity and volumetric heat capacity. In section 5, the experimental setup for 3ω method is presented in details along with the uncertainty in the measurement (section 6). Lastly, this 3ω method is used for estimation of the thermal conductivity and volumetric heat capacity of a chromel wire for validation purpose (section 7.1) and two types of PAN-based carbon fibers (section 7.2) and the effect of thermal contact resistance between sample and its holder is discussed in section 7.3.

1.1 Carbon Fibers

Carbon fibers are basically made up of small graphite crystallites where the atoms at each layer are clinched with each other by a strong covalent bond. The layer itself exhibits a weak van der Waals force. The alignment of each layer decides the strength and modulus of the final carbon fiber (Figure 1.4). The intermolecular bonding varies depending on the precursor, which is the main classifying factors for different types of fiber. Different precursors used in large scale production are poly-acrylonitrile (PAN), rayon and pitch based. These precursors are carbonized to get the final form of different fiber types (Figure 1.5). Depending on the nature of the precursor used, the texture of the atomic planes has a range and a variable orientation that govern their properties.

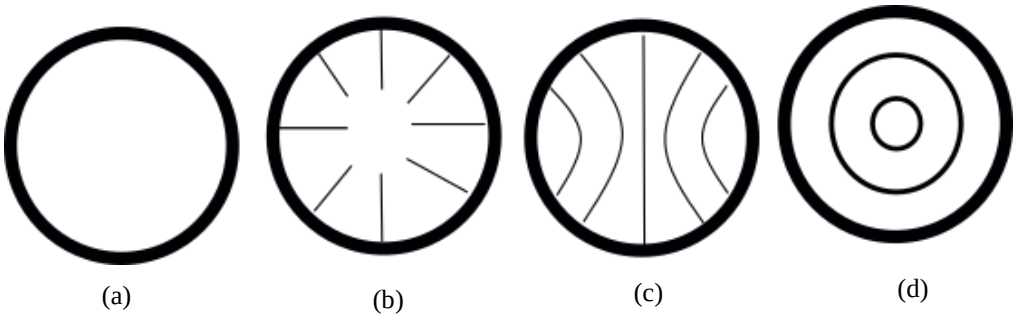


Figure 1.1: Different textures at the cross-section of a carbon fiber[11] (a) isotropic (b) radial (c) layered (d) onion shaped

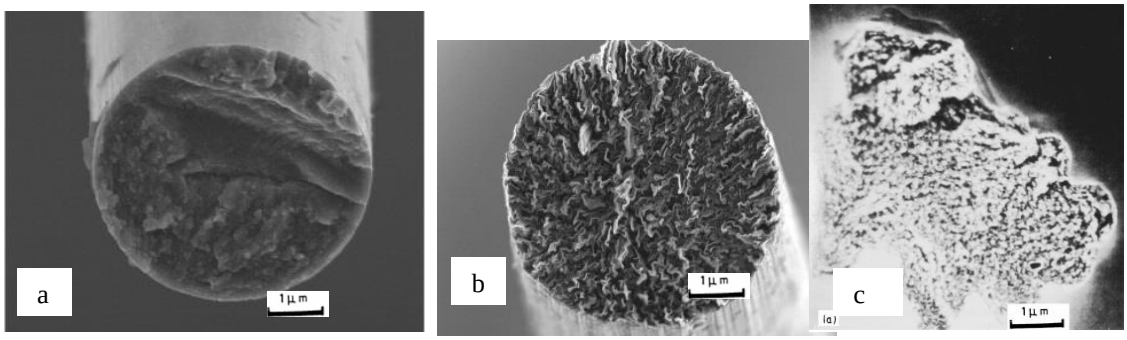


Figure 1.2: Microstructure image by scanning electron microscopy (a) PAN (b) Pitch (c) Rayon precursor [1]

The carbon fibers are produced in different conditions from different precursors, but the basic steps are the same. This involves the pyrolysis of stabilized precursor fibers, which are produced by oxidizing the precursors in the air at 200-400°C. These stabilized fibers are passed through treatment at a high temperature of 1000°C in an inert atmosphere. This step is known as carbonization where it removes nitrogen, oxygen, hydrogen and other elements that are non-carbonic. They are further treated at 3000°C to increase the carbon content and achieve higher Young's modulus. This produces carbon with a relatively inert surface, which is later post treated to help in the adhesive capacity of these fibers to the matrix [12].

Carbon fibers from different precursor exhibit different properties. Even though the production cost of PAN-based fibers is higher than the rayon, however PAN display twice the

carbon yield in comparison with the rayon based. The pitch-based carbon fibers could produce a higher tensile modulus fiber, but higher strength of the PAN fibers lead to the growth in the interest of multiple industrial on PAN precursor. Therefore currently PAN-based carbon fibers are the dominating precursor that is being used 96% of the overall carbon fiber market[13].

2. Literature Review

The general concept behind the measurement of thermal properties involves the observation of temperature response to any change in the boundary condition. As this change results in a disequilibrium in the system and the attempt of the particular system to come back to equilibrium contains the information for the thermal properties. But the estimation of thermal conductivity for a single fiber comes with lots of difficulties such as the small size, uncertainty, influence of any external disturbance and many more. In the past three decades, researchers have done many attempts for measuring the thermal conductivity, mostly axial thermal conductivity of the fiber. The studies can be grouped with samples made of bundle of fibers or a single fiber, steady or unsteady state measurements.

2.1 Thermal conductivity measurement techniques for single fiber

In this section, the techniques that are widely intriguing in the community of researcher for measuring the axial thermal conductivity are being discussed. Table 1 shows various techniques in nutshell along with the heating method, detection techniques, samples that are being used.

Method	Heating Method	Temperature sensor	Sample Type	Reference
Angström Method	Constant DC current heater (Joule Heating)	Thermocouples	Fiber Bundle	[7]
Laser Flash Method	Short Laser Pulse	IR sensor	Fiber Bundle	[6]
Thermal Potentiometer	Constant DC heater (Joule Heating)	Thermocouples	Fiber Bundle	[7]
AC Calorimetery	Halogen Lamp	Thermocouple	Single Fiber	[9]
T-Type Probe Method	Constant DC heater (Joule Heating)	Hot wire	Single Fiber	[8]
Periodic heating technique	Argon Laser Beam	IR sensor	Single Fiber	[14][15]
Transient electro thermal method	Constant DC heater (Joule Heating)	Sample dependent	Single Fiber	[16]
3ω Method	AC power supply heater (Joule Heating)	Sample dependent.	Single Fiber	[10]

Table 1: Literature survey on different methods used for thermal property measurement of carbon fiber

Carbon Fiber	Commercial Reference	Therm. Cond/W $m^{-1}K^{-1}$	Therm. Diff/mm^2s^{-1}	Temp. range/K	Method	Reference
PAN Based	IM7	-	7.48	RT*	Laser flash	[6]
	M55J	-	81.15	RT	Laser flash	[6]
	UKY	-	5.91	RT	Laser flash	[6]
	PANEX 33	-	15-20	850-1250	Periodic heating	[15]
	AS4	6.5	-	RT	3ω Method	[11]
	IM10	6.9	-	RT	3ω Method	[11]
Pitch Based	K1100	-	415.17	RT	Laser flash	[6]
	P100	-	85-45	750-1875	Periodic heating	[15]
	-	490	-	RT	T-type	[7]
Rayon Based	TC2	5-12.5	-	850-1800	Periodic heating	[15]
Lignin Based	-	0.1-2.63	-	10-300	Transient electro thermal technique	[16]

Table 2: Axial thermal conductivity and thermal diffusivity values of carbon fiber from literature. (*RT= Room temperature)

Table 2 shows the type of fiber that are being used and the range of the axial thermal conductivity that has been measured by different methods described below.

- Angström method: In Angström method, the fiber is periodically heated and it uses the decreasing temperature wave amplitude with the distance to measure the thermal diffusivity of the sample (fiber bundle). A function generator is used as heat source with thermal wave at one end of the sample. At two different locations on the sample, the temperature is measured either by thermocouple or infra-red temperature sensors. The temperature difference measured at these two points at different lengths from the source ($\Delta T_1, \Delta T_2$) and the thermal time delay Δt from wave reaching from one point to another one with a gap of L will contain the data for thermal diffusivity[7]. Figure 1.3 helps us in understanding the basic concept of this method[17].

$$\alpha_t = \frac{L^2}{2\,\Delta t \ln(\Delta T_1/\Delta T_2)} \tag{1.1}$$

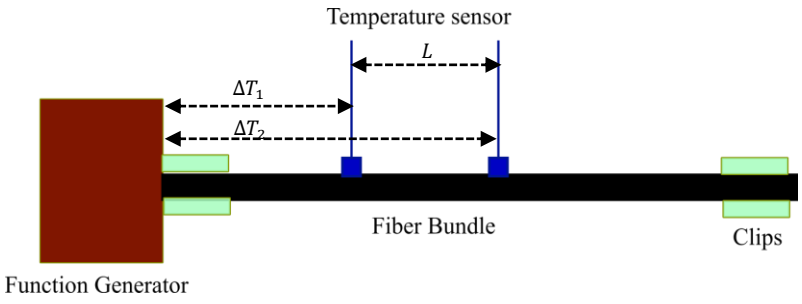


Figure 1.3 ***Schematic diagram of Angström method***

• Laser flash method: The laser flash analysis is a time dependent method. In this method a sample, i.e., a bundle of fiber with a thickness of b_{bundle}, placed in a temperature and atmosphere controlled environment (Figure 1.4). One side of the sample is subjected to sudden burst of heat from a short laser pulse and infra-red sensors are placed to monitor the temperature as a function of time. The time taken for the cold face to have a rise of half the equilibrium temperature i.e. the half rise time ($t_{1/2}$) contains the information about thermal diffusivity and then the thermal conductivity can be measured by knowing the heat capacity and density[6].

$$\alpha_t = 0.1388 * b_{bundle}^2 / t_{1/2} \tag{1.2}$$

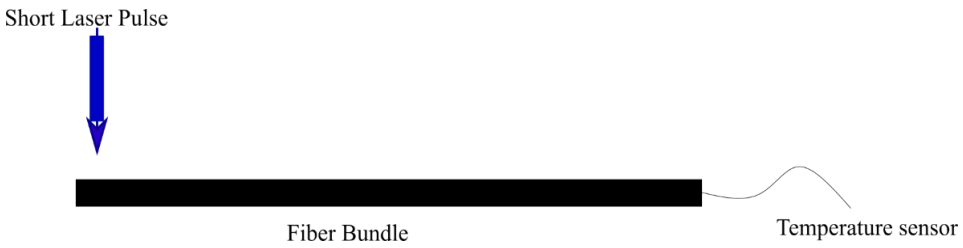


Figure 1.4: Schematic diagram of laser flash method

• AC calorimetry: This method was classically used for measurement of thermal diffusivity for thin films[18][19]. Later on it was implemented for the measurement of thermal diffusivity of a single fiber. In this technique, an oscillatory heat flux is projected by a tungsten halogen lamp at frequency f on one section of the sample and ultimately generation of AC temperature wave passing to the other section of the sample that is not being heated by the lamp. This results in decay of the AC temperature wave amplitude which can be represented by decay constant (e_{decay}), which contains the data about the thermal diffusivity of the fiber[9]. The heat capacity was measured externally with the help of differential scanning calorimeter and then later the value of thermal conductivity for that particular fiber was extracted using.

$$\alpha_t = \pi f / e_{decay} \tag{1.3}$$

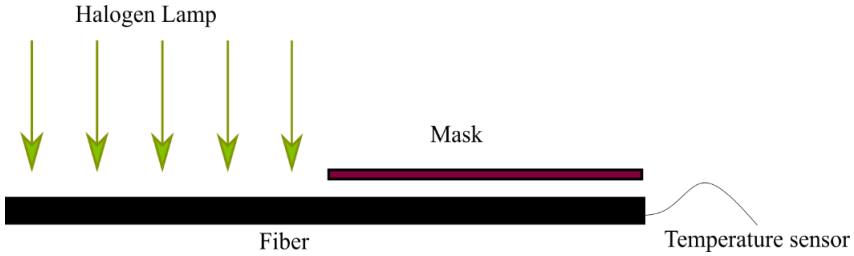


Figure 1.5: Schematic diagram of AC calorimetry

• Thermal potentiometer: It is a steady state method which aims to set up a uniform temperature gradient throughout the sample (fiber bundle). Similar to the guarded hot plate method a set of guard heaters are used to minimize heat losses by convection and

radiation from the sample heater and the thermocouples and thus maintaining the sample with a uniform temperature gradient. The heating of the sample by the heat supply will set up a thermal gradient within the sample which is then measured by thermocouples at different locations on the sample. These data along with the knowledge of power dissipation and cross sectional area of the sample is used to calculate the thermal conductivity of the sample. Although it has the ability of measuring thermal conductivity at various temperature[7] but the main drawback of this method is the time taken to obtain a measurement as we need to wait for the thermal gradient to become uniform.

- T-type probe method: It is a steady state where a hot wire placed between two heat sinks is used as both a constant heat source as well as a thermometer. Figure 1.6 shows the basic principle behind T-type probe technique[8]. A hot wire is carefully selected with its electrical and thermal properties being known and an electric current is sent through it. It tends to have a parabolic temperature profile with maximum value at the center of the wire. The sample is then placed in the middle of the hot wire with another end of the sample attached to another heat sink. The temperature profile in the hot wires is changed due to the disruption in heat flow by the fiber in contact. In the article of Wang et al., he explained how this change in the temperature profile of the wire from the initial case of without the fiber contain the information about the thermal conductivity of the fiber [20][21]. The equation for deriving the thermal conductivity of the fiber is as follows:

$$k = \frac{l_f l_h k_h S_h (l_h^2 IV - 12 l_h k_h S_h \Delta T_l)}{l_{h1} l_{h2} S_f (12\, l_h^2 k_h S_h \Delta T_l - IV(l_{h1}^3 + l_{h2}^3))} \tag{1.4}$$

Where subscript f denotes for fiber and h denotes for hot wire, l is the length, S is the cross section area, I is the current and V is the voltage, ΔT_l is the changed temperature rise in the hot wire due to fiber. Issues tend to arise when measuring conductivities of thin individual fibers projected to high temperature of heat since they are susceptible to large heat losses in the form of convection and radiation.

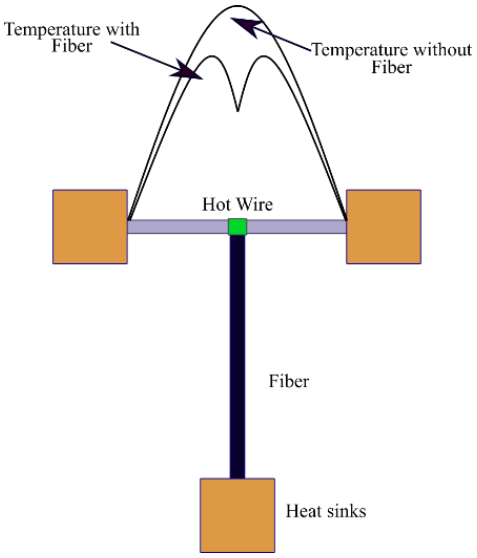


Figure 1.6: Schematic diagram of T-type probe method

• Periodic heating technique: In the article of Pradere[22][14], a frequency dependent periodic technique was used to measure the thermal conductivity of individual fibers (Figure 1.7). The single fiber of type PAN, pitch, rayon based, is initially heated by Joule effect and then an Argon laser beam is projected on the surface of the fiber and which results in periodic thermal excitation. With the help of a lens, a splitting prism and an objective, the laser beam is focalized on such small surface of the fiber. The temperature response is analyzed by an IR sensor. The phase shift between the++ and the magnitude of the response can be measured by the lock-in amplifier at multiple frequencies and position of the sensor. The modulated part of the signal contains the data related to diffusivity. A 1D direct analytical model was developed for the experimental setup giving the fluctuating part of temperature$\Delta\tilde{T}$ and phase$\emptyset$ as

$$\log\left(\Delta\tilde{T}\right) = -\gamma_r \hat{z} + \log(K_1 \Delta T_s) \quad (1.5)$$

$$\emptyset = -\gamma_i \hat{z} + arctg\left(\frac{1 + K_2 K_3}{K_2 - K_3}\right) \quad (1.6)$$

Where $\gamma = \sqrt{\frac{h_0 p}{kS} + i\frac{\omega}{a}} = \gamma_r + \gamma_i$ and K_1, K_2, K_3 are different functions of γ_r and γ_i. h_0 is heat losses coefficient, p is the perimeter, S is the surface area of fiber, k is the thermal conductivity, $\omega = 2\pi f$. Different minimization approaches were used to estimate the value of thermal diffusivity. In another article[23], similar experimental setup was used to solve the value of heat capacity. Through the data of diffusivity and heat capacity, the thermal conductivity of different fiber was estimated.

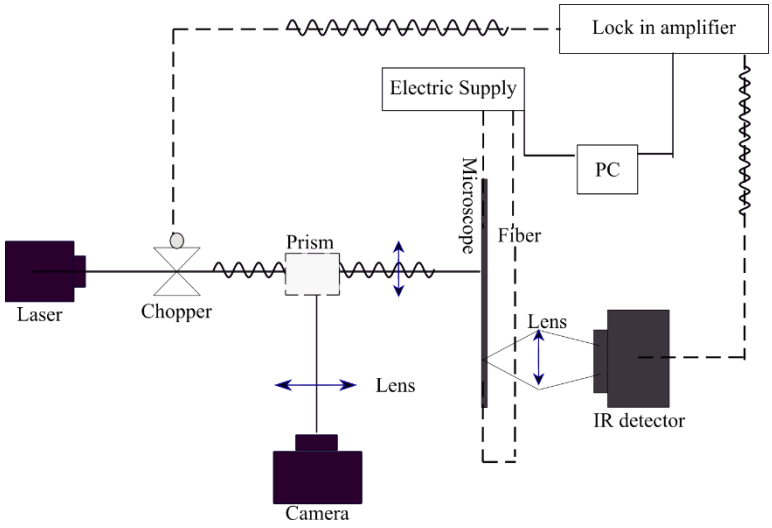


Figure 1.7: Schematic diagram of periodic heating technique

• Transient electro thermal method: In the transient electro thermal (TET) method, a step current is passed through single fiber of length L (Figure 1.8). Due to Joule heating effect, the temperature increases and ultimately depending on the material it will change the electric resistance of the sample and ultimately the voltage of the sample will have a decreasing profile with time t. With the oscilloscope, the voltage is monitored and by its evolution $((V(t) - V_0)/(V(t \to \infty) - V_0))$ the normalized temperature rise can be

obtained. V_0 is the initial voltage and $V(t \to \infty)$ is the steady state voltage over the sample; Fitting the experimental data of the sample with the analytical model (Eq. 1.7) developed in the article of Liu et al. gives its thermal diffusivity (α_{eff})[16].

$$\Delta T^* = \frac{96}{\pi^4} \sum_{m=1}^{\infty} \frac{1 - exp\left[-(2m-1)^2 \pi^2 \alpha_{eff} t / L^2\right]}{(2m-1)^4} \tag{1.7}$$

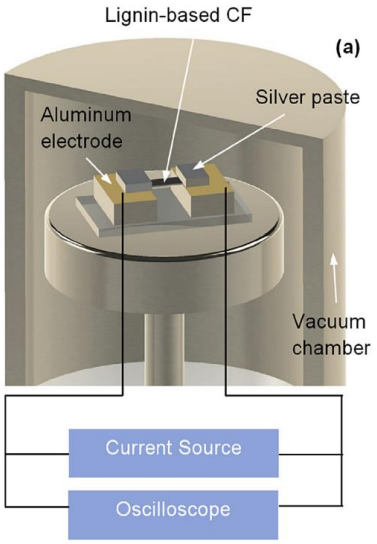


Figure 1.8: Schematic diagram of TET method

Although these techniques have widely focused on thermal characterization of the single fiber, however they have certain disadvantages. These methods are capable of estimation of certain thermal properties, either axial thermal conductivity or heat capacity. These approaches are widely focused on the estimation of diffusivity and heat capacity in order to get the thermal conductivity. Most importantly rather less focus was given to the measurement of radial thermal conductivity. Apart from this, it uses either thermocouple or IR sensor for the temperature measurement. With small diameter of the fiber typically less than 10µm, it's a big challenge to get good accuracy and stability in the result. Therefore, in the upcoming section a brief introduction about a more diverse technique, 3ω method, is presented that has the capability of overcoming these drawbacks. Its widespread applications in characterization of thermal properties in multiple scales of materials makes it an intriguing choice of experiments.

2.2 3ω method

In 1912, O.M. Corbino[24] was the first one to observe a 3ω voltage signal while testing the metal filaments of an incandescent light bulbs by passing an alternating current for measuring thermal diffusivity. Later this theory was used for measurement of thermal diffusivity of various types of material by heating the specimen using a metal filament which is in contact with the specimen under test. In the year 1987, Cahill and Pohl used this concept for the measurement of thermal conductivity of multiple amorphous solids using thin film metal acting as heater and

thermometer[25][26]. Successively the applicability of 3ω method has been becoming large starting from macro scale carbon-fiber/epoxy composite[27], textiles[5] or flexible bio sourced polymers[28] to thin films ranging from nanometers to micrometers in thickness[19][29][30]. Even the thermal conductivities of liquids and gases [31][32][33] are also correctly estimated using this technic. In the recent times, apart from heater on the substrate configuration, many researches are also focusing on direct implementation of 3ω signal with the specimen such as a wire or fiber. This was made possible with the development of fine electronic instrument such as lock-in Amplifier as it removes the necessity of frequency tripling circuit, making the electrical circuit simpler [27].

In the article of Lu et al [10], they developed simplified experimental setup with a four-probe resistance for simultaneously measurement of the specific heat and the axial thermal conductivity of a rod or filament-like specimen such as single platinum wire and carbon nanotube bundles. In this article, a 1D heat transfer equation was solved and then a solution for three omega voltage was presented in the form of an analytical model. But later simplified equations provided two separate models depending on high or low frequency working range. Lu et al [10] have also mentioned many detailed experimental tips while performing the 3ω method experiments under vacuum. They also chose proper approximation to minimize the effect of convective and radiative heat losses by performing the experiment in vacuum.

Later in 2005 [34], Dames and Chen have measured the thermal conductivity and specific heat of a suspended wire. They discussed two types of setup with current source and voltage source. It showed that the conversion of voltage source to approximate its action as current source is only valid when the sample resistance is small. They put emphasis on the information about the thermal conductivity in not only 3ω, but also 1ω and 2ω mode. Then in 2007 [35], Wang et al. published a research with four-pads 3ω method which has the capability to cancel the noise in the signal due to 1ω and measure the thermal conductivity, thermal diffusivity and heat capacity of an individual wire such as Platinum wire or polyacrylonitrile (PAN) based fiber. Later, in 2014 [36][37], Xing et al. presented an article on accurate thermal property measurement of fine fibers by the 3-omega technique. Along with presenting the effect of two sources types namely current and voltage, it also showed the effect of 1ω cancellation in the measurement of thermal properties. In this paper, the thermal properties such as heat capacity, thermal conductivity and diffusivity can be estimated independently using an appropriate excitation frequency range by the application of separate analytical models for each parameter.

In the same year, a Ph.D. thesis by was presented by Junfeng Liang where he successfully retrieved the value of the thermal conductivity, both axial and transversal, for carbon fiber reinforced composite and also for a single fiber[38]. In case of single carbon fiber, type AS4 and IM10, the axial thermal conductivity (Table 2) and heat capacity are estimated by fitting the experimental data with the complete analytical model developed by Lu et al[10]. But the use of complete analytical model was not properly justified as all the previous research was focused on simplified analytical model depending on the low frequency and high frequency. For radial thermal conductivity, a novel 1D analytical model was developed by the assumption of the fiber type T650 placing in a semi-infinite medium such as de-ionized water. The estimated radial

thermal conductivity was approximately 1.5 W m^{-1} K^{-1}. In this case, also no clear justification of the choice of working frequency range is provided.

The 3ω method consists of heating the sample with an alternating current at a frequency ω. The current leads to temperature fluctuations at 2ω, ultimately resulting in fluctuations of the voltage at both ω and 3ω. The variation of the 3ω voltage with the frequency contains the information about the thermal properties such as axial thermal conductivity and volumetric heat capacity of the sample. It is therefore important to eliminate the 1ω voltage by certain improvement in the setup such as a Wheatstone bridge [11] or an analog balance bridge circuit[35]. Fitting the 3ω voltage with the developed analytical model (section 3.1) can estimate simultaneously the unknown thermal properties such as axial thermal conductivity and volumetric heat capacity. Additionally, the specimen is itself acting as a heater making the accuracy in the measurements improved.

3. Models for determining fiber thermal conductivity from 3ω response

In this thesis, the 3ω method is applied on the sample as a wire or fiber like filament. It is required that the sample must be either electrical conductive or semi- conductive. The fiber is usually suspended between two copper strips serving as both electrodes and heat sinks. The AC driven voltage or current is directly fed onto the specimen and the specimen itself will response as both heater and sensor. The heat generation due to this voltage or current fluctuation in the sample can be predicted by solving 1D heat transfer equation. In the literature there are various approaches towards the development of the analytical model for voltage fluctuations, these are later being fitted with the experimental results to retrieve the thermal properties. The choice of a high frequency model for the estimation of heat capacity and low frequency for the thermal conductivity[10][20].

Although in the thesis of Liang[38] the global analytical model by Lu et al[10] is used for estimation of axial thermal conductivity and heat capacity simultaneously, however, it's rather questionable to see no discussion on the choice of working frequency range. In my thesis, the objective is to use the full frequency dependent analytical model developed in the paper of Lu et al. This was made possible by the sensitivity analysis to determining a working frequency range where the sensitivity of 3w voltage is high for both thermal conductivity and heat capacity.

3.1 Analytical Model

The schematic diagram of the sample over the copper electrodes is depicted in Fig. 7. The fiber, assumed straight and of length L, is connected to two electrodes with constant temperature. The measurement of the voltage between the two electrodes over a given range of frequencies is then used to identify the thermal properties, by using a thermal model, which can be either analytical or numerical. This section provides a brief introduction of the analytical model for the 3ω voltage response of a self-heating fiber depending on the imposed frequency (ω). The model assumes that the specimen is a uniform cylinder placed between two heat sinks (copper electrode)

with perfect contact at the joints (Fig. 7). An alternating electrical current ($I_0\sin(\omega t)$) with a frequency ω passed through the sample that has an electrical resistance R and length L.

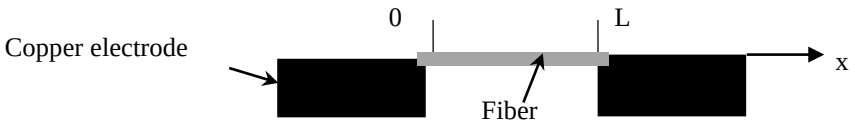


Figure 1.9: Schematic diagram of the fiber sample with copper holders

Lu et al. [11] has developed an analytical model for 1D heat conduction along the fiber with a source term that can predict the 3ω voltage through the sample. The partial differential equation associated to the heat conduction problem is as follows:

$$\rho C_p \frac{\partial}{\partial t}T(x,t) - k\frac{\partial^2}{\partial x^2}T(x,t) = \frac{I_o^2 \sin^2 \omega t\,[R_0(1+\alpha_e(T(x,t)-T_o)]}{SL} \tag{1.8}$$

And boundary and initial conditions as

$$\begin{cases} T(0,t) = T_o \\ T(L,t) = T_o \\ T(x,0) = T_o \end{cases} \tag{1.9}$$

where ρ is the density, C_p is the heat capacity, k is the thermal conductivity, $\omega = 2\pi f$ is the angular frequency, f is the frequency, $T(x,t)$ is the temperature of the sample at position *x* and time *t*, T_0 is the ambient temperature, $I_0$is the amplitude of the current, R_0 is the electrical resistance of the fiber at T_0, α_e is the temperature coefficient of this electrical resistance, S is the cross sectional area and L is the length of the sample. Let $\Delta(x,t)$ denotes the temperature variation from T_o , i.e. $\Delta(x,t) = T(x,t) - T_o$, then Eq. (1.8) and (1.9) become:

$$\frac{\partial}{\partial t}\Delta(x,t) - \alpha_t\frac{\partial^2}{\partial x^2}\Delta(x,t) - csin^2\omega t\Delta(x,t) = bsin^2\omega t \tag{1.10}$$

With initial and boundary conditions changed to

$$\begin{cases} \Delta(0,t) = 0 \\ \Delta(L,t) = 0 \\ \Delta(x,0) = 0 \end{cases} \tag{1.11}$$

Where $\alpha_t = \left(\frac{k}{\rho C_p}\right)$ is the thermal diffusivity, $b = \frac{I_0^2 R}{\rho C_p LS}$, $= \frac{I_0^2 R'}{\rho C_p LS}, R' = R_0\alpha_e$. Using the theory of momentum impulse as taking $bsin^2\omega t$ as the instantaneous force at each time interval, we can obtain $\Delta(x,t)$ as an integral of the samples responses to that force. Thus we obtain

$$\Delta(x,t) = \int_{-\infty}^{t} z(x,t;\tau)d\tau \tag{1.12}$$

Where $z(x,t;\tau)$ satisfies

$$\frac{\partial z}{\partial t} - \alpha\frac{\partial^2 z}{\partial x^2} - csin^2\omega t \; \mathrm{z} = 0 \tag{1.13}$$

While satisfying

$$\begin{cases} \mathrm{z}(0,t) = 0 \\ \mathrm{z}(L,t) = 0 \\ \mathrm{z}(x,\tau+0) = bsin^2\omega\tau \end{cases} \tag{1.14}$$

Using the expansion of Fourier series we can expand $z(x,t;\tau)$ as

$$\mathrm{z}(x,t;\tau) = \sum_{n=1}^{\infty} U_n(t;\tau)\sin\left(\frac{n\pi x}{L}\right) \tag{1.15}$$

This gives

$$\sum_{n=1}^{\infty}\left[\frac{dU_n}{dt} + \left(\frac{n^2}{\gamma} - csin^2\omega t\right)U_n\right]\sin\left(\frac{n\pi x}{L}\right) = 0 \tag{1.16}$$

where $\gamma \equiv L^2/\pi^2\alpha_t$ is the thermal time constant for axial heat transfer. The term $csin^2\omega t$ can be neglected if $\frac{n^2}{\gamma} \gg c$ or equivalently

$$\frac{I_o^2 R' L}{n^2\pi^2 kS} \ll 1 \tag{1.17}$$

The above condition indicates that the heating power inhomogeneity caused by the resistance fluctuation along the specimen should be much less than the total heating power. It is recommended that Eq. 1.17 must be satisfied for obtaining accurate results. After dropping the $csin^2\omega t$ term the solution to the ordinary differential equation can be written as

$$U_n(t;\tau) = C_n(\tau)e^{-\left(\frac{n^2}{\gamma}\right)(t-\tau)} \tag{1.18}$$

We can obtain the value of C_n by implement the above equation in the initial condition $t = \tau$ stated in Eq. 1.14 from the expression $\sum_{n=1}^{\infty}\left(\frac{2[1-(-1)^n]}{n\pi}\right)\sin\left(\frac{n\pi x}{L}\right) = 1$ for 0<x<L:

$$C_n(\tau) = \frac{2b[1-(-1)^n]}{n\pi}\sin^2\omega\tau \tag{1.19}$$

Using (13) and (14) in (9) we obtain

$$z(x,t;\tau)=\sum_{n=1}^{\infty}\sin\left(\frac{n\pi x}{L}\right)\frac{2b[1-(-1)^n]}{n\pi}\sin^2(\omega\tau)e^{-\left(\frac{n^2}{\gamma}\right)(t-\tau)} \tag{1.20}$$

The term in Eq. 1.20 can be implemented in Eq. 1.12 to obtain the expression for temperature by using integration by parts.

$$T(x,t)-T_o=\Delta_o\sum_{n=1}^{\infty}\frac{[1-(-1)^n]}{2n^3}*\sin\left(\frac{n\pi x}{L}\right)\left[1-\left(\frac{\sin(2\omega t+\phi_n)}{\sqrt{(1+\cot^2\phi_n)}}\right)\right] \tag{1.21}$$

Where $cot\phi_n=\frac{2\omega\gamma}{n^2}$, and $\Delta_o=\frac{2\gamma b}{\pi}=\frac{2{I_o}^2RL}{\pi kS}$ is the maximum DC temperature accumulation at the center of the specimen. The electrical resistance fluctuation can be obtained by integrating temperature fluctuation over the length.

$$\delta R=\frac{R'}{L}\int_0^L[T(x,t)-T_0]dx \tag{1.22}$$

This gives us an expression for resistance fluctuation that is expressed as shown below.

$$\delta R=R'\Delta_o\sum_{n=1}^{\infty}\frac{[1-(-1)^n]^2}{2\pi n^4}\left[1-\left(\frac{\sin(2\omega t+\phi_n)}{\sqrt{(1+\cot^2\phi_n)}}\right)\right] \tag{1.23}$$

ϕ_n is the value of the phase constant. This expression of electrical resistance fluctuation (function of 2ω) is due to the temperature fluctuation which can then be added to the sample initial electrical resistance R_0 to obtain the total resistance($R_0+\delta R$). This value of total resistance is then multiplied with the applied AC current ($I=I_o sin(\omega t)$) to obtain a value of voltage (V=IR) drop across the sample,

$$V=\ IR=I(\omega)\big(R_0+\delta R(2\omega)\big)=f(\omega)+g(3\omega) \tag{1.24}$$

The voltage has two components, one depending on ω and another on 3ω . The 3ω part contains the information about the thermal properties as it is derived from the temperature fluctuation part of resistance. So the third harmonic voltage can be derived as follows after doing some mathematical simplification[10].

$$V_{3\omega}(t)\approx\ -\frac{2{I^3}_oR_0R'}{\pi^4kS\sqrt{1+(2\omega\gamma)^2}}\sin(3\omega t-\phi) \tag{1.25}$$

Here the phase constant has been redefined as $\phi=\frac{\pi}{2}-\phi_{n=1}$ with $tan\phi\approx 2\omega\gamma$. Averaging (Root Mean Square) voltage over time at 3ω frequency can be written as follows:

$$V_{3\omega\,rms}\approx\ -\frac{4I_{rms}^3LRR'}{\pi^4kS\sqrt{1+(2\omega\gamma)^2}} \tag{1.26}$$

This is the global frequency dependent analytical model for 3ω fluctuations of voltage. Fitting the experimental data of $V_{3\omega\,rms}$ vs proper frequency with this analytical Eq. 1.21 can estimate the value for axial thermal conductivity and volumetric heat capacity ($\gamma\ \equiv L^2\rho C_p/\pi^2k$) for the sample under test.

3.2 Pre-requisites for the validity of analytical model

As discussed previously, applicability of the analytical model for a successful implementation of the 3ω method requires few preconditions to be fulfilled first. These factors came into play either during the derivation of the analytical model or for neglecting convective/radiative losses during experiment. In the following, these are explained in brief:

- From the Eq. 1.26, we can observe that $V_{3\omega_rms} \propto I^3$. To validate the 3ω method it is essential first to fulfill this condition.
- The choice of correct current value is necessary in order to follow the condition which comes across the derivation of the analytical Eq. 1.17:

$$\delta_0 = \frac{I_0^2 L R^{'}}{\pi^2 k S} \ll 1 \tag{1.27}$$

The current implemented should not be even very small as a small current will tend to have a small $V_{3\omega_rms}$ and thus include the noise coming from other electronic apparatus.

- It is also important to take care of the length of the sample that is being chosen for the preparation of the sample. A larger length will result in larger thermal time constant ($\gamma \propto L^2$) which will result in a lower frequency window. This will make the analytical equation independent of thermal conductivity as the denominator is primarily dominated by the high value of the thermal time constant. A detailed sensitivity analysis is shown in section 4.
- To encounter for the radiative heat loss through the fiber surface, one should take care that radiative power due to the fluctuations in temperature along the specimen should be much less than the axial heat current[10]. In this paper, it is well explained by solving the partial differential equation of heat transfer with radiative heat loss term (Eq. 1.29).

$$W(x,t) = \pi\varepsilon\sigma D(T(x,t)^4 - {T_o}^4) \approx 4\pi\varepsilon\sigma D{T_o}^3\Delta(x,t) \tag{1.28}$$

$$\rho C_p \frac{\partial}{\partial t}T(x,t) - k\frac{\partial^2}{\partial x^2}T(x,t) + \frac{16\varepsilon\sigma T_0^3}{D}(T(x,t) - T_o) = I_o^2 \sin^2 \omega t\,[R_0(1 + \alpha_e(T(x,t) - T_o)] \tag{1.29}$$

Where ε is the emissivity, σ is the Stefan Boltzmann constant, D is the diameter of the sample. While deriving the solution for heat transfer equation for the above equation, it was indicated that the radiation heat loss can be neglected [10] if

$$\frac{16\varepsilon\sigma T_0^3 L^2}{\pi^2 k D} \ll 1 \tag{1.30}$$

- As the copper slab is chosen as the heat sink for the fiber thus it is very important that the state of the copper slab should be good. As the copper suffers from oxidation thus it will lead to spurious signal and results in unstable $V_{3\omega_rms}$. Thus it's

necessary to remove the oxidation from the copper plate either by scrubbing with sand paper.

- ❖ In addition, it is crucial to analyze the effect of the contact between the sample and copper blocks. This would add to the overall uncertainty in the parameter estimation.

These guidelines can help in achieving a better accuracy in the results and fulfilling the objective faster. But with these pre-requisites, it is crucial to verify the appropriateness of analytical model to our experimental setup. Furthermore previous researches on 3ω method were restrictive to experiments in a vacuum chamber [11][19] rather the question of the effect of convective heat losses when working at atmospheric pressure is not addressed. This led to the objective of development of a numerical model without any prior presumptions and to compare the results with the analytical model. It can strongly justify the further utility of this analytical model for extracting the unknowns from experiments.

3.3 Numerical Finite Difference Model

This section shows a brief description of the numerical model for estimating the 3ω response of one fiber in the configuration depicted in Figure 1.10 after passing an alternating current. Compared to the previous analytical model, the numerical one takes into account the lateral heat losses through the heat transfer coefficient (h). In the case of constant thermophysical parameters, the heat transfer phenomena along with convective heat loss term can be described by the following 1D partial differential equation with the spatial boundary condition same as Eq. 1.9:

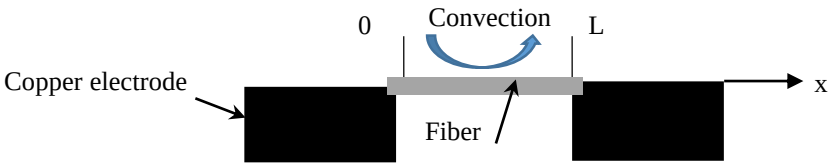


Figure 1.10: Schematic diagram for the sample to solve numerical model

$$\frac{\rho C_p}{k}\frac{\partial}{\partial t}T(x,t) - \frac{\partial^2}{\partial x^2}T(x,t) + m^2(T(x,t) - T_o) = \frac{Q}{k} \tag{1.31}$$

where $m^2 = {}^{4h}/_{kD}$ with h the heat transfer coefficient of air that surrounds the sample. Q is the average volumetric heat source due to the alternating current. By choosing $\Delta T(x,t) = T(x,t) - T_o$, the above equation can be transformed to

$$\frac{\rho C_p}{k}\frac{\partial}{\partial t}\Delta T(x,t) - \frac{\partial^2}{\partial x^2}\Delta T(x,t) + m^2\big(\Delta T(x,t)\big) = \frac{Q}{k} \tag{1.32}$$

One of the outcomes from the analytical model is $\Delta T(x,t) \sim R = f(2\omega)$. The volumetric heat source fluctuates at 2ω $\left({}^{2RI_{rms}^2}/_{SL} \sim f(2\omega)\right)$, the terms ΔT and Q can be sought in the following periodic form:

$$\Delta T = \tilde{T} e^{j2\omega t}, Q = \tilde{Q} e^{j2\omega t} \tag{1.33}$$

where $\tilde{T}$ and $\tilde{Q}$ are the complex expressions of the temperature drop and volumetric power respectively. Eq. 1.32 can be transformed by implementation of Eq. 1.33 to:

$$\frac{\partial^2 \tilde{T}}{\partial x^2} = -\frac{\tilde{Q}}{k} + \left(\frac{j2\omega \rho C_p}{k} + m^2\right)\tilde{T} \tag{1.34}$$

The spatial boundary conditions present in Eq. 1.9 can be transformed to Eq. 1.35

$$\begin{cases} \tilde{T} = 0, & x = 0 \\ \tilde{T} = 0, & x = L \end{cases} \tag{1.35}$$

A 1D mesh representative of the sample was generated and a central finite difference approach was used to solve the Eq. 1.34.

$$\frac{\partial^2 \tilde{T}}{\partial x^2} = \frac{\tilde{T}_{i+1} - 2\tilde{T}_i + \tilde{T}_{i-1}}{\Delta x^2} \tag{1.36}$$

The source term is independent of spatial discretization, thus the Eq. 1.34 is transformed to

$$\frac{1}{\Delta x^2}\,\tilde{T}_{i+1} - \left[\frac{2}{\Delta x^2} + \frac{j2\omega}{\alpha} + m^2\right]\tilde{T}_i + \frac{1}{\Delta x^2}\tilde{T}_{i-1} = -\frac{\tilde{Q}}{k} \tag{1.37}$$

For simplification, few variable assumptions are taken such as

$$\frac{1}{\Delta x^2} \text{ as } \Omega, \quad -\left[\frac{2}{\Delta x^2} + \frac{j2\omega}{\alpha} + m^2\right] \text{ as } \beta, \quad -\frac{\tilde{Q}}{k} \text{ as } \gamma \tag{1.38}$$

The equation transformed to visually more compact form to

$$\Omega\,\tilde{T}_{i+1} + \beta\,\tilde{T}_i + \Omega\,\tilde{T}_{i-1} = \gamma \tag{1.39}$$

The solution of temperature can be achieved by a simple matrix conversion which will change the equation to multiple equations at each nodes. The number of equations formed is equal to the number of nodes and thus the matrix form of the equation is shown as

$$\begin{bmatrix} \tilde{T}_2 \\ \tilde{T}_3 \\ \vdots \\ \vdots \\ \vdots \\ \tilde{T}_{N-1} \end{bmatrix} = \begin{bmatrix} \beta & \gamma & 0 & \dots & \dots & 0 \\ \gamma & \beta & \gamma & 0 & \dots & 0 \\ 0 & \gamma & \beta & \gamma & \dots & 0 \\ \vdots & \vdots & \ddots & \ddots & \ddots & 0 \\ \vdots & \vdots & 0 & \ddots & \ddots & \ddots \\ 0 & 0 & 0 & 0 & \gamma & \beta \end{bmatrix}^{-1} \begin{bmatrix} \delta \\ \vdots \\ \vdots \\ \vdots \\ \vdots \\ \delta \end{bmatrix} \text{ with } \begin{cases} \gamma = \frac{1}{\Delta x^2} \\ \beta = -\left[\frac{2}{\Delta x^2} + \frac{j2\omega\rho C_p}{k} + m^2\right] \\ \delta = -\frac{\tilde{Q}}{k} \end{cases} \tag{1.40}$$

The complex form of the temperature rises at all nodes ($\tilde{T}_2, \tilde{T}_3 \dots \tilde{T}_{N-1}$) can be estimated by solving this linear system. The modulus of the average of this temperature rises over all nodes (N) gives the average axial temperature rise T_{av} of the sample for certain frequency:

$$T_{av} = \left\| \sum_{1}^{N} \tilde{T}_i \right\| / N \tag{1.41}$$

The overall voltage response at each frequency measured in 3ω method is dependent on T_{av} of the sample and thus the numerical $V_{3\omega\, rms}$ can be expressed as follows:

$$V_{rms} = I_{rms}(R_0 + R_0\alpha_e T_{av}) = f(\omega) + g(3\omega) \tag{1.42}$$

$$V_{3\omega\, rms} = I_{rms} R_0 \alpha_e T_{av} \tag{1.43}$$

This step is repeated for estimating $V_{3\omega\, rms}$ for the desired frequencies. It is interesting to observe that the effect of convective loss during the measurements under atmospheric condition can be approximated by implementation of heat transfer coefficient in the term 'm' present in Eq. 1.40. This is determined by the correlations given in the literature. For the experimental conditions of 3ω method, the correlations by Morgan[39] or Churcill and Chu[40] are suitable to implement according to the Rayleigh Number (Ra).

$$Ra = \frac{g\beta\Delta T D^3}{\vartheta \alpha_t} \tag{1.44}$$

Where g is acceleration due to gravity, β is the thermal expansion coefficient, ϑ is the kinematic viscosity.

3.4 Comparison of Analytical and Numerical model

In this section, a comparison between the $V_{3\omega\, rms}$ calculated with the analytical model and numerical model is shown. This could ultimately help in understanding the effect of various assumptions (section 4.2) on the validity of the analytical model. The comparison between these two models was proceeded by testing the 3ω voltage fluctuations ($V_{3\omega\, rms}$) over a test case for chromel wire (assuming a diameter of 13 µm) and carbon fiber (assuming a diameter of 7 µm) with a length of 1.5mm. An alternating current of 6mA and 1mA was assumed to pass through the chromel wire and carbon fiber respectively. The difference in the choice of the current input is due to the fact that carbon fiber are electrically more resistive as compared to chromel wire. The values of thermal properties were imposed from the literature or from the supplier [41–43]. A comparison of the estimated value of $V_{3\omega\, rms}$ under vacuum, by using numerical and analytical models is shown in Figure 1.11. It showed a good agreement between the $V_{3\omega\, rms}$ values obtained with the two models. The difference lies mostly at lower frequencies with a value less than 1.6% of maximum $V_{3\omega\, rms}(f < 0.1Hz)$. A similar result was found for comparison of analytical and numerical model in case of carbon fiber. Additionally, for each test, the validity condition of Eq. 1.17 for the analytical model is well checked with an approximate value of $\delta_0 = 4\times10^{-4}$ for chromel and $\delta_0 = 4\times10^{-2}$ for carbon fiber.

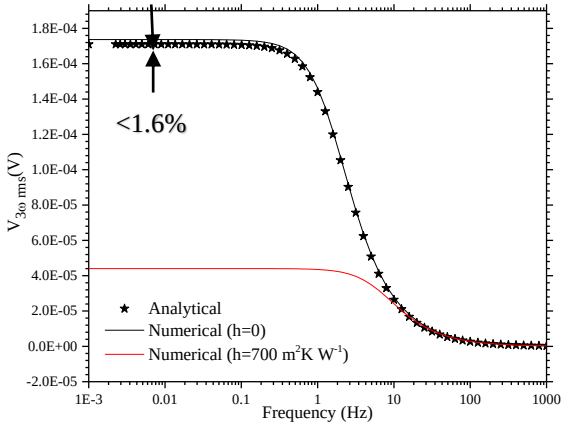


Figure 1.11: Numerical and analytical models comparison and effect of convective losses (13.6μm diameter and 1.5mm length of chromel wire)

In addition to the comparison of both models under vacuum, a test was also done to quantify the effect of convective heat transfer. Since the numerical model has a term 'm' to handle the convective heat losses, thus the $V_{3\omega\,rms}$ is predicted from a periodic heating of the sample in an atmospheric condition. This is possible by imposing an approximate value of heat transfer coefficient with a correlation for natural air convection around a horizontal cylinder[39][40] with an assumption of max 1K[10] increase in temperature. The radiation losses can be neglected as the criterion of Eq. 1.8 is always respected for the chromel wire (δ_1~0.025) and also carbon fibers (δ_1~0.079). It can be observed from Figure 1.11 that the convective heat transfer leads to a huge drop of the $V_{3\omega\,rms}$value. To quantify the effect of convective heat loss on the estimation of thermal conductivity and heat capacity, this data is then fitted with analytical model. Table 3 shows that the thermal conductivity value is increased by ~390% and the heat capacity value is decreased by ~8% for chromel wire.

These biases become more prominent in case of carbon fiber as its thermal conductivity is smaller and also as the approximated heat transfer coefficient almost doubled due to its smaller diameter. Thus it is highly important to use vacuum while performing measurements in 3ω method especially for thermal conductivity. Thus, all the experiments of 3ω method in this thesis are performed under vacuum.

Sample	Heat transfer coefficients	Thermal Properties estimated	
	h($Wm^{-2}K^{-1}$)	k($Wm^{-1}K^{-1}$)	ρC_P(MJ $m^{-3}K^{-1}$)
Chromel wire	0	17	3.8
	700*	66	3.48
Carbon fiber	0	10	1.3
	1300*	133	1.14

*: computed using correlation for natural air convection around a horizontal cylinder [40]

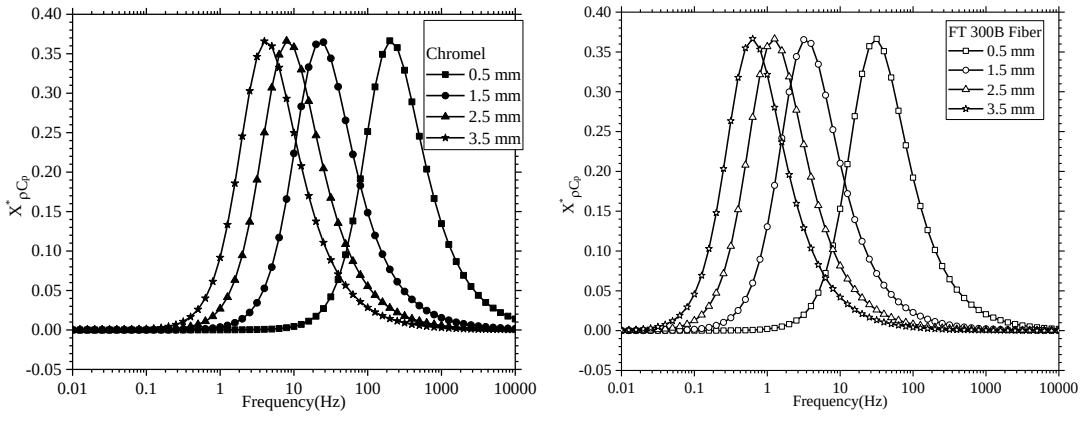
Table 3: Thermal conductivity and heat capacity estimated with and without convective losses

4. Sensitivity Analysis

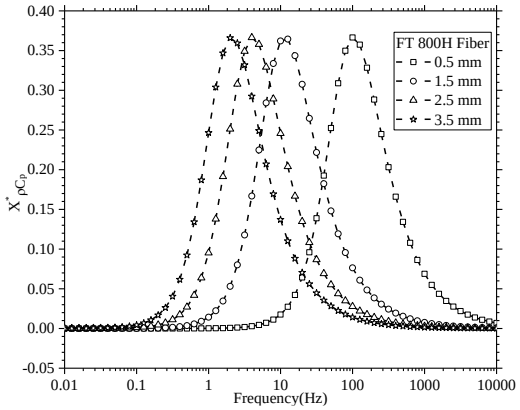
One of the important objective is to find the frequency range where it is possible to use the frequency dependent analytical model for estimation of both axial thermal conductivity and heat capacity. A sensitivity analysis was performed over the voltage fluctuations at 3ω with the unknown thermophysical parameters (u_P), ultimately helping in choosing a frequency window that can give a better accuracy in the results. This is defined by the reduced sensitivity coefficients ($X^*_{u_P}$) and is computed by [44]:

$$X^*_{u_P} = u_P \frac{\partial V_{3\omega\, rms}}{max(V_{3\omega\, rms})\partial u_P}, \qquad with\, u_P = k, \rho C_p \tag{1.45}$$

From the analysis on various parameters impacting the calculation of $X^*_{u_P}$, it was found that the length of the sample can hugely influence the working frequency range. Thus various lengths ranging from 0.5 to 3.5 mm were chosen in order to see how this can affect the reduced sensitivity coefficient of multiple samples. The sensitivity analysis of the testing sample of chromel wire or PAN fibers type FT300B and FT800H (explained in section 5.2). The thermal conductivity and heat capacity were imposed from the literature or from the supplier (Table 5 and 6). Figure 1.12 and 1.13 show that the sensitivities of thermal conductivity and heat capacity are high in a particular frequency range depending on the sample length. A better accuracy can be recovered if the sensitivity coefficients are higher in the working frequency range. Working on a frequency lower than 1Hz would lead to higher time constant and ultimately longer time for stabilization. On the other hand working on a higher frequency would lead to a choice of smaller length for having higher sensitivity of the unknown parameters. It will create practical problems for the sample such as placing it on the holder or putting silver paste. Thus a frequency window of 1-100Hz is chosen in order to avoid these problems. For example, 0.8-1.6mm range of length for carbon fiber sample FT300B will give higher $X^*_{u_P}$ values, thus a better estimation of the thermal properties.

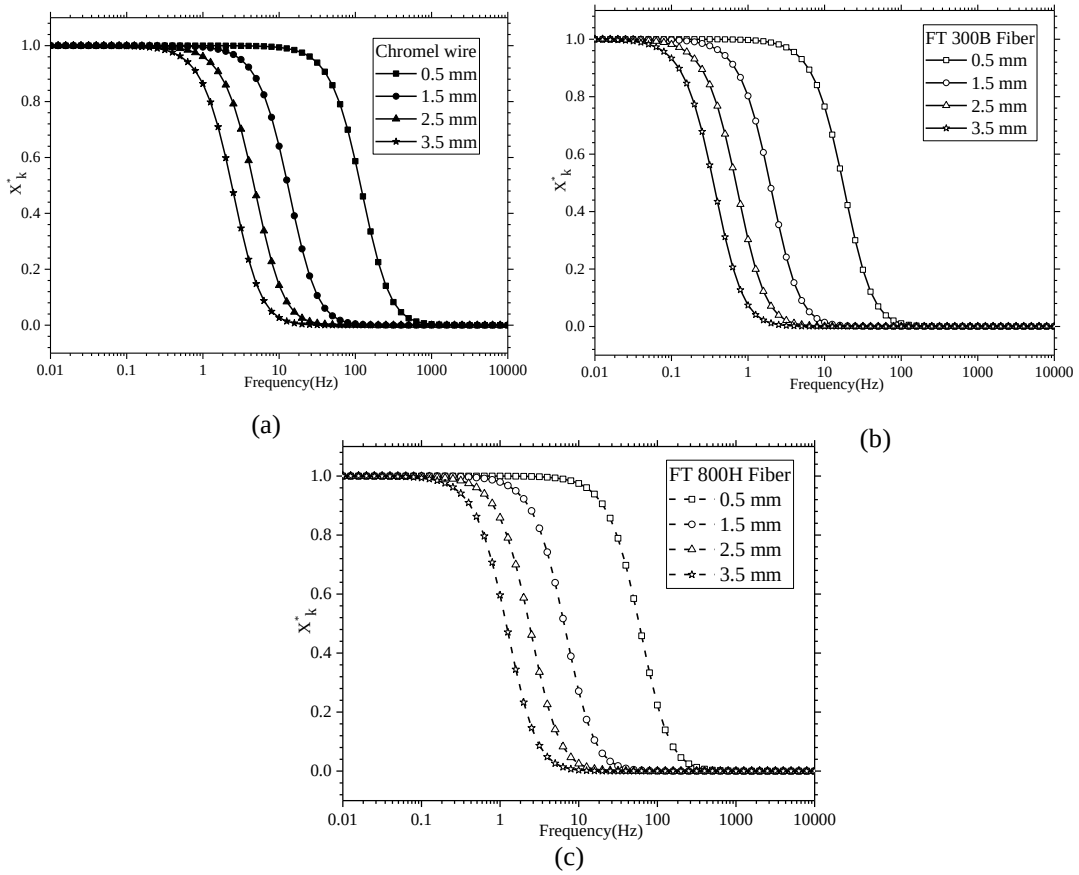


(a) (b)



(c)

Figure 1.12: Sensitivity analysis of the $V_{3\omega\ rms}$ to the volumetric heat capacity with varied sample lengths (a) chromel wire (b) FT300B (c) FT800H



(a) (b)

(c)

Figure 1.13: Sensitivity analysis of the $V_{3\omega\ rms}$ to the axial thermal conductivity with varied sample lengths (a) chromel wire (b) FT300B (c) FT800H

5. Experimental Setup and Materials

The previous section showed the importance of choosing proper frequency window which is one of the most important aspect in 3ω method experiments. In this section the experimental setup along with the description of each component used are discussed.

5.1 Experimental Setup

The experimental setup for 3ω method can have multiple configurations for fulfilling the objective of extraction of 3ω voltage from the sample. Depending on the type of source, it can be either with a voltage or current source[36][34]. The advantage of current source over the voltage source is the direct application of the 3ω theory where we assume the periodic heating by imposing an alternating current[36].

As mentioned in the section 2.2, it is necessary to extract just the 3ω signal by cancelling the 1ω signal. This can be achieved again by two types of setup, i.e., either with a Wheatstone bridge or with a differential amplifier (Figure 1.14). In order to measure the 3ω voltage in the sample, it is positioned in one of the branches of Wheatstone bridge circuit. On the other hand in differential amplifier circuit, it is placed in series with a potentiometer. Although both configurations can assist in getting just the 3ω voltage but differential amplifier has the capacity to work on a sample with high electrical resistance. On the contrary, in case of Wheatstone bridge, the stability of signal reduces as the resistance of the sample is more than 500 Ohms. This is due to the discrepancy with the 50 Ohms input impedance of the lock-in-amplifier. Moreover the error in the measurement of thermal conductivity with Wheatstone bridge is higher than using differential amplifier along with more repetitive results[30]. This was observed in few of the initial test in the thesis performed for 3ω voltage with Wheatstone bridge with a fiber of approximately 1 kOhms. Therefore two differential amplifiers (AD624) with a constant current source (Keithley 6221) were used for the detection of the voltage signal in the sample.

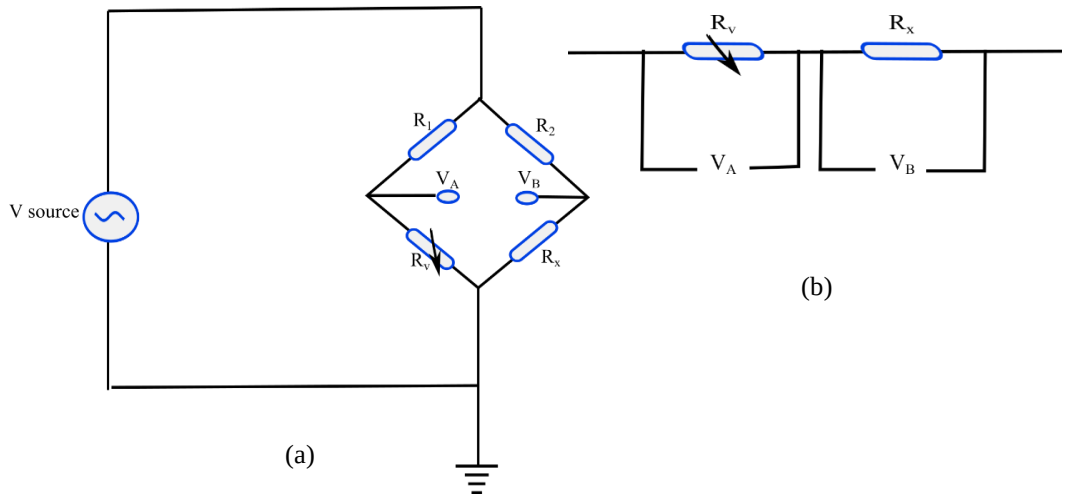
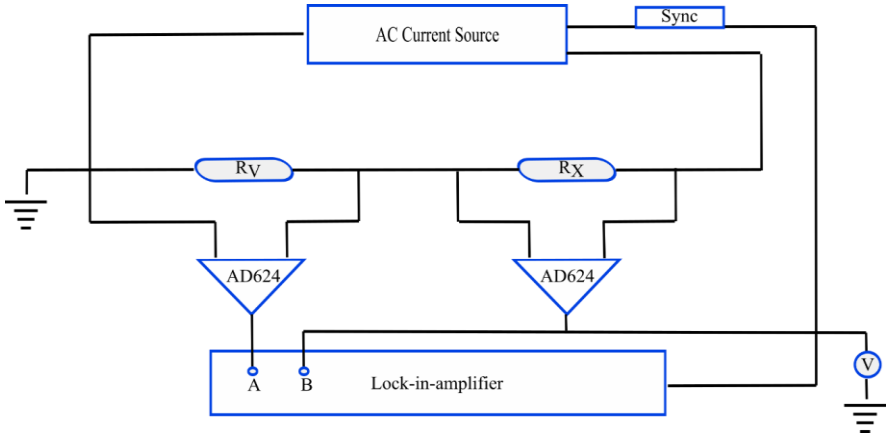
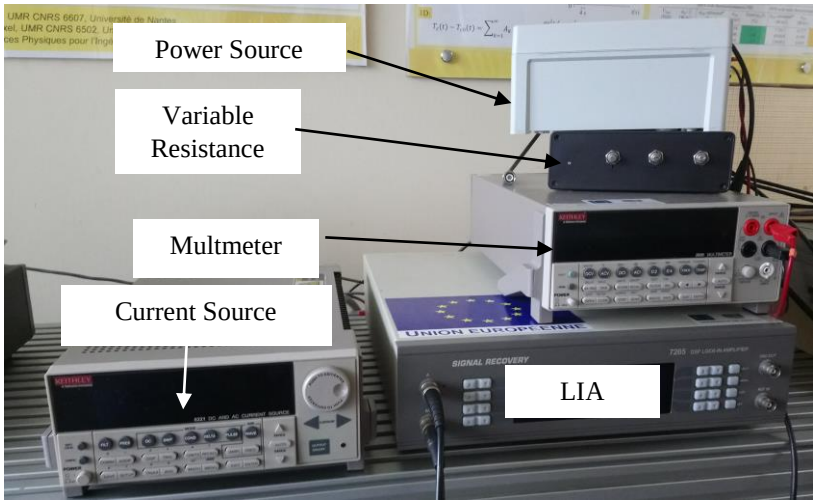


Figure 1.14: (a) Wheatstone bridge circuit (b) Differential amplifier

Figure 1.15 shows the circuit diagram for the detection of 3ω voltage while using a configuration of constant current source and differential amplifier. A detailed description about each apparatus along with the application in 3ω measurement is given below.



(a)



(b)

Figure 1.15: Electrical setup for 3ω measurement (a) Schematic (b) Electronic Instruments

AC current source: The current is supplied by a KEITHLEY 6221 current source. This model works on a wider current sourcing range from 4pA to 210mA peak to peak. It has the advantage of being cost effective, high consistency and robustness. It has a built in current source waveform generator that works in the frequency range of 1mHz to 100kHz. It can also produce huge variety of signals such as sinusoidal, square etc.

Variable resistance: As in differential amplifier the objective is to produce 1ω signal in two almost equal resistances and making a differentiation between them and finally get the information regarding the 3ω signal in the sample. In order to do so, a variable resistance (R_V) is used which can be manually tuned to get the same resistance as the sample (R_X). The variable resistance is built with three tunable resistances ranging from 2.5 to 5000 Ohms (Figure 1.16). This would generate the same 1ω voltage in the two resistances and with the help of differential amplifier AD624 it can extract any voltage fluctuations occurring in the two resistances. The amplifier AD624 with high precision and low noise is used at gain 1.

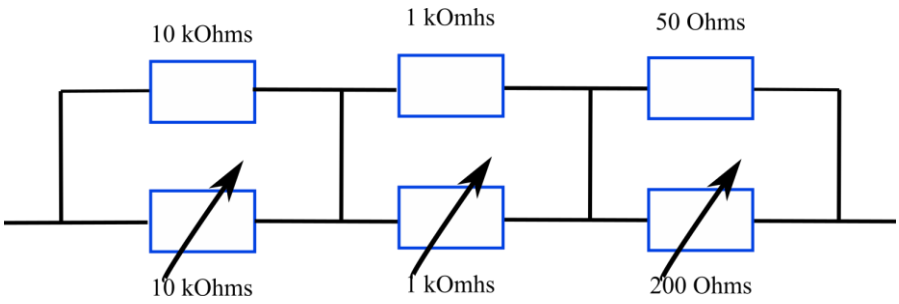


Figure 1.16: Variable resistance

Lock in amplifier: A lock-in-amplifier (LIA) has the capacity to either recover signal even in the presence of high noise or working at different frequency levels to provide signal of large order of magnitude with high resolution. For the experimental setup, SIGNAL RECOVERY 7265 LIA from AMETEK is used. It is being popularly used because of its multipurpose functioning range in many fields of scientific research such as material science, electrochemistry, optics, etc. [45]. It is a more versatile form of lock-in-amplifier (LIA) which uses digital signal processing that is suitable for experimental control and measurements. Thus it increases the working competences of LIA in favor of researcher. It has a wider frequency operating range from 1 mHz to 100 kHz. The major advantage for this model lies in the capability of detection of sensitivity to voltage up to 2 nV and current 2 fA, recovery of AC signal, recording transient data with high precision etc.[46]

Briefly, the block diagram for a LIA is as shown in Figure 1.17. This can help in detecting the real and imaginary part of a voltage signal with a low order magnitude despite of the noise in the signal. In this a phase sensitivity detector (PSD) multiplies the amplified input signal with noise to the reference input signal at a base frequency. Thus the LIA detects the signal at that particular base frequency. In the 3ω method, two input signals, i.e. A and B are differentiated among which one is from the sample and the other one from the variable resistance. In the LIA, A-B mode is switched on in order to detect the 3ω signal only in the sample. Initially in the LIA, 1ω signal is detected as in order to have the variable resistance equal to that of the sample and thus giving 1ω signal of voltage to the LIA as close as possible to 0V. Then the signal recovery is shifted to 3ω thus detecting only the 3ω voltage fluctuations in the sample as the variable resistance is a pure resistance with no 3ω voltage.

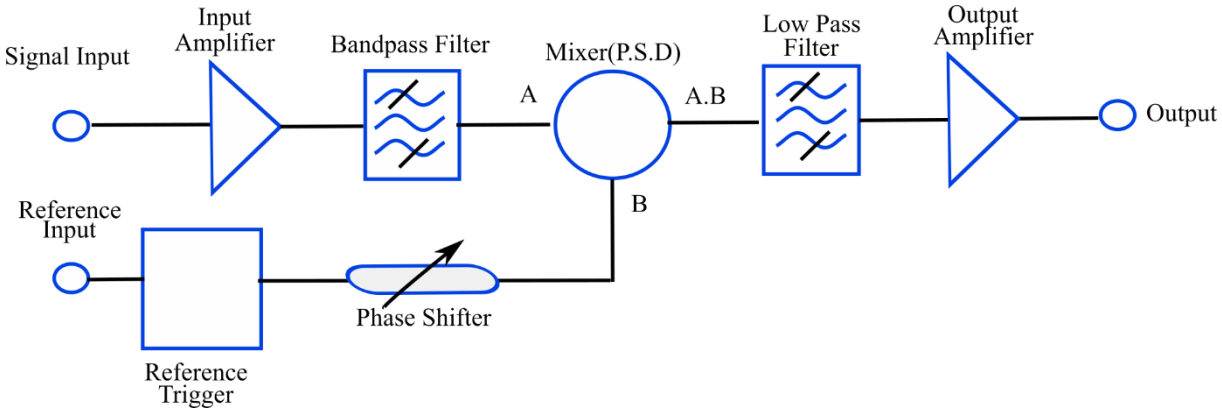


Figure 1.17: Block diagram for a LIA

5.2 Materials

In the literature, the 3ω method is used for metallic wire such as platinum[37] or tungsten [38][10], carbon nanotubes[10], or carbon fibers[35]. In this thesis, the objective is to measure the thermal properties of carbon fiber of types FT300B (high stiffness) and FT800H (high modulus) (Toray) provided by Chomarat company. Chromel wire (Omega Engg) is used for the validation of the experimental setup. The easy availability and similar thermal properties of chromel wire such as thermal conductivity or temperature coefficient of resistance makes it an ideal choice as a reference sample. Figure 1.18 shows the images retrieved from the scanning electron microscopy for the fiber FT300B and FT800H. The diameter of carbon fibers are ranging from 4-8µm making it a great difficulty for performing any direct measurements.

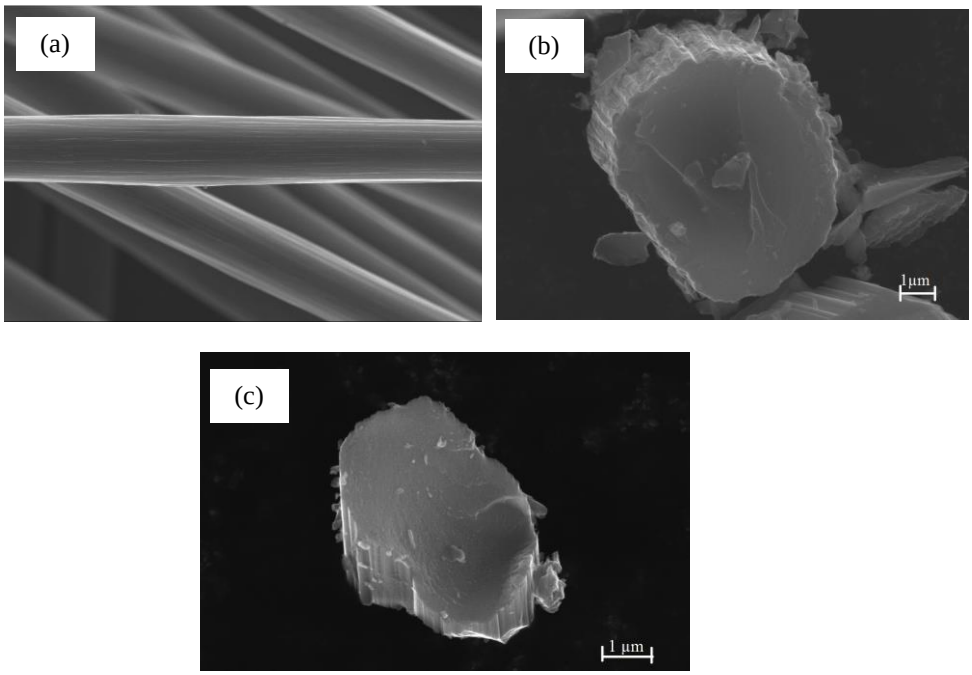


Figure 1.18: Scanning electron microscopy images for carbon fiber (a) along the length (b) along the cross-section FT300B (c) FT800H

5.3 Specimen Preparation

The schematic diagram associated to the analytical model for measuring the axial thermal conductivity and volumetric heat capacity is previously shown in Figure 1.9. The sample is cut into small pieces depending on the desired length and then placed over two copper electrodes acting as a heat sink and electrical connector. Copper is chosen as the electrode due to its high thermal and electrical conductivity. The copper electrodes were cut in a way that the sample length can be chosen from 1mm to 10mm. These strips are then fixed over a glass slide by an adhesive to avoid movements during experiments. Due to the problem of oxidation of the copper, it is necessary to clean the strips with sand paper before use.

The fiber is placed over the two electrodes and stretched in order to have a straight sample making an accurate measurement of the length (Figure 1.19). The sample is then carefully attached with the electrode by using silver paste. Sufficient time is given for pasting until the electrical resistance remains constant. The sample holder is then connected with the rest of the electrical setup with the help of copper attachments shown in Figure 1.19 (c).

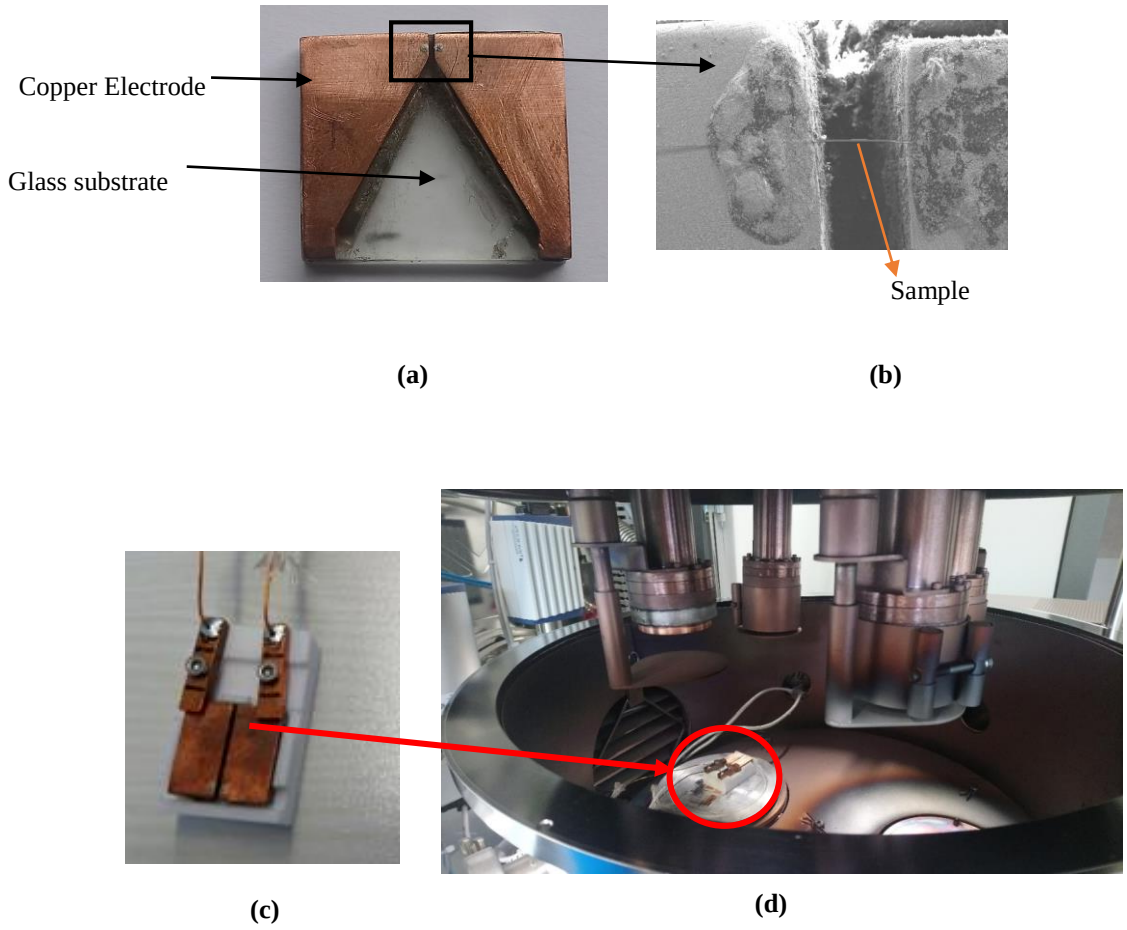


Figure 1.19: (a) Sample holder (b) zoomed image of fiber on the electrode (c) Sample with the electric connector (d) Vacuum chamber

5.4 Measurement Procedure

In order to retrieve the unknown thermal properties, fitting the analytical model with experimental results of $V_{3\omega\,rms}$ is only possible when each parameter involved in the analytical model (Eq. 1.26) is well measured. The values of I_{rms} and ω are noted from the current source KEITHLEY 6221 which is also acting as frequency generator. The resistance (R_X) is measured from the multi-meter externally connected with circuit. An accurate measurement of the parameters such as sample length (L) and diameter (D), is necessary. A Scanning Electron Microscope and a high-resolution optical camera were used to have an exact measurement of the sample diameter and length respectively. The length of the sample is also chosen in such a way that the frequency window of working is from 1 to 100 Hz. Table 4 shows the diameter and length of each sample that was be used in this thesis.

Type of fiber		Diameter/µm	Length/mm
FT300B	Sample 1	6.95-7.23	1.24
	Sample 2	6.69-7.01	1.34
	Sample 3	7.32-7.61	1.53
	Sample 4	6.99-7.62	1.76
FT800H	Sample 1	5.45-5.79	1.57
	Sample 2	5.34-5.89	1.28
Chromel		13.62	1.64

Table 4: Dimension of the samples used for 3ω measurement

After the successful measurement of each parameter, curve fitting tool of Matlab is used for fitting the $V_{3\omega\,rms}$ with the analytical model. The objective is to find a solution for the unknown thermal properties that minimizes the difference between the analytical model and experimental results. A built in Matlab algorithm Levenberg-Marquardt that uses nonlinear least squares method is applied for estimation of the thermal conductivity and heat capacity of the sample.

5.5 Temperature Coefficient of Resistance

The temperature coefficient of resistance (α_e) is still an unknown parameter for the implementation of the analytical model. It is the change in the resistance with 1-degree change in temperature of the sample.

$$\alpha_e = \frac{1}{R_0}\frac{(R - R_0)}{(T - T_0)} \tag{1.46}$$

α_e is the temperature coefficient of resistance in K^{-1}, R_0 is the initial resistance of the sample at initial temperature (T_0) in ohms and R is the current resistance at current temperature T. It is very important to measure the temperature coefficient of resistance correctly for better accuracy of the results. It can be achieved by varying the sample temperature gradually and according the variation in the electrical resistance. The following setup can be used to fulfill this objective.

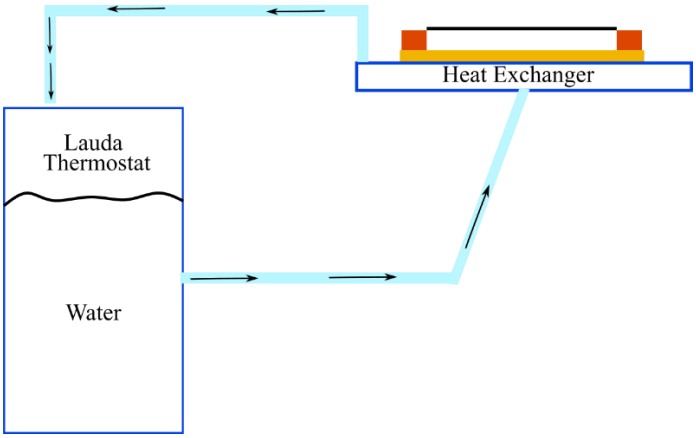


Figure 1.20: Schematic diagram for $\alpha_e$measurements.

A thermos-regulated bath (LAUDA) was used to supply the temperature controlled water through a parallel heat exchanger for heating the sample gradually with the elevation of 2K (Figure 1.20). A K-type thermocouple was welded at the electrode at closest vicinity to the sample to measure the exact temperature. Then a multi-meter was connected to measure the resistance through the sample with the change in temperature.

For each sample, i.e., 2 types of PAN carbon fibers and chromel wire, the temperature coefficient of resistance was measured. The value of α_e wass measured by changing the temperature of heat exchanger by varying the thermal baths between 12 and 32°C. Figure 1.21 shows the variation of resistance with the temperature rise for chromel wire and by linear fitting the experimental data we got α_e as 2.8 10^{-4} K^{-1}. A similar test was performed for the carbon fiber FT300B and FT800H. Table 5 shows the experimentaly measured value of α_e for the sample that were tested for 3ω method. The low temperature coefficient of chromel wire as compared to other metallic wires such as tungsten or platinum (Table 5) shows the difficulty to perform 3ω method as temperature measurement is an additional challenge.

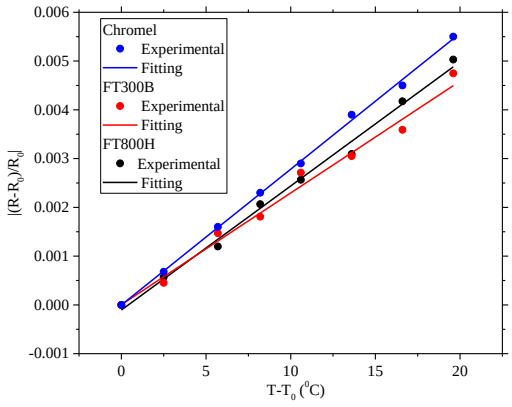


Figure 1.21: $\left|\frac{R-R_0}{R_0}\right|$ vs temperature rise for measuring α_e

Material	α_e (K^{-1})
Platinum	$3.9\ 10^{-3}$ [38]
Tungsten	$4.3\ 10^{-3}$ [38]
Chromel	$2.8\ 10^{-4}$ (experimental)
Carbon Fiber FT300B	$2.3\ 10^{-4}$(experimental)
Carbon Fiber FT800H	$2.5\ 10^{-4}$(experimental)

Table 5: α_e for different materials

6. Uncertainty Analysis

Despite the use of instruments with high accuracy, there are few uncertainties on known parameters such as length, diameter, current and etc. The model for estimation of the overall uncertainty on the thermal conductivity and heat capacity measurement through 3ω was presented by Milosevic[47].

$$S_{final} = [X^T\ W\ X]^{-1} \text{ with } W = \left[\sigma^2_{V_{3\omega\,rms}} + \sum_p (\sigma_{u_P} \frac{\partial V_{3\omega\,rms}}{\partial\, u_P})^2\right]^{-1} \quad (1.47)$$

where X is the sensitivity coefficient matrix, W is the variance covariance matrix, $\sigma_{V_{3\omega\,rms}}$ is the variance of measured $V_{3\omega\,rms}$, σ_{u_P} is the variance of the known parameters u_P, S_{final} is the matrix of variance and covariance. The values of σ_{m_p} can be estimated with the errors on the known parameters during measurements of $V_{3\omega\,rms}$ for chromel wire represented as ε_I=0.1%, ε_R=0.5%, ε_{α_e}=0.5%, ε_D=0.2%, ε_L=2.8%. During the measurements for carbon fiber, the error is similar to the chromel except in case of the diameter for which $\varepsilon_D = 5.1\%$ predicted from Table 4. The diagonal terms of S_{final} represent the variances $\sigma_{u_P}{}^2$ of the estimated parameters u_P (k or ρC_p) including the effect of the uncertainty of the known parameters. For a 95% confidence band, the relative uncertainty ε_{u_P} on parameter u_P is obtained using $\varepsilon_{u_P} = 1.96\ \sigma_{u_P}/u_P$.

7. Thermal Conductivity Measurements for Single Fiber

In this section, results for the measured axial thermal conductivities and volumetric heat capacity of carbon fibers are presented. Initially the results for validation of 3ω method and the experimental setup is shown using the chromel wire as a reference material. Then results implementing 3ω method for PAN carbon fibers are shown. As discussed in the section 5.3, it's very important to verify that the thermal contact resistance (TCR) between the sample and electrode is low or not. So the measurement of TCR is shown in the last section to correct the measured apparent thermal conductivity of the fiber.

7.1 Validation with Chromel Wire

A chromel wire with 13.62µm diameter and 1.62mm length was chosen to test the 3ω method. Its diameter was checked to be fairly constant with perfectly circular cross-section over the length. A 6mA current is passed through the sample and all the necessary experimental steps (section 5) are followed. Figure 1.22 shows the experimental test performed in vacuum for a

frequency range of 1 to 100 Hz. This data is fitted with the analytical model (Eq. 1.26) to estimate the axial thermal conductivity and volumetric heat capacity for chromel wire as shown in Table 6. The experiments conducted under vacuum showed very good agreement of the measured values for thermal conductivity and heat capacity with the reference values from the literature. The overall uncertainties in the measurement of thermal conductivity and heat capacity for chromel are ~2.9% and ~1.3% respectively (section 6). Furthermore the parameter estimation (Table 6) using the numerical model for vacuum are also consistent with previous results of analytical model.

In section 3.4 a hypothetical test case was shown that could quantify the effect of performing experiment under atmospheric conditions on the estimation of the axial thermal conductivity. In the experiments, further tests were carried out for justifying the initial hypothesis by performing experiments under atmospheric conditions. Figure 1.22 shows this experimental result for a frequency range of 1 to 100 Hz. The thermal conductivity estimated from the analytical model fitting with this experiment is very unrealistic and with a discrepancy of ~390% from the reference value (Table 6).

Using the numerical model for fitting experimental data required a correct prediction of the heat transfer coefficient. Although the diameter of the chromel wire is constant, the temperature rise in 3ω method is from 0.1K to 1K[48] and thus the heat transfer coefficient[39][40] was approximated to be ranging from 450-740 $Wm^{-2}K^{-1}$. The impact of the range of heat transfer coefficient is shown in the estimation of the thermal properties, leading the estimation of thermal conductivity to a range of value. Furthermore, it can be realized that the volumetric heat capacity estimation is not affected by the convective heat loss. In addition, one should note that the used correlations for heat transfer coefficient prediction [34][35] were established for steady state regimes and not for periodic ones as in the case of 3ω method. Otherwise without using correlations, one could have estimated simultaneously the thermal conductivity and the heat transfer coefficient but the sensitivity coefficients to these two parameters are strongly correlated. This was shown by the minimization of error between numerical and experiments give infinite number of minima that is a function of heat transfer coefficient and thermal conductivity. Thus, making simultaneous estimation of both unknown parameters impossible.

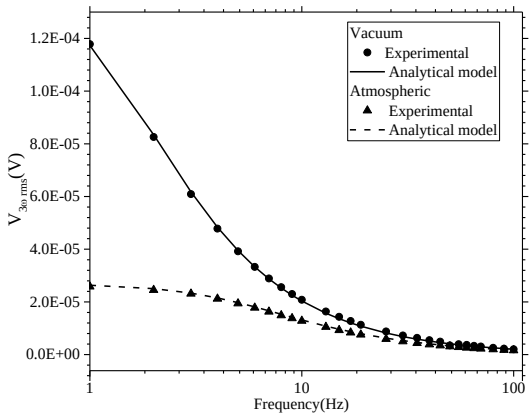


Figure 1.22: Measurements for chromel wire with vacuum and atmospheric conditions and fitting with analytical model

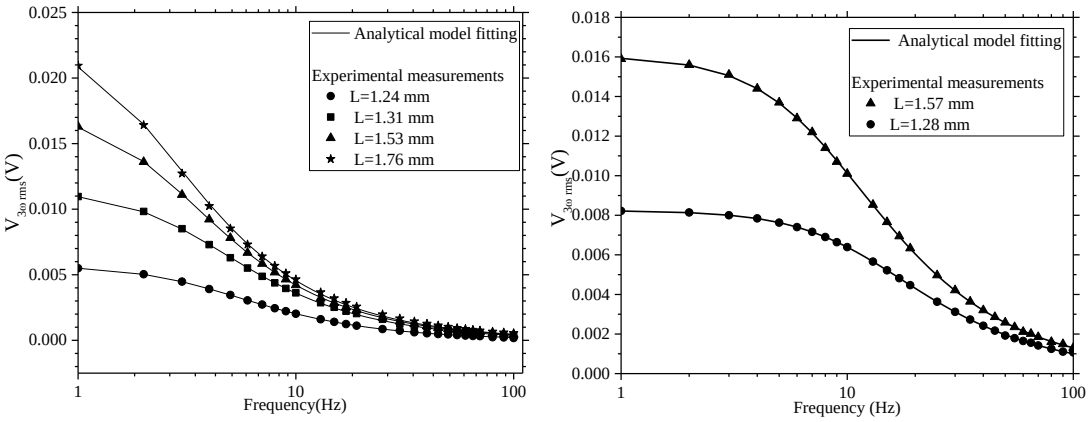
Thermal Properties		**Measured**		**Reference**[41][42]
		Analytical Model	**Numerical Model**	
k($Wm^{-1}K^{-1}$)	Vacuum	18.15	18.27	17.3
	Atmospheric	70.15	18.51*-25.82§	
ρC_P(MJ $m^{-3}K^{-1}$)	Vacuum	3.68	3.81	3.85
	Atmospheric	3.62	3.81*-3.83§	

Table 6: Thermal properties measured for chromel wire by fitting with the analytical model under vacuum and atmospheric conditions (* h=450, § h=740)

7.2 PAN Carbon Fibers

The 3ω method was then used to estimate the thermal properties for the two PAN carbon fibers FT300B and FT800H. From the study of experiments under atmospheric condition, it was quite obvious that the convective loss played a huge role in the estimation of thermal properties by 3ω method. Additionally the small diameter and irregular cross section (Figure 1.18) of the carbon fiber makes the prediction of thermal conductivity extremely more sensitive to the convective heat losses. Thus the 3ω method for carbon fibers were only tested under vacuum as shown in Figure 1.19(c).

For FT300B and FT800H carbon fibers multiple samples with different lengths (Table 4) were tested. The experimental results for $V_{3\omega\ rms}$ are highly reproducible for each sample. Figure 1.23 shows the experimental $V_{3\omega\ rms}$ with a 1 to 100 Hz frequency range performed in a vacuum chamber by passing 1mA of current on different fibers. Four samples of FT300B and two samples FT800H were tested with 3ω method. After analytical model fitting, the thermal conductivity and heat capacity for the carbon fibers are estimated and compared with the data provided by the fiber supplier (Toray Industries) as shown in Table 7. The uncertainties in the measurement of thermal conductivity and heat capacity are ~8.1% and ~4.9% respectively for these carbon fibers, as estimated from the uncertainty analysis described in section 6.



(a) (b)

Figure 1.23: (a) Measurements for FT300B carbon fiber with vacuum and multiple sample lengths, (b) Measurements for FT800HB carbon fiber with vacuum for a sample length of 1.56mm and 1.28mm.

	FT300B				**Reference**[43]
Thermal Properties	Sample 1	Sample 2	Sample 3	Sample 4	Supplier datasheet
k($Wm^{-1}K^{-1}$)	10.11	10.03	10.17	10.28	10.47
ρC_P(MJ $m^{-3}K^{-1}$)	1.35	1.38	1.37	1.37	1.39
	FT800H				
k($Wm^{-1}K^{-1}$)	34.59	34.88			35.13
ρC_P(MJ $m^{-3}K^{-1}$)	1.37	1.37			1.36

Table 7: Thermal properties estimation for carbon fibers.

7.3 Thermal Contact Resistance between sample and copper electrodes

The analytical and numerical models work with an assumption of perfect thermal contact between the sample and copper electrodes, which is impossible to achieve in practice. Therefore an estimation of thermal contact resistance was done from the measured values of thermal conductivity with different sample lengths. For each sample the overall thermal resistance (L/k) is calculated. Figure 1.26 shows the variation of the overall thermal resistance with length for the fiber FT300B.

The measured thermal resistances can be fitted with a linear regression. The y intercept of this plot gives the thermal resistance when the fiber length is 0 that can be interpreted as the global thermal contact resistance with the value of 8.83 10^{-6} m^2KW^{-1}. This value is compared with the intrinsic thermal resistance at each length of the carbon fiber sample (~10^{-4} m^2KW^{-1}). In the 3ω method, overall effect of the thermal contact resistance (TCR) over the thermal resistance (TR) at each length, therefore less than 7% (~TCR/TR). The inverse of the slope of the linear regression provides the final value of the thermal conductivity of the FT300B carbon fiber which is equal to 10.82 $Wm^{-1}K^{-1}$.

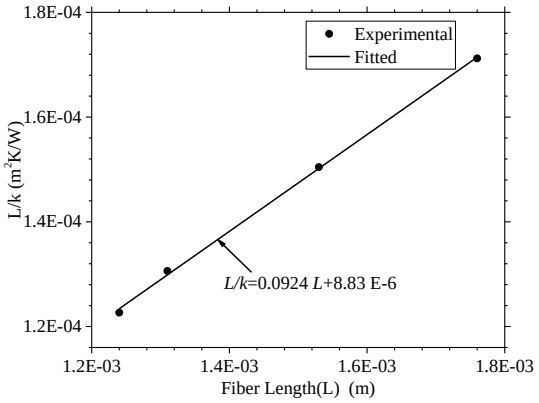


Figure 1.24: Thermal resistance vs length for FT300B

8. Partial Conclusions

In this chapter, the 3ω method is used for estimating the axial thermal conductivity and volumetric heat capacity of single carbon fiber. A detailed derivation of the analytical model from Lu et al.[10] demonstrated that it can work by imposing multiple mathematical and physical assumptions. These assumptions are imposed in terms of the pre-requisites that are necessary to perform 3ω test on any sample. Due to the application of analytical model, which is limited by the assumption of surrounding as a vacuum, it is crucial to quantify the effect of convection in 3ω method. Thus a complete numerical model was developed that can take into account not only the periodic heating due to the alternating current but also the convective heat loss. The comparison between the analytical and numerical model was done by calculating the 3ω response for same working conditions. Despite multiple assumptions of analytical model under vacuum, it was observed that the 3ω response from the numerical model is remarkably similar except for a lower frequency with a difference of less than 1.6%. This result emphasized in validation of the analytical model for our experimental setup under vacuum.

Even though most research in the literature focused on simplifying the analytical model for making estimation of each parameters in different frequency range, our focus was to use the complete analytical model for estimating the axial thermal conductivity along with heat capacity simultaneously. This was possible by selecting a proper frequency window. To determine the working frequency window for our experiments, a sensitivity analysis was done over each sample and it was observed that the length of the sample is an important factor. Thus an optimum length was chosen where the sensitivity of each unknown parameter is high.

For carrying out the experiments a constant current source with differential amplifier was used to extract the 3ω response of the voltage. The setup for 3ω method was validated by performing test on chromel wire under vacuum. The results showed a good agreement of the estimated thermal conductivity and heat capacity with the values from literature. The importance of experimenting only under vacuum condition was proven by quantifying the influence of convective loss on the estimation of thermal conductivity using this analytical model. It showed an increase in the estimated thermal conductivity value by 390% from the literature. Although the numerical model can somehow take into account the convective losses, the wide range value of heat transfer coefficient from known correlation makes the estimation of thermal conductivity is very questionable. For carbon fiber this problem becomes more prominent due to the smaller and varying diameter of the fiber.

The thermal properties of carbon fiber of type FT300B and FT800H are also estimated using 3ω method under vacuum. They are found out to be consistent with the data from literature and supplier. The higher uncertainty in the measurement for carbon fibers is mainly due to the discrepancy of the diameter through the length of samples. At the end, the uncertainty due to the thermal contact between the fiber and sample holder is also studied. The sum of the two thermal contact resistances at both fiber ends was also estimated to be less than 7% of the overall sample thermal resistance thus the influence on the measurement of thermal conductivity is small.

From this chapter, the application of 3ω method to estimating axial thermal conductivity is successfully studied. But for full characterization of thermal properties for carbon fiber, it is extremely important to work not only on the axial but also on the radial heat transfer. In the next chapter the application of 3ω method to estimating the radial thermal conductivity is discussed.

References

[1] Chand S 2000 Carbon fibers for composites *J. Mater. Sci.* **35** 1303–13

[2] Sweeting R D and Liu X L 2004 Measurement of thermal conductivity for fibre-reinforced composites *Compos. Part A Appl. Sci. Manuf.* **35** 933–8

[3] Selvakumar M, Ramkumar T and Chandrasekar P 2019 Thermal characterization of titanium--titanium boride composites *J. Therm. Anal. Calorim.* **136** 419–24

[4] Manocha L M, Warrier A, Manocha S, Sathiyamoorthy D and Banerjee S 2006 Thermophysical properties of densified pitch based carbon/carbon materials-I. Bidirectional composites *Carbon N. Y.* **44** 488–95

[5] Siddiqui M O R and Sun D 2018 Development of Experimental Setup for Measuring the Thermal Conductivity of Textiles *Cloth. Text. Res. J.* **36** 215–30

[6] Craddock J D, Burgess J J, Edrington S E and Weisenberger M C 2016 Method for Direct Measurement of On-Axis Carbon Fiber Thermal Diffusivity Using the Laser Flash Technique *J. Therm. Sci. Eng. Appl.* **9** 014502

[7] Gallego N C, Edie D D, Ntasin L N and Ervin V J 2000 Modeling the thermal conductivity of carbon fibers *Carbon N. Y.* **38** 1003–10

[8] Wang J L, Gu M, Zhang X and Song Y 2009 Thermal conductivity measurement of an individual fibre using a T type probe method *J. Phys. D. Appl. Phys.* **42**

[9] Yamane T, Katayama S I, Todoki M and Hatta I 1996 Thermal diffusivity measurement of single fibers by an ac calorimetric method *J. Appl. Phys.* **80** 4358–65

[10] Lu L, Yi W and Zhang D L 2001 3 ω method for specific heat and thermal conductivity measurements *Rev. Sci. Instrum.* **72** 2996–3003

[11] Lorrette C 2007 *Outils de caracterisation thermophysique et mod_eles numeriques pour les composites thermostructuraux a haute temperature* (Université Bordeaux 1)

[12] Huang X 2009 Fabrication and properties of carbon fibers *Materials (Basel).* **2** 2369–403

[13] Dobbins T 2019 *State of the Industry Report* vol 35 (Arlington)

[14] Pradère C, Goyhénèche J M, Batsale J C, Dilhaire S and Pailler R 2006 Thermal diffusivity measurements on a single fiber with microscale diameter at very high temperature *Int. J. Therm. Sci.* **45** 443–51

[15] Pradere C, Batsale J C, Goyhénèche J M, Pailler R and Dilhaire S 2009 Thermal properties of carbon fibers at very high temperature *Carbon N. Y.* **47** 737–43

[16] Liu J, Qu W, Xie Y, Zhu B, Wang T, Bai X and Wang X 2017 Thermal conductivity and annealing effect on structure of lignin-based microscale carbon fibers *Carbon N. Y.* **121** 35–47

[17] Zhu Y 2016 Heat-loss modified Angstrom method for simultaneous measurements of thermal diffusivity and conductivity of graphite sheets: The origins of heat loss in Angstrom method *Int. J. Heat Mass Transf.* **92** 784–91

[18] Yamane T, Mori Y, Katayama S I and Todoki M 1997 Measurement of thermal diffusivities of thin metallic films using the ac calorimetric method *J. Appl. Phys.* **82** 1153–6

[19] Sinha S, Barjami S, Iannacchione G, Schwab A and Muench G 2005 Off-axis thermal properties of carbon nanotube films *J. Nanoparticle Res.* **7** 651–7

[20] Wang J, Song B, Zhang X, Song Y and Wu G 2011 Simultaneous measurements of thermal properties of individual carbon fibers *Int. J. Thermophys.* **32** 974–83

[21] Wang J, Gu M, Ma W, Zhang X and Song Y 2008 Temperature dependence of the thermal conductivity of individual pitch-derived carbon fibers *New Carbon Mater.* **23** 259–63

[22] Pradere C and Sauder C 2008 Transverse and longitudinal coefficient of thermal expansion of carbon fibers at high temperatures (300-2500 K) *Carbon N. Y.* **46** 1874–84

[23] Pradère C, Goyhénèche J M, Batsale J C, Dilhaire S and Pailler R 2005 Specific-heat measurement of single metallic, carbon, and ceramic fibers at very high temperature *Rev. Sci. Instrum.* **76** 4–6

[24] Corbino O M 1912 Measurement of specific heats of metals at high temperatures *Atti della R. Accad. Naz. dei Lincei* **21** 181–8

[25] Cahill D G and Pohl R O 1987 Thermal conductivity of amorphous solids above the plateau *Phys. Rev. B* **35** 4067–73

[26] Cahill D G 1990 Thermal conductivity measurement from 30 to 750 K: The 3ω method *Rev. Sci. Instrum.* **61** 802–8

[27] Tian T and Cole K D 2012 Anisotropic thermal conductivity measurement of carbon-fiber/epoxy composite materials *Int. J. Heat Mass Transf.* **55** 6530–7

[28] Boussatour G, Cresson P Y, Genestie B, Joly N, Brun J F and Lasri T 2018 Measurement of the thermal conductivity of flexible biosourced polymers using the 3-omega method *Polym. Test.* **70** 503–10

[29] Bogner M, Hofer A, Benstetter G, Gruber H and Fu R Y Q 2015 Differential 3ω method for measuring thermal conductivity of AlN and Si<inf>3</inf>N<inf>4</inf> thin films *Thin Solid Films* **591** 267–70

[30] Nadine Al-Khudary 2014 M*aterial thermal conductiviy measurement by the 3-omega method application to polymer characterization using inkjet printing technology* (Univ. Lille)

[31] Schiffres S N and Malen J A 2011 Improved 3-omega measurement of thermal conductivity in liquid, gases, and powders using a metal-coated optical fiber *Rev. Sci. Instrum.* **82**

[32] Gauthier S, Giani A and Combette P 2013 Gas thermal conductivity measurement using the three-omega method *Sensors Actuators, A Phys.* **195** 50–5

[33] Zhao L, Luo Y, Huang X, Zhou X, Hebibul R, Ding J, Li Z and Jiang Z 2019 A novel microsensor for measuring thermal conductivity of fluid based on three omega method *Rev. Sci. Instrum.* **90**

[34] Dames C and Chen G 2005 1Ω, 2Ω, and 3Ω Methods for Measurements of Thermal Properties *Rev. Sci. Instrum.* **76** 1–14

[35] Wang Z L, Tang D W and Zhang W G 2007 Simultaneous measurements of the thermal conductivity, thermal capacity and thermal diffusivity of an individual carbon fibre *J. Phys. D. Appl. Phys.* **40** 4686–90

[36] Xing C, Jensen C, Munro T, White B, Ban H and Chirtoc M 2014 Accurate thermal property measurement of fine fibers by the 3-omega technique *Appl. Therm. Eng.* **73** 315–22

[37] Xing C, Jensen C, Munro T, White B, Ban H and Chirtoc M 2014 Thermal property characterization of fine fibers by the 3-omega technique *Appl. Therm. Eng.* **71** 589–95

[38] Liang J 2014 *Experimental measurement and modeling of thermal conductivities of carbon fibers and their composites modified with carbon nanofibers* (University of Oklahoma)

[39] Morgan V T 1975 The Overall Convective Heat Transfer from Smooth Circular Cylinders. *Adv. Heat Transf.* **11** 199–264

[40] Boetcher S K S 2014 Natural convection transfer from horizontal cylinders *SpringerBriefs Appl. Sci. Technol.* 23–42

[41] Sundqvist B 1992 Thermal diffusivity and thermal conductivity of Chromel, Alumel, and Constantan in the range 100-450 K *J. Appl. Phys.* **72** 539–45

[42] Omega Engineering 2005 Physical Properties of Thermoelement Materials

[43] Sheet D Torayca® T300 Data Sheet. Available online http://www.toraycfa.com/pdfs/T300DataSheet.pdf ; last retrieved on February 11th 2013. at: 6–7

[44] Chapelle E, Garnier B and Bourouga B 2009 Interfacial thermal resistance measurement between metallic wire and polymer in polymer matrix composites *Int. J. Therm. Sci.* **48** 2221–7

[45] AMETEK 2002 Model 7265 DSP Lock-in Amplifier *Manual*

[46] AMTEK Advanced Measurment Technology Inc. The Digital Lock-in Amplifier, TN-1003 *Measurement* 1–4

[47] Milošević N D, Raynaud M and Maglić K D 2002 Estimation of thermal contact resistance between the materials of double-layer sample using the laser flash method *Inverse Probl. Eng.* **10** 85–103

[48] Lu L, Yi W and Zhang D L 2001 3ω method for specific heat and thermal conductivity measurements *Rev. Sci. Instrum.* **72** 2996–3003

Chapter 2

Application of the 3ω method to the Radial Thermal Conductivity of single carbon fibers

1. Introduction 45
2. Literature review 45
3. 3*ω* method 47
4. Models for determining radial thermal conductivity 47
4.1 Analytical 1D Radial Model 47
4.2 Numerical Finite Difference 1D Model 51
4.3 Numerical Finite Element 2D Model 53
4.4 Comparison between analytical, numerical 1D and numerical 2D 54
5. Sensitivity Analysis 55
6. Experimental test for radial thermal conductivity 56
6.1 Fitting with 1D analytical model 56
6.2 Fitting with 2D finite element model 57
7. Partial Conclusion 59
References 60

1. Introduction

A large part of the composite materials used in the industry today is composed of carbon fibers impregnated within a thermosetting or thermoplastic matrix. In most composite applications or composite manufacturing problems, one considers quite thin parts (plates or shells) where the dominant mode of heat transfer is in the transverse (out-of-plane) direction. In this transverse conduction mode, the radial conductivity of fibers is of major importance. It is thus necessary to estimate not only the axial thermal conductivity but also the radial thermal conductivity of the fiber. Despite the high interest of determining the anisotropic features of the carbon fibers, the experimental determination of the radial thermal conductivity of a single fiber is still a big challenge within the research community.

In this chapter, the objective was to verify the possibility of using the 3ω method for radial thermal conductivity measurement. In reference to the thesis of Liang[1], a similar analytical model is shown in section 4.1. A 1D numerical model was also developed that could validate the analytical model (section 4.2). A 2D finite element model is developed using Comsol (section 4.3) to check the presence of longitudinal temperature gradient as it could influence the estimation of radial thermal conductivity. A sensitivity analysis was done to choose the working frequency window to obtain higher accuracy in the measurement (section 5). An experimental work was also executed on the single fiber FT300B to estimate the radial thermal conductivity and to check the accuracy of its measurement (section 6).

2. Literature review

Previous researches mostly focused on the effective transversal conductivity at the scale of composite[2–5] and rather less focus was given to the microscale properties. In the literature, only a couple of experimental approaches are present for the determination of the radial thermal conductivity of a single fiber. In the research article by Huang et al [6], the transverse thermal conductivity of a pitch-based carbon fiber was measured by a custom-designed thermal conductivity measurement system based on steady-state heat flux measurement (ASTM C177-10) [7]. In the ASTM standard technique, the measured specimen is positioned between two reference heaters held at two different temperatures using thermal grease to reduce the interfacial thermal contact resistance between the specimen and the heaters. The sensors are placed along the lengths of the test specimen and yield information on the rate of heat flow through two reference materials of known conductivities. The rate of heat flow can then be used to determine the thermal conductivity of the unknown specimen using the one-dimensional Fourier's conduction equation.

They also computed the in plane and out of plane thermal conductivity of graphite sheets using molecular dynamics and then implementing this data to compute transverse thermal conductivity for individual fiber using a FEM resolution. Although, this method seems to have multiple counts of

thermal resistance, however, no exact estimation of thermal contact resistance was provided. Moreover, no details was provided about the precision of the experimental setup during measurement.

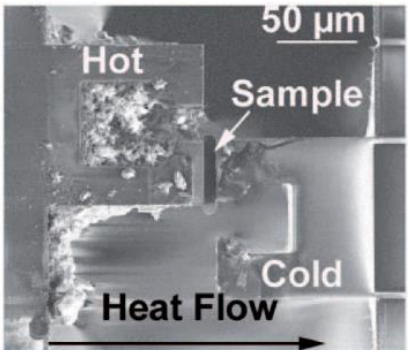


Figure 2.1: Simplified schematic diagram of the measurement procedure by Huang et al.

Recently in 2019, a paper of Wang et al [8] presents anisotropic thermal conductivity tensor of lignin based fiber was measured. The transient electro thermal technique was used for the measurement of the axial thermal conductivity (k_a) and of the volumetric heat capacity (ρC_p). Then this data was used to determine the radial thermal conductivity (k_r) by using frequency domain energy transport (FET) state Raman method. Figure 2.2 shows the basic illustration of FET Raman method. Two types of laser are passed through the sample, i.e. continuous wave (CW) and frequency modulated wave (FR). From this two Raman shift coefficients (Ψ) are obtained. These two factors are normalized (Θ) for cancelling the effect of laser absorption coefficient and temperature coefficient and finally obtaining a term dependent only on k_r, $k_a$and ρC_p. The limitation of this technique was concerned to the measurement of k_r . A high uncertainty in the measurement of k_r was observed at different axial position of the fiber sample. Moreover the repeatability of the results for different samples were not achieved during the experiments.

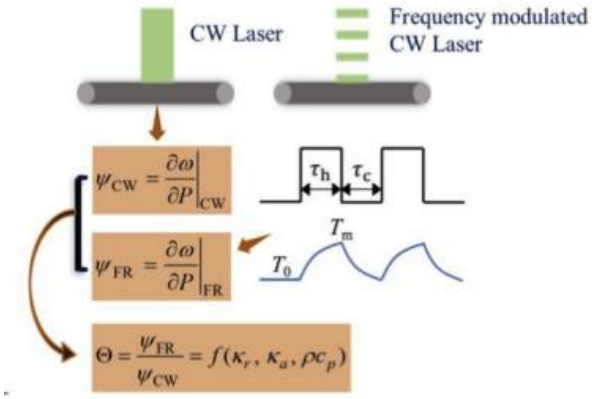


Figure 2.2: Illustration of FET Raman method [8]

3. 3ω method

In the year 2014 Liang et al[1] used the 3ω method for measuring the radial thermal conductivity by developing an analytical model describing radial heat transfer and remodeling the experimental setup that was used for the longitudinal thermal conductivity measurement. They placed the sample in a surrounding medium of deionized water to induce radial heat transfer while maintaining an electrical insulation. The deionized waters also acts as a controlling environment and an infinite medium surrounding the fiber.

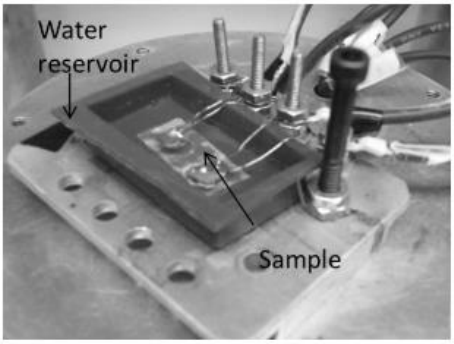


Figure 2.3: Water reservoir used in the thesis of Liang[1]

Although the experimental setup was validated by the metallic wires with less than 5% difference from the literature value, there was no test provided to ensure the absence of longitudinal temperature gradient. Furthermore, no sensitivity analysis was done to determine the working frequency window for the 3ω method and surprisingly the same frequency range as for the longitudinal thermal conductivity was used. Subsequently, in this work, the possibility of using the 3ω method for the radial thermal conductivity was investigated by developing numerical models and performing an experimental test on a single PAN fiber. The water reservoir used for the sample was similar to the one used in the thesis of Liang and rest of the experimental setup is the same as the one described in chapter 1 for the measurement of the longitudinal thermal conductivity.

4. Models for determining radial thermal conductivity

4.1 Analytical 1D Radial Model

This section provides a brief introduction of the analytical model for the 3ω voltage response of a self-heating fiber depending on the imposed frequency (ω) with dominating radial transfer. Like the axial direction dominated heat transfer discussed in the previous chapter, this model also assumes that the specimen is a uniform cylinder placed between two heat sinks (copper electrodes). An alternating electrical current ($I_0 \sin(\omega t)$) with a frequency ω is passed through the sample of radius a that has an electrical resistance R and a length L. The schematic diagram of the sample submerged in de-ionized water is shown in Figure 2.4.

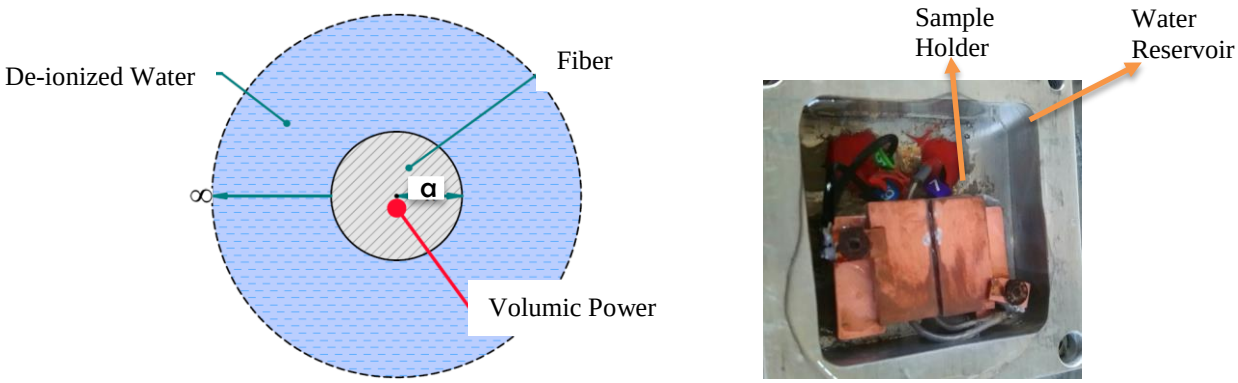


Figure 2.4: (a) Schematic diagram of a fiber in water (b) Sample holder in water reservoir

In the thesis of Liang[1], an analytical model for 1D heat conduction along the radial by the assumption of infinite long cylinder in an infinite medium was developed. He makes the assumption of constant thermal conductivity along the radial direction and continuity of temperature along the interface between the fiber and the surrounding medium. He also assumes no radiative nor convective heat losses. The radial heat transfer equation with a power generation from passing alternating current through the sample can be written as follows:

$$\rho C_P \frac{\partial}{\partial t} T_1(r,t) - k_R \left(\frac{\partial^2 T_1}{\partial r^2} + \frac{1}{r} \frac{\partial T_1}{\partial r} \right) = P \tag{2.1}$$

where k_R is the radial thermal conductivity, ρC_P volumetric heat capacity of fiber and P is the volumetric electrical power source. The heat transfer equation for water with thermal conductivity k_w and volumetric heat capacity $\rho_w C_{p\,w}$ reads:

$$\rho_w C_{p\,w} \frac{\partial}{\partial t} T_2(r,t) - k_w \left(\frac{\partial^2 T_2}{\partial r^2} + \frac{1}{r} \frac{\partial T_2}{\partial r} \right) = 0 \tag{2.2}$$

The boundary and initial condition are:

$$\begin{cases} at\ r = a:\ T_1 = T_2\ and\ \ k_R \left. \dfrac{\partial T_1}{\partial r} \right|_a = k_W \left. \dfrac{\partial T_2}{\partial r} \right|_a \\ at\ r \to \infty:\ T_2 = T_0 \\ at\ t = 0: T_1 = T_2 = T_0 \end{cases} \tag{2.3}$$

T_1 and T_2 are the respective temperature of the sample and surrounding water at position r and time t. Focusing now only in the temperature fluctuations around the average value, we take a similar approach to the one described in chapter 1 and use the notion of complex temperature $T = \tilde{T}\, e^{2j\omega t}$ with power $P = \tilde{P}\, e^{2j\omega t}$ to transform the system of equations in Fourier's space. The space and time derivatives in Eq. 2.1 and 2.2 therefore become

$$\frac{\partial T}{\partial r} = \frac{\partial \tilde{T}}{\partial r} e^{2\omega jt}, \frac{\partial^2 T}{\partial r^2} = \frac{\partial^2 \tilde{T}}{\partial r^2} e^{2\omega jt}, \frac{\partial \mathrm{T}}{\partial \mathrm{t}} = 2\omega \mathrm{j}\tilde{\mathrm{T}} e^{2\omega jt} \tag{2.4}$$

For periodic regimes, Eq. 2.1 becomes:

$$\frac{\partial^2 \widetilde{T_1}}{\partial r^2} + \frac{1}{r}\frac{\partial \widetilde{T_1}}{\partial r} - \frac{2\omega j \widetilde{T_1} \rho_R C_{P_R}}{k_R} = -\frac{\tilde{P}}{k_R} \tag{2.5}$$

If $u = \alpha_1 r$, Eq. 2.5 can be written as

$$\frac{\partial^2 \widetilde{T_1}}{\partial u^2} + \frac{1}{u}\frac{\partial \widetilde{T_1}}{\partial u} - \widetilde{T_1} = -\frac{\tilde{P}}{\alpha_1^2 k_R} \tag{2.6}$$

The solution without a 2nd member is provided by Bessel's functions:

$$\widetilde{T_1} = A_3 I_0(\alpha_1 r) + A_4 K_0(\alpha_1 r), \qquad \widetilde{T_2} = A_1 I_0(\alpha_2 r) + A_2 K_0(\alpha_2 r) \tag{2.7}$$

where I_0 and K_0 are the first and second kind modified Bessel functions respectively and the equation for the constants α_1 and α_2 are defined in Eq. 2.23 and 2.24 respectively. In the following, the mathematical derivations for A_1, A_2, A_3, A_4 is provided so that Eq. 2.7 can be used directly for the solution. Using boundary conditions for $\widetilde{T_2}$, we have

$$\lim_{r\to\infty} I_0(\alpha_2 r) = +\infty, \quad \lim_{r\to\infty} K_0(\alpha_2 r) = 0 \tag{2.8}$$

$\widetilde{T_2}$ can be further solved as

$$\begin{cases} A_1 = 0 \\ \widetilde{T_2} = A_2 K_0(\alpha_2 r) \end{cases} \tag{2.9}$$

For $\widetilde{T_1}$ with the 2nd member (source term), we have:

$$at\ r = 0 \quad \frac{d\widetilde{T_1}}{du} = 0, \qquad at\ r = a \quad \widetilde{T_1}(R) = \widetilde{T_2}(R)\ and\ k_R \frac{d\widetilde{T_1}}{dr} = k_W \frac{d\widetilde{T_2}}{dr} \tag{2.10}$$

With the 2nd member the particular solution is

$$\widetilde{T_1} = \frac{\tilde{\mathrm{P}}}{\alpha_1^2 \mathrm{k_R}} \tag{2.11}$$

Therefore for $\widetilde{T_1}$ the solution is

$$\widetilde{T_1} = A_3 I_0(\alpha_1 r) + A_4 K_0(\alpha_1 r) + \frac{\tilde{\mathrm{P}}}{\alpha_1^2 \mathrm{k_R}} \tag{2.12}$$

With the boundary conditions we have at r=0, u=0 and $A_4 = 0$:

$$\widetilde{T_1} = A_3 I_0(\alpha_1 r) + \frac{\tilde{\mathrm{P}}}{\alpha_1^2 \mathrm{k_R}} \tag{2.13}$$

If we use the interfacial boundary conditions $\widetilde{T_1}(a) = \widetilde{T_2}(a)$ we have

$$A_3 I_0(\alpha_1 r) + \frac{\widetilde{\mathrm{P}}}{\alpha_1^2 \mathrm{k_R}} = A_2 K_0(\alpha_2 r) \tag{2.14}$$

$$k_R \left.\frac{\partial T_1}{\partial r}\right|_a = k_W \left.\frac{\partial T_2}{\partial r}\right|_a \rightarrow k_R A_3 \alpha_1 I_1(\alpha_1 a) = k_W A_2 \alpha_2 \left(-K_1(\alpha_2 a)\right) \tag{2.15}$$

$$\frac{A_2}{A_3} = -\frac{k_R \alpha_1 I_1(\alpha_1 a)}{k_W \alpha_2 K_1(\alpha_2 a)} \tag{2.16}$$

Eq. 2.14 transforms to

$$\frac{\widetilde{\mathrm{P}}}{A_3 \alpha_1^2 \mathrm{k_R}} = \frac{A_2}{A_3} K_0(\alpha_2 a) - I_0(\alpha_1 a) = -\frac{k_R \alpha_1 I_1(\alpha_1 a)}{k_W \alpha_2 K_1(\alpha_2 a)} K_0(\alpha_2 a) - I_0(\alpha_1 a) \tag{2.17}$$

Therefore A_3 is

$$A_3 = -\frac{\widetilde{\mathrm{P}}}{\xi \alpha_1^2 \mathrm{k_R} I_1(\alpha_1 a)}, \qquad \text{with} \quad \xi = \frac{k_R \alpha_1 K_0(\alpha_2 a)}{k_W \alpha_2 K_1(\alpha_2 a)} + \frac{I_0(\alpha_1 a)}{I_1(\alpha_1 a)} \tag{2.18}$$

and the expression of temperature becomes

$$\widetilde{T_1} = -\frac{\widetilde{\mathrm{P}} I_0(\alpha_1 a)}{\xi \alpha_1^2 \mathrm{k_R} I_1(\alpha_1 a)} + \frac{\widetilde{\mathrm{P}}}{\alpha_1^2 \mathrm{k_R}} \tag{2.19}$$

The corresponding analytical solution for the average temperature rise $\overline{\widetilde{T_1}}$ in the fiber with imposed frequency ω can be written as:

$$\widetilde{T_1} = -\frac{\widetilde{\mathrm{P}} I_0(\alpha_1 a)}{\xi \alpha_1^2 \mathrm{k_R} I_1(\alpha_1 a)} + \frac{\widetilde{\mathrm{P}}}{\alpha_1^2 \mathrm{k_R}} \tag{2.20}$$

$$\overline{\widetilde{T_1}} = \frac{1}{\pi a^2} \int_0^a \widetilde{T_1} 2\pi r dr = \frac{2\pi}{\pi a^2} \left[\int_0^a \frac{A_3 I_0(\alpha_1 r) \alpha_1}{\alpha_1} r dr + \int_0^R \frac{\widetilde{\mathrm{P}}}{\alpha_1^2 \mathrm{k_R}} r dr \right] \tag{2.21}$$

$$\overline{\widetilde{T_1}} = \frac{\tilde{P} a^2}{\alpha_1^2 k_R} \left[1 - \frac{2}{\xi \alpha_1} \right] \tag{2.22}$$

where

$$\alpha_1 = \sqrt{\frac{2\omega j}{a_1}} = \frac{(1+j)}{\delta_1}, \qquad \delta_1 = \sqrt{\frac{k_R}{\omega \rho_R C_{P_R}}} = \sqrt{\frac{2k_R}{4\pi f \rho_R C_{P_R}}} \tag{2.23}$$

$$\alpha_2 = \sqrt{\frac{2\omega j}{a_2}} = \frac{(1+j)}{\delta_2}, \delta_2 = \sqrt{\frac{k_W}{\omega \rho_W C_{P_W}}} = \sqrt{\frac{2k_W}{4\pi f \rho_W C_{P_W}}} \tag{2.24}$$

From this data, the 3ω fluctuations of voltage can be estimated as

$$V_{3\omega\,rms} = I_{rms}R'\left\|\widetilde{\overline{T_1}}\right\| \tag{2.25}$$

Again fitting this model with the experimental results may provide the estimation of the radial thermal conductivity (k_R) of the specimen. Eq. 2.25 is similar to the one for the analytical model developed by Liang [1] if we correct the definition of γ - top of p. 63 in his PhD report. Indeed in Liang's PhD, one can notice a mistake: the index of the two materials for the thermal diffusivity ratio should be permuted, due to the implementation of the inner boundary condition at $r=a$.

4.2 Numerical Finite Difference 1D Model

A numerical model was developed to analyze the radial heat transfer by 3ω method, similar to the one for the longitudinal heat transfer, with the objective of validating the analytical radial model. For a system with radial direction dominated heat transfer, finite difference method was used to solve the 3ω voltage response for the fiber submerged in de-ionized water.

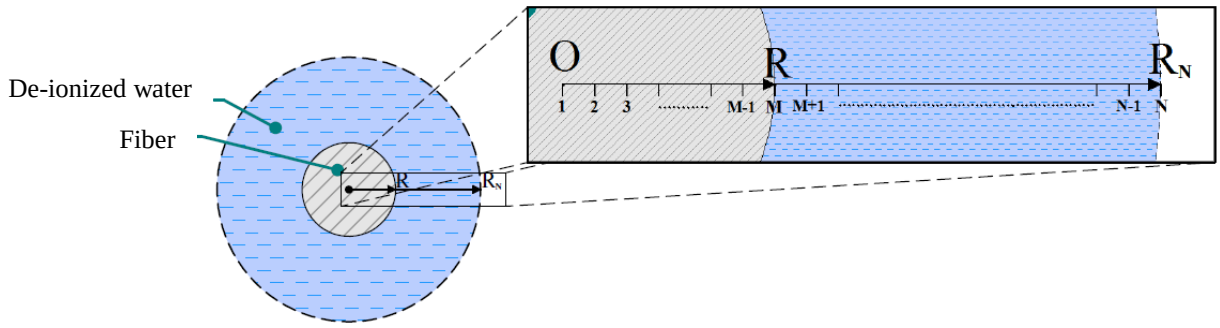


Figure 2.5: Schematic diagram for numerical model in 1D for the fiber in water

In the case of constant thermophysical parameters, the heat transfer can be described by the following polar coordinate partial differential equation with k dependent on the position (fiber or water) and P only present in the fiber:

$$\rho C_p \frac{\partial}{\partial t} T(r,t) - k\left(\frac{\partial^2 T}{\partial r^2} + \frac{1}{r}\frac{\partial T}{\partial r}\right) = P \tag{2.26}$$

As detailed previously, the complex form of the above equation is

$$\frac{\partial^2 \tilde{T}}{\partial r^2} + \frac{1}{r}\frac{\partial \tilde{T}}{\partial r} - \frac{2\omega j\tilde{T}}{a_1} = -\frac{\tilde{P}}{k} \tag{2.27}$$

With central discretization of $\tilde{T}$

$$\frac{\partial^2 \tilde{T}}{\partial r^2} = \frac{\tilde{T}_{i+1} - 2\tilde{T}_1 + \tilde{T}_{i+1}}{\Delta r^2}, \frac{\partial \tilde{T}}{\partial r} = \frac{\tilde{T}_{i+1} - \tilde{T}_{i-1}}{2\Delta r} \tag{2.28}$$

where, I = 1,2,3…. are the number of nodes starting from 1 (i.e. the center of the fiber cross-section shown in Figure 2.5). Since, $T = \tilde{T}e^{2\omega jt}$; $P = \tilde{P}e^{2\omega jt}$ and using central difference of T on r, the Eq. 2.27 can be simplified

$$\frac{\tilde{T}_{i+1} - 2\tilde{T}_1 + \tilde{T}_{i-1}}{\Delta r^2} + \frac{1}{r}\frac{\tilde{T}_{i+1} - \tilde{T}_{i-1}}{2\Delta r} = -\frac{\tilde{P}}{k} + j\frac{2\omega}{a_1}\tilde{T}_i \tag{2.29}$$

$$\left(1 - \frac{\Delta r}{2r}\right)\tilde{T}_{i-1} - 2\left(1 + j\frac{2\omega}{a_1}\Delta r^2\right)\tilde{T}_i + \left(1 + \frac{\Delta r}{2r}\right)\tilde{T}_{i+1} = -\frac{\tilde{P}}{k}\Delta r^2 \tag{2.30}$$

It can be further simplified as

$$(1 - \Theta)\tilde{T}_{i-1} + \beta\tilde{T}_i + (1 + \Theta)\tilde{T}_{i+1} = \Omega \tag{2.31}$$

where

$$\Theta = \frac{\Delta r}{2r},\ \beta_1 = -2\left(1 + j\frac{\omega\rho C_p}{k_R}\Delta r^2\right),\ \beta_2 = -2\left(1 + j\frac{\omega\rho_W C_{PW}}{k_W}\Delta r^2\right), \tag{2.32}$$

$$\Omega_1 = -\frac{\tilde{P}}{k_R}\Delta r^2 \quad ; \quad \Omega_2 = 0 \text{ (no heat generation in the medium)}, \tag{2.33}$$

$$\Delta r = \frac{R}{M-1},\ r_i = (i-1)\Delta r. \tag{2.34}$$

The boundary conditions on nodal terms are:

$$\begin{cases} at\ i = 1;\ r = 0 \rightarrow \tilde{T}_{i-1} = \tilde{T}_0 = \tilde{T}_2 \\ at\ i = N-1;\ r = R_H \rightarrow \tilde{T}_{i-1} = \tilde{T}_N = 0 \end{cases} \tag{2.35}$$

Interfacial condition involves the following equations:

$$k_R\frac{\tilde{T}_M - \tilde{T}_{M-1}}{\Delta r} = k_W\frac{\tilde{T}_{M+1} - \tilde{T}_M}{\Delta r} \quad , \quad \tilde{T}_{M-1} - \left(1 + \frac{k_W}{k_R}\right)\tilde{T}_M + \frac{k_W}{k_R}\tilde{T}_{M+1} = 0 \tag{2.36}$$

The discrete matrix representation for the temperature distribution in the fiber and water is

$$\begin{matrix} \text{i=2} \\ \text{i=3} \\ \\ \\ \\ \text{i=M-1} \\ \\ \\ \text{i=N-1} \end{matrix} \begin{bmatrix} \tilde{T}_2 \\ \tilde{T}_3 \\ \vdots \\ \vdots \\ \vdots \\ \tilde{T}_{M-1} \\ \vdots \\ \vdots \\ \tilde{T}_{N-1} \end{bmatrix} = \begin{bmatrix} \beta_1 & 2 & 0 & \dots & \dots & 0 \\ 1-\Theta & \beta_1 & 1+\Theta & 0 & \dots & 0 \\ 0 & 1-\Theta & \beta_1 & 1+\Theta & \dots & 0 \\ \vdots & \vdots & \ddots & \ddots & \ddots & 0 \\ \vdots & \vdots & 0 & \ddots & \ddots & \vdots \\ 0 & 0 & 0 & 0 & 1-\Theta & \beta_2 \\ \vdots & \vdots & \vdots & \ddots & \ddots & \vdots \\ \vdots & \vdots & \vdots & 1-\Theta & \beta_2 & 1+\Theta \\ 0 & 0 & \dots & 0 & 1-\Theta & \beta_2 \end{bmatrix}^{-1} \begin{bmatrix} \Omega_1 \\ \vdots \\ \vdots \\ \vdots \\ \Omega_1 \\ 0 \\ \vdots \\ \vdots \\ 0 \end{bmatrix} \begin{matrix} \\ \\ \\ \\ \\ \\ \\ \\ \end{matrix} \begin{matrix} \\ \\ \\ \\ \text{Fiber} \\ \\ \\ \text{Water} \\ \\ \end{matrix} \tag{2.37}$$

The complex form of the temperature rise at all nodes ($\tilde{T}_2, \tilde{T}_3 \ldots \tilde{T}_{N-1}$) can be estimated by solving this linear system. The modulus of the average of this temperature rises over all nodes (*1 to M*) gives the average radial temperature rise T_{av} of the sample for certain frequency:

$$T_{av} = \left\| \sum_{1}^{N} \tilde{T}_i \right\| / N \tag{2.38}$$

The overall voltage response at each frequency measured in 3ω method is the modular $V_{3\omega\, rms}$ of the sample and can be expressed as follows:

$$V_{rms} = I_{rms}(R_0 + R_0 \alpha_e T_{av}) = f(\omega) + g(3\omega) \tag{2.39}$$

$$V_{3\omega\, rms} = I_{rms} R_0 \alpha_e T_{av} \tag{2.40}$$

Thus, a frequency dependent $V_{3\omega\, rms}$ was estimated by this 1D numerical model.

4.3 Numerical Finite Element 2D Model

The 3ω method for radial thermal conductivity requires a strong thermal gradient along the radius of the fiber. However, as it will be observed later in this chapter, there is also a presence of axial heat transfer along the fiber. Therefore, a 2D finite element numerical model was developed using Comsol Multiphysics 5.3. An axis-symmetrical model is created as shown in Figure 2.6. The width (*w*) of the surrounding medium was obtained from the 1D model by verifying the distance above which there is no direct influence of the boundaries on the estimation of $V_{3\omega\, rms}$ (section 4.4).

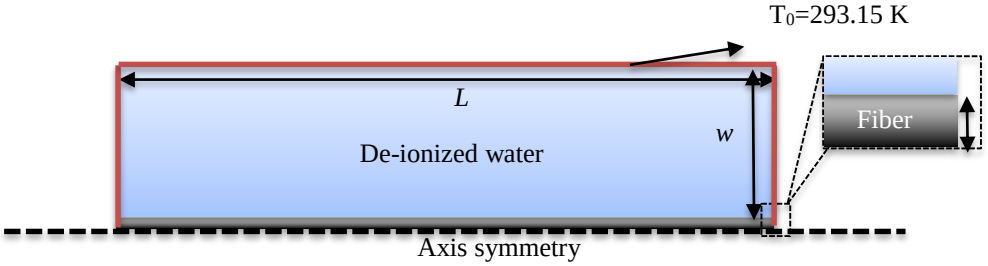


Figure 2.6: Geometry for 2D finite element

The anisotropy in thermal conductivity of the fiber was introduced in the material property by using the longitudinal thermal conductivity determined from the initial 3ω method (chapter 1) and assuming a certain value of radial thermal conductivity. The fiber is also acting as a heat source by the current passing over its length.

Frequency domain perturbation model from Comsol 5.3 was used to calculate the temperature rise depending on different frequencies and the heat source (fiber).

$$j\omega\rho C_p T + \nabla.(-k\nabla T) = P \tag{2.41}$$

where k involves the axial and radial thermal conductivity values as shown in Table 2.1. The initial condition is with imposed room temperature (293.15K) and the external boundaries are also

with imposed temperature of 293.15K. The $V_{3\omega\,rms}$over the sample is calculated by the complex temperature rise in the sample over the wide frequency range of 1-10^5 Hz (Eq. 2.40).

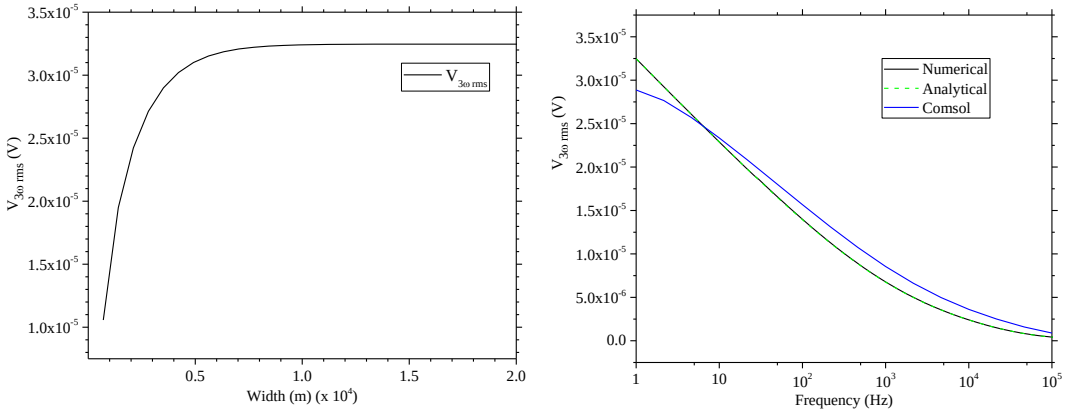
4.4 Comparison between analytical, numerical 1D and numerical 2D

In this section, different models are compared by the value of $V_{3\omega\,rms}$ obtained for the fiber of length 1.5mm and diameter 7µm by passing 1mA current under similar given initial and boundary condition. The input parameters for different models are as shown in Table 2.1.

Thermal Properties	Fiber	Water
ρC_p(MJ $m^{-3}K^{-1}$)	1.3 10^6	4.17e6 [9]
Joule Heat source(Wm^{-3})	3.8 10^{10}	-
1D model k_R($Wm^{-1}K^{-1}$)	k_R =1	0.59 [10]
2D model k($Wm^{-1}K^{-1}$)	$\begin{bmatrix} k_R = 1 & 0 \\ 0 & k_L = 10.4 \end{bmatrix}$	0.59 [10]

Table 2.1: Material Properties of fiber and water for the models

Before doing the comparison, it is necessary to check that the width of the surrounding medium is sufficient to obey the condition of an infinite surrounding. This was verified by comparing $V_{3\omega\,rms}$ for different widths of the surrounding de-ionized water. From Figure 2.7(a), it is determined that the water with a width of more than 0.15 mm is sufficient for the boundaries with no influence on the calculation of $V_{3\omega\,rms}$ of the fiber.



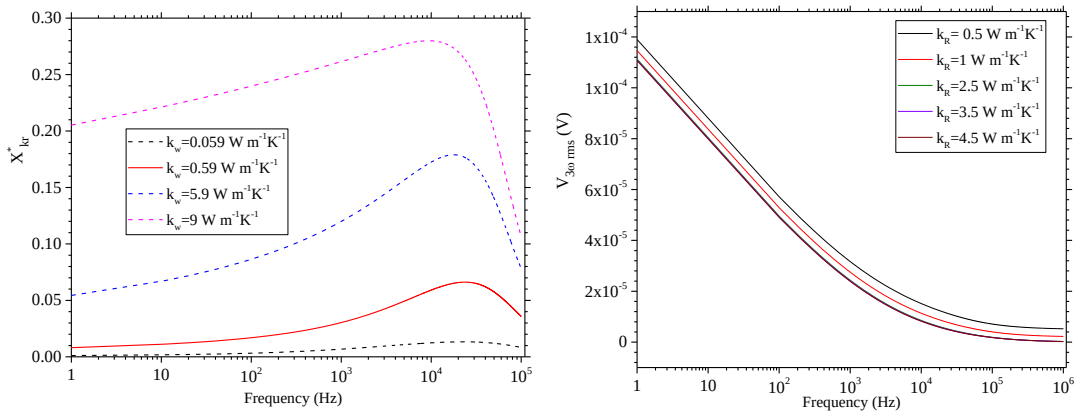
(a) (b)

Figure 2.7: (a) $V_{3\omega\,rms}$ at 1Hz with changing the width of the surrounding medium. (b) $V_{3\omega\,rms}$ Versus frequency for comparing analytical and numerical 1D model with Numerical 2D Finite element model.

Figure 2.7(b) shows the comparison between the 1D analytical and 1D numerical models, along with the 2D finite element based numerical model. It is evident that both 1D models are in good agreement for the overall frequency range, as both models have the same assumption and boundary condition. On the contrary, the finite element 2D model is not exactly following the same trend as the two other models. This is due to the impact of longitudinal thermal conductivity on the computation of the $V_{3\omega\,rms}$. Thus neglecting completely the longitudinal heat flow is still questionable. Further, it is necessary to perform a sensitivity analysis for the radial thermal conductivity in order to find a frequency zone where the estimation of radial thermal conductivity would be feasible.

5. Sensitivity Analysis

This study was performed with the analytical 1D radial thermal model therefore the estimation of the radial thermal conductivity is insensitive to the change in length. From the sensitivity analysis, one seeks for a frequency range where the 3ω measurement provides the best estimation of radial thermal conductivity. This study was done similar to the sensitivity coefficient equation used in section 4 of chapter 1. Figure 2.8(a) shows the sensitivity coefficients for the $V_{3\omega\,rms}$ versus the frequency. It is observed that the sensitivity is better at higher frequency range (10^3 Hz – 10^5 Hz), but the overall maximum value of sensitivity coefficients is rather small (<0.07 if we use water as surrounding medium where k_w =0.59 $Wm^{-1}K^{-1}$). It was also seen that increasing the thermal conductivity (k_w) of the infinite medium around the fiber improved significantly the sensitivity coefficients (Figure 2.8(a)). Indeed, if we increase k_w from 0.059 (insulation material) to 0.59 $Wm^{-1}K^{-1}$ (water), the sensitivity X^*_{kr} increases by 6 times which justifies the use of water. Further increase of k_w to 5.9 $Wm^{-1}K^{-1}$ would have been very interesting with respectively a 2.5 and 4 times X^*_{kr} increase with respect to the case of water. However, practically it is difficult to have a material with such a high conductivity that would be easy to implement around the fibers. Indeed, the sensitivity coefficients stay very small compared to the ones of the axial thermal conductivity parameter and especially at low frequency. For example at 10 Hz, the reduced sensitivity coefficients for k_R and k_L are respectively around 0.06 and 0.9 (with L=1.5mm). Additionally Figure 2.8(b) shows the value of $V_{3\omega\,rms}$ for different radial thermal conductivity values. It can be checked to be weakly sensitive to the change in radial thermal conductivity of the fiber especially for value above 1 W $m^{-1}K^{-1}$. Thus the uncertainty analysis should provide a much larger uncertainty along with the confidence band for k_R estimation than k_L.



(a) (b)

Figure 2.8: (a) Sensitivity analysis of the $V_{3\omega\,rms}$voltage to the radial thermal conductivity with varying k_W (b) $V_{3\omega\,rms}$ with frequency for different k_R, analysis performed with the analytical 1D radial model $k_W = 0.59$ W m^{-1}K^{-1}.

6. Experimental test for radial thermal conductivity

6.1 Fitting with 1D analytical model

Despite the limitation of the sensitivity coefficient, test was performed with a carbon fiber FT300B for the estimation of the radial thermal conductivity by the 3ω method. Figure 2.9 shows the experimental $V_{3\omega\,rms}$ with a frequency range of 1-2500 Hz (applied limitation due to lock in amplifier) by passing a current of 1mA over a sample of length 1.7mm. The experimental data was fitted with the 1D finite analytical model for a frequency range of 1-2500 Hz as shown in Figure 2.9. It can be seen that the fitting is rather incoherent with the experimental data. A fitting for lower frequency bound of 1-100 Hz was also tested, but no significant change in the quality of the fitting was observed. Moreover, the obtained $k_R(0.5-9)$ were with larger confidence bound of the fitting results. One possible reason for the discrepancy between the experimental result and 1D radial model is the presence of axial heat transfer and too low sensitivity. Its effect is suspected to modify significantly the shape of the $V_{3\omega\,rms}$ evolution. Therefore, in the following section, the 2D heat transfer model using a finite element model will be used.

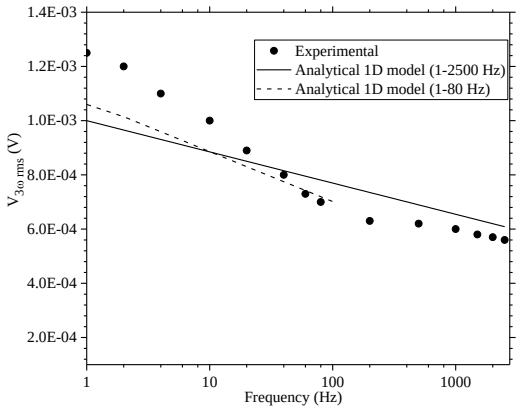


Figure 2.9: Experimental results for FT300B carbon fiber with diameter of 7.3 µm

6.2 Fitting with 2D finite element model

A fitting to experimental data by the 2D finite element model is presented in Figure 2.10(a). It can be observed that the fitting is notably improved for a frequency less than 100 Hz. The axial thermal conductivity was imposed from the results obtained in Chapter 1. To estimate the value of radial thermal conductivity, an error analysis was performed by varying the radial thermal conductivity from 0.1 to 4 $Wm^{-1}K^{-1}$ and in the frequency window 1-100Hz (Figure 2.10(b)). The model agreement is evaluated through the root mean square error (RMSE):

$$RMSE = \sqrt{\frac{\sum_{i=1}^{N}(V_i - V_i^{model})^2}{N}} \tag{2.41}$$

where V_i is the $V_{3\omega\,rms}$ during experiment at different frequency points i=1,2 .. N, V_i^{model} is the $V_{3\omega\,rms}$ by the 2D model. From Figure 2.10(b) it can be seen that the RMSE is rather flat for a certain range of thermal conductivity (0.7-1.1 $Wm^{-1}K^{-1}$) where a minimum can be observed. Arguably, the exact solution for radial thermal conductivity lies in this range. As visible on the detailed view of Figure 2.10(c) which enables to precise the very minimum of the RMSE function, the radial thermal conductivity for the fiber FT300B can be estimated to be 0.8 $Wm^{-1}K^{-1}$. Additionally, the uncertainty sources in the measurement comes also from various input parameters (5.7%) as discussed in the section 6 of previous chapter, for longitudinal thermal conductivity. The uncertainty in the $V_{3\omega\,rms}$ is approximately 15.9% leading to the overall uncertainty in the radial thermal conductivity measurement for carbon fiber as 23.6%. Therefore, the radial thermal conductivity value for FT300B is 0.8 ± 0.19 $Wm^{-1}K^{-1}$.

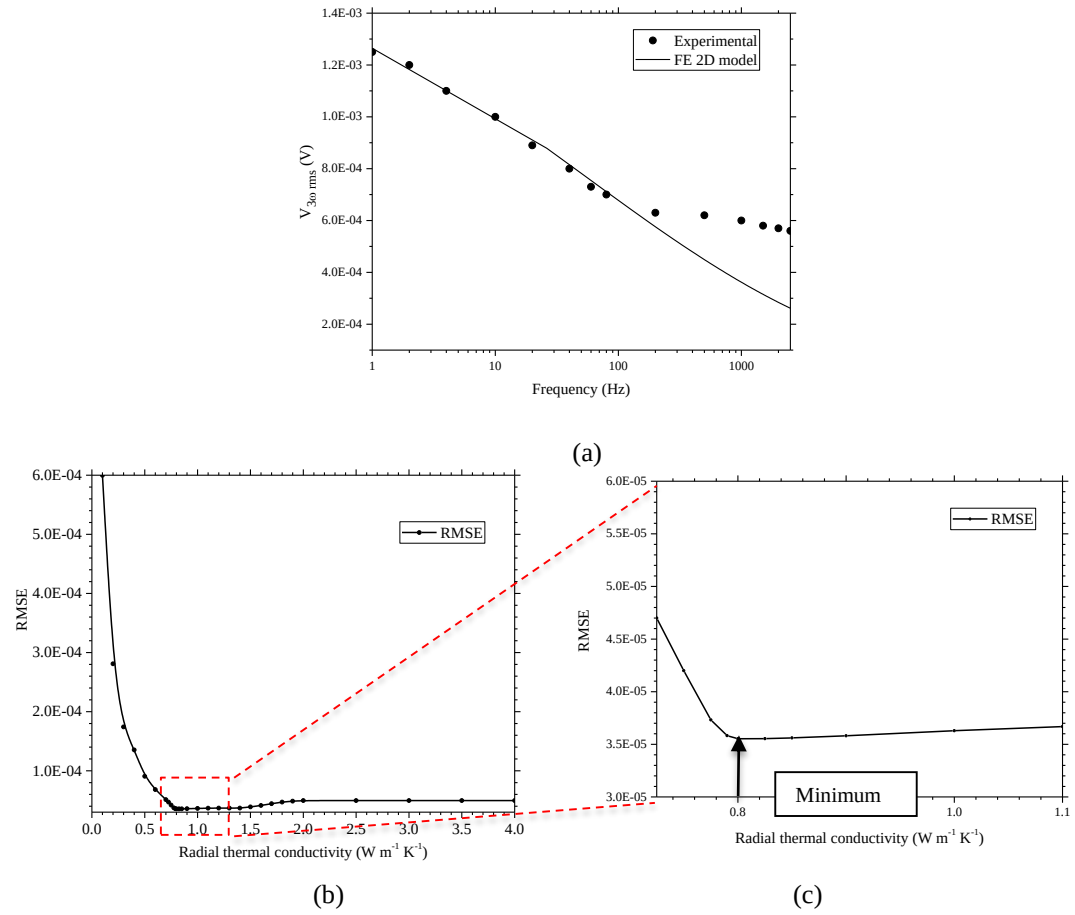


Figure 2.10: (a) Measurements for FT300B carbon fiber with diameter of 7.3 µm and length 1.38 mm (b) evolution of RMSE between experimental and numerical model for different k_R at frequency window of 1-100 Hz (c) Zoomed region of RMSE for k_R between 0.7 – 1.1 Wm^{-1}K^{-1}

7. Partial Conclusion

In this chapter, the application of the 3ω method on estimating the radial thermal conductivity of single carbon fiber was discussed. A detailed derivation of the analytical model along with 1D numerical model was shown. A further 2D finite element model was developed to verify the effect of the longitudinal heat transfer. It was observed that the longitudinal heat flow cannot be neglected at all as it ultimately affects the value of $V_{3\omega\,rms}$. A sensitivity analysis was performed for the 3ω method on the basis of a purely radial transfer model and it was seen that the sensitivity of $V_{3\omega\,rms}$for the radial thermal conductivity was quite low (<0.06). This intrinsically makes the estimation of radial thermal conductivity rather difficult and the uncertainty on results rather important. From the experiments on FT300B, it was observed that the 3ω method was only capable of estimating the radial thermal conductivity with an uncertainty of 23.6% and bigger confidence band. Apart from that, the fitting of the experimental and finite element model was also not coherent beyond 100Hz. The deviation could be because of the microstructure non-uniformity along the diameter (fiber not perfectly cylindrical). Yet, the exact reason of this deviation needs further investigation.

From this chapter, it was concluded using the 3ω method the value of radial thermal conductivity can be predicted with large uncertainty, at least in the current configuration and the tested frequency range. The difficulty comes from the low sensitivity coefficient. Nevertheless, this first study about the radial heat transfer is very promising and would place the 3w method as good candidate to measure both the longitudinal and radial conductivity on two similar and rather simple devices. The lack of research towards the radial thermal conductivity, makes this initial contribution of 3ω method with high importance. It was also observed that a higher thermal conductivity of the surrounding medium would increase significantly the sensitivity coefficient. A perspective would be for example using a phase change material with higher thermal conductivity as an alternative to water.

References

[1] Liang J 2014 *Experimental measurement and modeling of thermal conductivities of carbon fibers and their composites modified with carbon nanofibers* (University of Oklahoma)

[2] Villière M, Lecointe D, Sobotka V, Boyard N and Delaunay D 2013 Experimental determination and modeling of thermal conductivity tensor of carbon/epoxy composite *Compos. Part A Appl. Sci. Manuf.* **46** 60–8

[3] Donaldson A B and Taylor R E 1975 Thermal diffusivity measurement by a radial heat flow method *J. Appl. Phys.* **46** 4584–9

[4] Degiovanni A, Batsale J . and Maillet D 1996 Mesure de la diffusivité longitudinale de matériaux anisotropes *Rev. Générale Therm.* **35** 141–7

[5] Tian T and Cole K D 2012 Anisotropic thermal conductivity measurement of carbon-fiber/epoxy composite materials *Int. J. Heat Mass Transf.* **55** 6530–7

[6] Huang H S, Ganguli S and Roy A K 2014 Prediction of the transverse thermal conductivity of pitch-based carbon fibers *J. Compos. Mater.* **48** 1383–90

[7] ASTM C177-19 2019 Standard Test Method for Steady-State Heat Flux Measurements and Thermal Transmission Properties by Means of the Guarded-Hot-Plate Apparatus *ASTM Int. West Conshohocken, PA*

[8] Wang R, Zobeiri H, Lin H, Qu W, Bai X, Deng C and Wang X 2019 Anisotropic thermal conductivities and structure in lignin-based microscale carbon fibers *Carbon N. Y.* **147** 58–69

[9] Joe Khachan 2018 *Thermal Properties of Matter* (Morgan & Claypool Publishers)

[10] Ramires M L V, Nieto Castro C A, Nagasaka Y, Nagashima A, Assael M J and Wakeham W A 1995 Standard Reference Data for the Thermal Conductivity of Water *J. Phys. Chem. Ref. Data* **24** 1377–81

Chapter 3

Thermal modeling of fibrous composite for estimating effective thermal conductivity tensor

1. Introduction **63**
2. Homogenization **64**
2.1 Mesoscale/Macroscale 64
2.2 Representative elementary volume (REV) and scale separation 64
3. Theoretical Models **66**
3.1 Modeling based on real microstructures 67
3.2 Basic Concept of Homogenization and asymptotic expansions 69
3.3 Effective Thermal conductivity estimation for imposed boundary conditions 71
4. Development of Framework for Effective conductivity tensor calculation **72**
4.1 Geometrical modeling 72
4.2 Boundary conditions 74
5. Results on Square Packed CFRC **76**
5.1 Influence of Length on different Boundary conditions 76
5.2 Representative elementary volume of uniform square cell 79
5.3 Influence of Volume fraction 81
6. Results on Random distributed fibers in CFRC **82**
6.1 Influence of Randomization and Clustering 82
6.2 REV and homogenization in tapes 83
7. Partial Conclusion **86**
References **87**

1. Introduction

Composite materials have anisotropic properties due to their complex microstructure. Therefore, perfect characterization of each parameter, thermal/mechanical/chemical, is necessary to understand the overall behavior and impact of the composite during various applications. The multiple scales of heterogeneities, from individual fibers, to yarns, eventually to the textile period and then plies imply a rich and complex multiscale analysis of the physical behavior of a composite. Figure 3.1 shows the schematic scaling of composite from the scale of cm to µm. A huge amount of research articles deal with the multiscale analysis of mechanical properties of composite materials [1–4]. However, the multiscale thermal analysis[5–11][5–11][5–11] is an area that requires more vast research as the overall strength of the composite is highly correlated with the thermal history. The two previous chapters dealt with the microscale characterization of single fibers by estimating thermal conductivity. The present chapter now focuses on the numerical analysis of the thermal conductivity at larger scale, using data gained experimentally at the micro-scale.

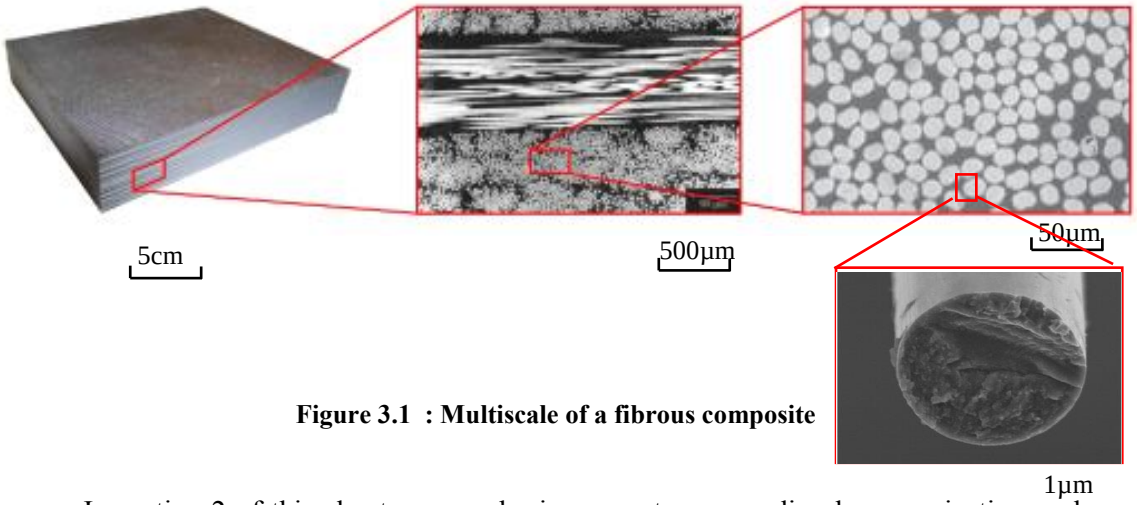


Figure 3.1 : Multiscale of a fibrous composite

In section 2 of this chapter, some basic concepts surrounding homogenization such as meso/macroscale division, representative elementary volume are presented, as well as different existing models of the literature for the estimation of the effective thermal conductivity (section 3). In this chapter, meshes for CFRC with different types of arrangement of fibers, starting from square packed, random or real are presented (section 4). Real meshes in correspondence to industrial tapes such as those provided by Solvay and Suprem are analyzed. In later sections, different factors influencing the effective thermal conductivity tensor estimation such as length of the mesh, contrast in properties, and type of boundary conditions are also discussed (section 5). Moreover, the homogenization in real tapes used in automated tape laying or automated fiber placement is also discussed (section 6).

2. Homogenization

2.1 Mesoscale/Macroscale

The heterogeneities present in fibrous composite such as the characteristic lengths (i.e. the diameter and length of the constituents) depends directly on the fibers considered. Generally remain of the order of four or hundred microns (carbon, glass, polymer, wood, etc ...), which is way below the macroscopic scale[12] At this scale, it is very difficult to simulate a physical process over an extended domain while keeping a sufficiently fine mesh to take into account all local heterogeneities. Therefore, the material effective properties are estimated taking into account the local heterogeneities at a mediatory scale that can describe the behavior at the macroscopic scale as the one of a homogeneous continuous medium.

As we are interested mainly in organic matrix fibrous composites, the matrix conductivity is generally low in our problems, and in any case lower, or much lower than the fiber one. In this context, in the longitudinal direction, it is commonly admitted that fibers largely dominate the heat transfer, whereas in the transversal direction, fibers, matrix and fiber/matrix interface or fiber/fiber contacts also come into play at a similar range. The effective properties also depend on the conductivity tensor of the fiber, on fiber orientation and fiber volume fraction, fiber spatial distribution and many more local factors. Deterministic methods such as averaging and homogenization methods[13] are generally used for the estimation of the effective thermal conductivity.

2.2 Representative elementary volume (REV) and scale separation

It is important to consider a larger volume known as representative elementary volume (REV), demonstrative of each small factors that determine the value of the effective property (Figure 3.2). Beyond this scale, the effective properties remain constant and can be implemented to depict the thermal behavior for the macroscale composite. Solving directly at the macro scale with classical numerical techniques such as FEM, FVM and FDM would require a bigger mesh to encounter all heterogeneities (proportional to the number of local factors) and thus with a high computational cost. However, with REV, an intermediary region could be found that can deal with the local factors impact on the macro scale[13][10].

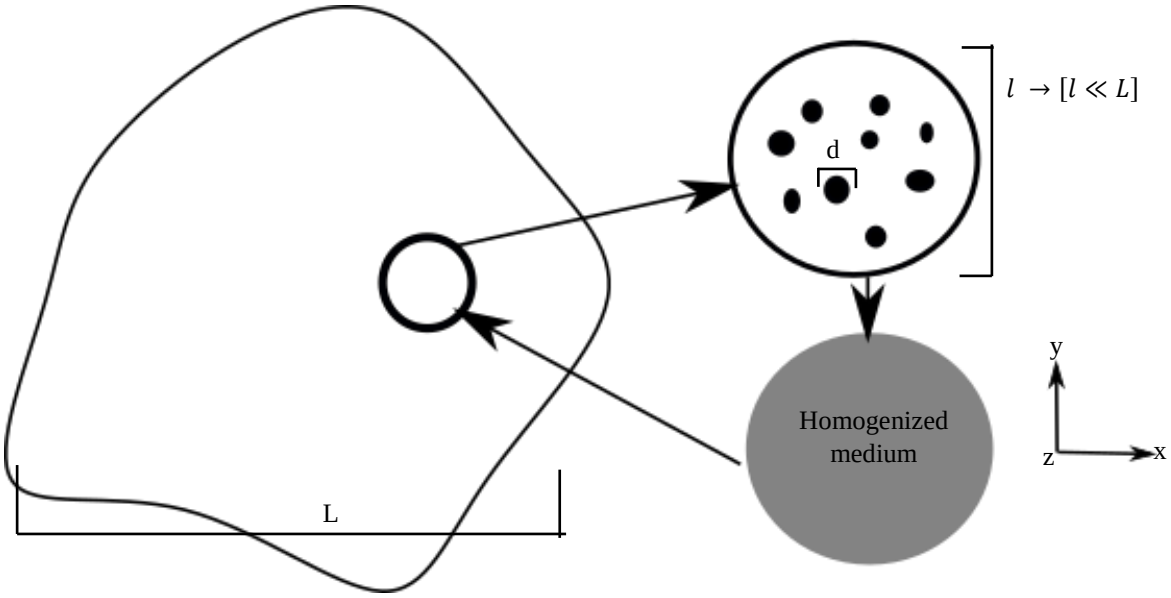


Figure 3.2: Schematic representation of homogenization approach[14] d=diameter of the fiber, l= length of REV, L= length of macroscale

In the thesis of Hadi Moussady[15], he discussed various definitions of REV that has been discussed through literature and mentioned below:

- Hill[16]: The RVE refers to "a sample that a) is structurally entirely typical of the whole mixture on average, and b) contains a sufficient number of inclusions for the apparent overall moduli to be effectively independent of the surface values of traction and displacement, so long as these values are macroscopically uniform." While a) is a condition to the microstructure morphology, b) expresses the RVE independency of the applied boundary conditions.
- Drugan and Willis[17]: The RVE is "the smallest material volume element of the composite for which the usual spatially constant "overall modulus" macroscopic constitutive representation is a sufficiently accurate model to represent a mean constitutive response."
- Gusev[18]: The RVE is a material volume that computes the same effective properties as the bulk material.
- Jiang[19]: The REV is an "infinite length scale limit, relative to the microscale in which the material appears uniform and the continuum concept may be applied"
- Ostoja-Starzewski[20]: The RVE is defined by three conditions: "(i) statistical homogeneity (stationarity) and ergodicity; (ii) Hill condition leading to admissible boundary conditions; (iii) variational principle."

From the above definitions, the REV can be obtained either through physical, microstructural or morphological behavior. However for homogenization, the REV is frequently obtained by the constant effective properties reached after certain size.

It is therefore interesting to get a description of the heterogeneous medium with an equivalent homogeneous model containing all the heterogeneities of macroscale. This then

implies a certain scale separation between the microscopic heterogeneities, size l and the macroscopic size L. This can be achieved by taking into account:

$$\varepsilon = \frac{l}{L} \ll 1 \tag{3.1}$$

Depending on the scale separation, there can be two non-dimensional space variables defining the behavior, $x^* = X/L$ and $y^* = X/l$ where X is the real Cartesian coordinate at macroscale, x^* is then considered as the macroscopic variable, y^* is then considered as the macroscopic variable. Thus in case of heat transfer problem, the temperature variable is a function of these two non-dimensional space variables with $T = T(x^*, y^*)$.

3. Theoretical Models and Homogenization

The techniques for calculation of the effective properties for a heterogeneous composite can be grouped into two parts depending on the arrangement of the fibers in the matrix[14].

- Simplified model- Applicable to ideal heterogeneous composite where REV is represented by a periodic pattern.
- Real microstructural model- Dispersion or non-uniform distribution in the constituent position are difficult to be taken into account in a single model. Effective properties are directly numerically calculated from the microstructure by using approaches like unit cell method or embedded cell method.

The simplest approach towards effective thermal conductivity estimation comes through rules of mixture. Modeling through the assumption of uniform temperature gradient in the considered direction.

$$K_{axial} = v_f K_f + (1 - v_f) K_m \tag{3.2}$$

where v_f is the volume fraction of the fiber, K_f longitudinal conductivity of fiber and K_m is the thermal conductivity of matrix. The hypothesis for transversal thermal conductivity ($K_{\|}$) estimation involves the concept that the heat flux is constant.

$$K_{transversal} = \frac{K_m K_f}{K_m v_f + (1 - v_f) K_f} \tag{3.3}$$

Voigt-Reuss bounds are also popularly known as mixture rule model where the phases are considered either in series (Reuss) or parallel (Voigt) through the thermal paths. These two models then lead to a framework of the effective conductivity tensor for heterogeneous material. These models are applicable to any type of inclusion starting from spherical, or cylindrical[21]. However, slightly sophisticated approach for effective property estimation is the effective mean field model. In this case, the heterogeneous materials are considered to be homogenized. In the following section, brief descriptions of some models are presented[22].

Maxwell model[14]: In the work of Maxwell, effective thermal conductivity of a dilute dispersion of spherical particles in a continuous matrix was measured. Later, this model was improved depending on the type of inclusions. No thermal interaction between the filler and the matrix was

considered, however this was modified in one article by Hasselman [23] where he considered thermal resistance between the inclusion and medium. The expression for effective thermal conductivity is given by

$$K_{Maxwell} = K_m \frac{v_f(p-1)+p+1}{v_f(1-p)+p+1} \rightarrow \mathrm{p} = \frac{K_f}{K_m} \tag{3.4}$$

Rayleigh Model[24][25]: This model was developed for cubic arrays of spherical and cylindrical inclusions. The effective transversal thermal conductivity for cylindrical particles representation can be written as:

$$K_{Rayleigh} = K_m \left[1 + \frac{2v_f}{\frac{K_m+K_f}{K_m-K_f} - v_f + \frac{K_m-K_f}{K_m+K_f}\left(0.3058v_f^4 + 0.0134v_f^8\right)} \right] \tag{3.5}$$

Similarly, there are other models of effective conductivity in the literature such as Eshelby[26], Mori-Tanaka[27], Ponte Castaneda [28], Weng, Benveniste models[29] [14]. They use different assumptions to simplify the approach towards heterogeneities. The major disadvantage of these models comes from the lack of information regarding the composite microstructure and sometimes the strong assumptions that can induce a high deviation from reality.

However, the bound approach accepts the disadvantage of theoretical modeling and gives a bound, upper and lower limit of the effective property rather than giving a single value. Two classical models for bound predictions are Voigt-Reuss and Hashin-Shtrikman. Compared to the Voigt and Reuss bounds, Hashin and Shtrikman (HS) defined a tighter bound. The importance of HS bound comes from the fact that this variational principle based bound is applicable for the inhomogeneous composite. In the case of a two-phase composite in which reinforcement is more conductive than the matrix, the Hashin and Shtrikman lower and upper bounds are[30]

$$K_{HS-} = K_m + v_f \left[\frac{1}{(K_f - K_m)} + \frac{1-v_f}{2K_m} \right]^{-1} \tag{3.6}$$

$$K_{HS+} = K_f + (1-v_f) \left[\frac{1}{(K_m - K_f)} + \frac{v_f}{2K_f} \right]^{-1} \tag{3.7}$$

Derivations of the HS bounds have been improved and revised by many authors since they were originally developed. It should be noted that the Hashin–Shtrikman bounds, demonstrate divergence and become almost out of practical use for the densely packed, high contrast of thermal properties[30]. Although these bounds can give an expected range of the effective thermal property for certain volume fraction of the composite, exact estimation would need a numerical model to take into account the microstructural deformities.

3.1 Modeling based on real microstructures

The simplified theoretical models are easy to implement but the complexity in real geometries make direct employment of these models questionable. However, the accessibility of fast computers has allowed the development of advanced computational methods able to realize

calculations on more complete microstructures, thus reliving the standard assumptions on the statistical distribution of fibers and on local interactions. The main advantage of these methods is their flexibility since they can be applied to any kind of arrangement, and especially on real composite microstructures.

Numerically the effective thermal conductivity can be determined by finite difference, boundary elements, finite elements, finite volume and many other methods[31]. With a finite difference approach, the primary disadvantage lies in the precision of the geometrical description of particles. Despite the presence of other numerical techniques present such as finite volume or boundary element, however, in this thesis the focus is using finite element method for effective thermal conductivity estimation.

Generally, there are two approaches in the literature for this estimation, namely the unit cell approach and the embedded cell approach that are briefly described hereunder.

- Unit cell approach- It is a simple and common approach for estimation of effective properties. In the literature, it was used for simple 2D to complex multiphase models for different types of materials. Initially, for CFRC, the simplest way to implement the unit cell approach is for identical fibers surrounded by a matrix layer in periodical distribution. It ignores the effect of variations in the inclusion type. However, many researchers have worked on the application of unit cell approach for multiple inclusions[32], statistical inclusion distribution[33], damaged matrix[34] and etc. Even if the approach is too simple to estimate accurately effective properties of real composites, it appears to be very efficient in the analysis of the effects of inclusions arrangement, inclusions volume fraction, shape or contrast. The basic concept of unit cell approach is to impose opposite surface of the sample with temperature gradient. As shown in Figure 3.3, the surface A is imposed with temperature 1K and the surface B is imposed with temperature 2K. Keeping the remaining surfaces at adiabatic condition, the heat current is from high temperature surface to low temperature as shown in Figure 3.3. In a steady state situation, the inward flux through surface A equals the outward flux through surface B. The effective thermal conductivity in the considered direction is the ratio of the flux over the length of the sample and the temperature difference between the surfaces A and B (~1K in this case).

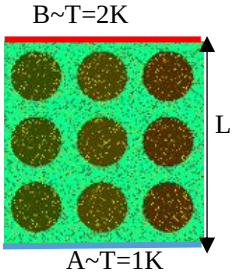


Figure 3.3 : Unit cell approach on small CFRC

Generally, a unit thermal gradient is be applied along different directions in order to estimate the complete effective thermal conductivity tensor. This of course assumes that the unit cell was exactly chosen in the principal axes of the conductivity tensor, which is not so obvious for random microstructures. The main advantage of the unit cell approach is the requirement of little computational efforts for complex microstructure. However,

over simplification can lead to certain discrepancies in the results such as using these techniques for large deformations, complex microstructures and/or non-linear history dependent constitutive behavior[22].

- Embedded cell approach- It consists of integrating the cell to be studied in a homogenized volume whose properties are known in advance (or are the ones that one seeks) and to impose a mesh on the edges of the enveloping volume[14] (Figure 3.4). The core region that contains the discrete phase arrangement of the composite material is embedded within some outer region that stands for the bulk composite. The properties of the equivalent material are determined by any simple analytical model. The boundary conditions are then applied to this homogeneous material. It can be described by different ways. A first common approach consists in using the homogenized response of the core, e.g. determining it with a self-consistent manner from the behavior of the core[35][36]. A second way is based on the use of macroscopic constitutive laws, e.g. Knight[37] used semi-empirical Halpin and Tsai model so as to determine the embedding region properties. The embedding allows for the effect of the rest of the material and the influence of the interaction of other inclusions with a given inclusion on the behavior of the cell. The advantage of this approach comes from its capability to handle the microstructural complexity, however, the computational cost is higher.

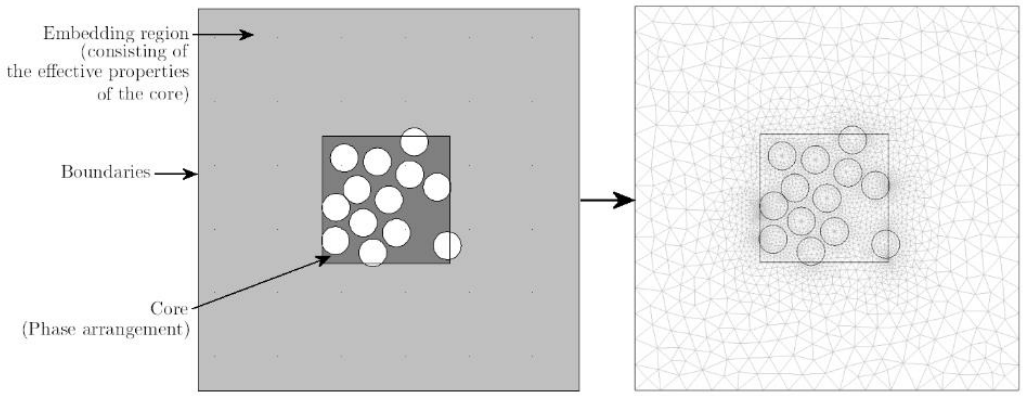


Figure 3.4 : Schematic diagram of embedded cell approach[38]

3.2 Basic concept of Homogenization and Asymptotic expansions

As discussed in the previous sections, various approaches exist to identify effective properties of a heterogeneous material. The non-homogeneity of the composites at different scales can be homogenized, depending strongly on the internal spatial distribution, the size and the properties of the material components and their respective interfaces. In a widely simpler case study used in this thesis, the objective was to deal with the unidirectional fibrous composite for estimating the effective thermal property. When the properties of the resin and fibers are known or determined by experimental approach, it is possible to define the equivalent thermal properties the composite material. This can be achieved by solving the asymptotic expansion, described in details in this section. These methods are based on a fundamental assumption of periodicity of the middle structure, which is sometimes the case in composite materials, or in any event within

idealized composite structures. We then consider a heterogeneous material whose properties are continuous by piece, alternating between those of the individual components. Therefore, the properties reproduce by periodic translation on a microscopic scale. The REV should generally contain a sufficient number of heterogeneities while having a small size to macroscopic dimensions studied. In the case of a periodic medium, the REV is reduced to the periodic cell. The size of the heterogeneities is then the same as the size of the REV.

In the thesis of M. Peron[39], a detailed description of various stages of homogenization process in solving the transient heat transfer equation was presented. Generally, the heat transfer by conduction is solved in a domain Ω consisting of two phases, Ω_f and Ω_m, each considered homogeneous and isotropic. The microstructure of the domain Ω is periodic and the periodic cell P is described. In each phase the following heat transfer equation is solved with an assumption of continuity of temperature at the interface of fiber and matrix:

$$\rho C_p \frac{\partial}{\partial t} T(x,y,z,t) - \nabla.\left(\boldsymbol{K}\nabla T(x,y,z,t)\right) = 0 \tag{3.8}$$

Following the method described in the thesis and adopting the macroscopic point of view, we define the various quantities of the problem by using characteristic quantities:

$$\nabla^* \bullet = L\nabla \bullet, t^* = \frac{t}{t_c}, C^* = \rho C_p / C_c, T^* = \frac{T}{\Delta T_c}, \boldsymbol{K}^* = \boldsymbol{K}/\boldsymbol{K_c} \tag{3.9}$$

where the quantities followed by an asterisk are the dimensionless quantities and those denoted by the index "c" are the characteristic quantities. By rearranging it, the previous system becomes.

$$C^*\dot{T}^* - F_c\, \nabla^* \boldsymbol{K}^* \nabla^* T^* = 0 \rightarrow F_c = \boldsymbol{K_c} t_c / C_c L^2 \tag{3.10}$$

Because of the separation of scales, it sets up two dimensionless variables space, x^* and y^*, as discussed previously. The differential operator is converted to

$$\boldsymbol{\nabla}^* = \boldsymbol{\nabla}_{\mathbf{x}^*} + \frac{\partial \mathbf{y}^*}{\partial \mathbf{x}^*}\boldsymbol{\nabla}_{\mathbf{y}^*} = \boldsymbol{\nabla}_{\mathbf{x}^*} + \frac{1}{\varepsilon}\boldsymbol{\nabla}_{\mathbf{y}^*} \tag{3.11}$$

The temperature field in the form of an asymptotic expansion in powers of ε.

$$T^*(\mathbf{X}^*, t^*) = \varepsilon^0 T^{(0)*}(\mathbf{x}^*, \mathbf{y}^*, t^*) + \varepsilon^1 T^{(1)*}(\mathbf{x}^*, \mathbf{y}^*, t^*) + \varepsilon^2 T^{(2)*}(\mathbf{x}^*, \mathbf{y}^*, t^*) + \ldots \tag{3.12}$$

Implementing the above two equation in equation, we get

$$\begin{aligned}
&C^*\left(\dot{T}^{(0)*} + \varepsilon^1 \dot{T}^{(1)*} + \varepsilon^2 \dot{T}^{(2)*} + \ldots\right) \\
&= F_c\Big(\boldsymbol{\nabla}_{\mathbf{x}^*} K^* \boldsymbol{\nabla}_{\mathbf{x}^*} T^{(0)*} + \varepsilon^{-1}\boldsymbol{\nabla}_{\mathbf{y}^*} K^* \boldsymbol{\nabla}_{\mathbf{x}^*} T^{(0)*} + \varepsilon^{-1}\boldsymbol{\nabla}_{\mathbf{x}^*} K^* \boldsymbol{\nabla}_{\mathbf{y}^*} T^{(0)*} \\
&+ \varepsilon^{-2}\boldsymbol{\nabla}_{\mathbf{y}^*} K^* \boldsymbol{\nabla}_{\mathbf{y}^*} T^{(0)*} + \varepsilon \boldsymbol{\nabla}_{\mathbf{x}^*} K^* \boldsymbol{\nabla}_{\mathbf{x}^*} T^{(1)*} + \boldsymbol{\nabla}_{\mathbf{y}^*} K^* \boldsymbol{\nabla}_{\mathbf{x}^*} T^{(1)*} \\
&+ \boldsymbol{\nabla}_{\mathbf{x}^*} K^* \boldsymbol{\nabla}_{\mathbf{y}^*} T^{(1)*} + \varepsilon^{-1}\boldsymbol{\nabla}_{\mathbf{y}^*} K^* \boldsymbol{\nabla}_{\mathbf{y}^*} T^{(1)*} + \varepsilon^2\, \boldsymbol{\nabla}_{\mathbf{x}^*} K^* \boldsymbol{\nabla}_{\mathbf{x}^*} T^{(2)*} \\
&+ \varepsilon\, \boldsymbol{\nabla}_{\mathbf{y}^*} K^* \boldsymbol{\nabla}_{\mathbf{x}^*} T^{(2)*} + \varepsilon \boldsymbol{\nabla}_{\mathbf{x}^*} K^* \boldsymbol{\nabla}_{\mathbf{y}^*} T^{(2)*} + \boldsymbol{\nabla}_{\mathbf{y}^*} K^* \boldsymbol{\nabla}_{\mathbf{y}^*} T^{(2)*} \\
&+ \ldots\Big)
\end{aligned} \tag{3.13}$$

This equality is a continuation in power ε which, must be true regardless of the scale separation ε, identifying the relationship with different levels of ε. In the thesis of M. Peron, depending on the power ε, the asymptotic form of heat transfer equation was simplified. The order of Fourier number also played an important role in finding the effective properties. It was concluded that the homogenizability of conductive heat transfer problem in terms of separation of scales and the number of Fourier number. For Fourier number of order ε^{-1}, the problem is homogenisable and the capacitive term is negligible to the order 0. This enables the estimation of effective thermal conductivity as described in the upcoming section. The interest of the method of asymptotic development is from a local description of the problem to the microscopic scale components, it is possible to determine if a behavior equivalent homogeneous on a macroscopic scale is possible.

3.3 Effective Thermal conductivity estimation for imposed boundary conditions

The prediction of the effective thermal conductivity tensor of CFRC for distribution of fiber in a matrix in form of square packed to real tapes is possible by application of different boundary conditions to the heat transfer problem. In the principal axes of heat conduction and for a transversely isotropic material such as UD composites, the thermal conductivity tensor can be represented in the following matrix form

$$\boldsymbol{K} = \begin{bmatrix} K_{transversal} & 0 & 0 \\ 0 & K_{transversal} & 0 \\ 0 & 0 & K_{axial} \end{bmatrix} \tag{3.14}$$

In general, the heat transfer equation solved for effective conductivity tensor is following.

$$\nabla_y \boldsymbol{K} \nabla_y T = S \tag{3.15}$$

where S is the source term. Depending on the type of boundary condition, the equation is transformed as follows. In case of periodic boundary condition with homogenizable asymptotic equation (ε^{-1}):

$$S = -\nabla_y \boldsymbol{K} \nabla_x T^{(0)} \rightarrow \nabla_y \boldsymbol{K} \nabla_y T = -\nabla_y \boldsymbol{K} \nabla_x T^{(0)} \tag{3.16}$$

The PDE was solved for T with given macroscopic unit gradients $\nabla_x T^{(0)}$ by FEM with FreeFem++. The effective thermal conductivity tensor ($\boldsymbol{K_{eff}}$), in periodic condition, is obtained by solving the following equation:

$$\boldsymbol{K_{eff}} = \frac{1}{P} \int \boldsymbol{K} \left(\boldsymbol{I} + \nabla_y T \right) \tag{3.17}$$

In case of classical boundary condition such as mixed, Dirichlet or Neumann:

$$S = 0 \rightarrow \nabla_y \boldsymbol{K} \nabla_y T = 0 \tag{3.18}$$

A detailed description of application of each boundary condition cases are present in section 4.2. The PDE was solved for T under different boundary condition by FEM with FreeFem++. With the data of T over the mesh, the flux in/ flux out is calculated and then the effective conductivity is estimated.

$$\langle \varphi \rangle = \langle \boldsymbol{K} \nabla_y T \rangle / L \longrightarrow \boldsymbol{K_{eff}} = \frac{\langle \varphi \rangle L}{\Delta T} \tag{3.19}$$

where ΔT is the difference in temperature. Overall with homogenization, the primary objective of existence of equivalent continuum for the heat transfer problem needs to be fulfilled. Secondarily, at the scale of REV, the effective properties of the homogenized medium needs to be determined. Thus, a spatially dependent equation at heterogeneous scale to a homogenized spatially independent equation is represented. In this thesis, the effective thermal conductivity tensor and presence of REV under different boundary conditions are estimated.

4. Development of Framework for Effective conductivity tensor calculation

4.1 Geometrical modeling

To fully calculate the anisotropic conductivity tensor for any situation, a 3D finite element approach was adopted. The first step to generate a 3D mesh from a given microstructure, real or generated. In this chapter, three types of mesh were generated depending on the distribution of the fibers in the matrix, i.e. uniform square cell, random distribution and clustered distributions. Moreover, meshes in resemblance to the real microstructure were also generated (detailed in chapter 4). The geometries and meshes were generated using GMSH, a free finite element meshing tool.

- Uniform square cell- Hypothetical uniformly placed fibers in a matrix were generated for different volume fraction starting from approximately 0.2 to 0.6 fiber volume fraction. At each volume fraction, multiple meshes with different number of fibers were generated such as for sample window 2 to 10 (Figure 3.5).

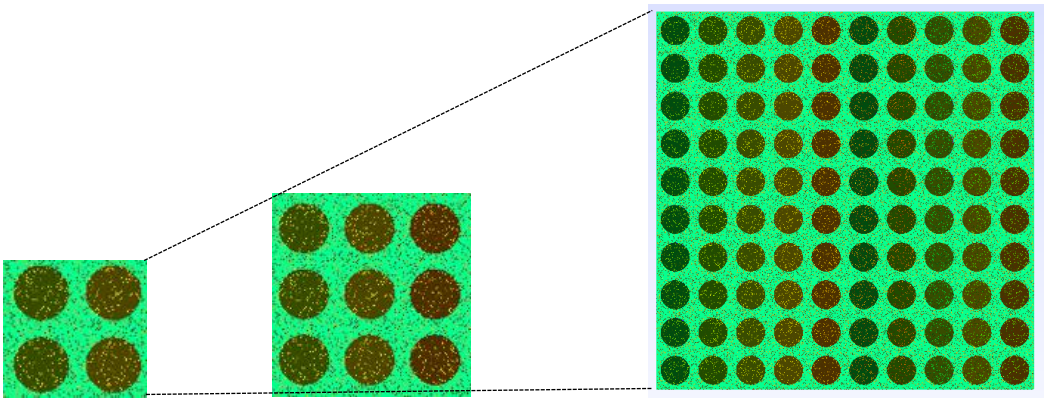


Figure 3.5 : Evolution of size of CFRC until REV is determined

- Random fiber generation- From the uniform square cell, a random geometry is generated by adding a degree of randomness to the uniform position. The degree of randomness ($d_R = l_{shift}/r_{fiber}$) is defined by the ratio of distance the fibers l_{shift} moved from the position (o) of their square cell structure to the radius of the fiber (r_{fiber}) (Figure 3.6). l_{shift} varies depending on the volume fraction and with a condition that the fiber center is placed in such a way that it does not intersect with neighboring fibers. The movement is

also oriented in random angle. The angle (θ) in which the fiber center moved, decided by a random factor of $2\pi\vartheta$ where ϑ is the random number between 0 to 1. Below is an explanation of the randomization of a fiber from the square packed center o.

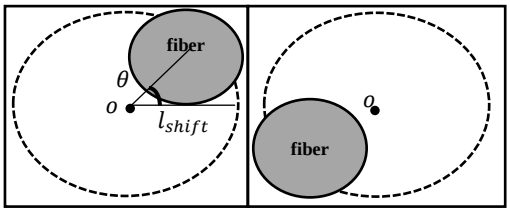


Figure 3.6 : Random positioning of the fiber

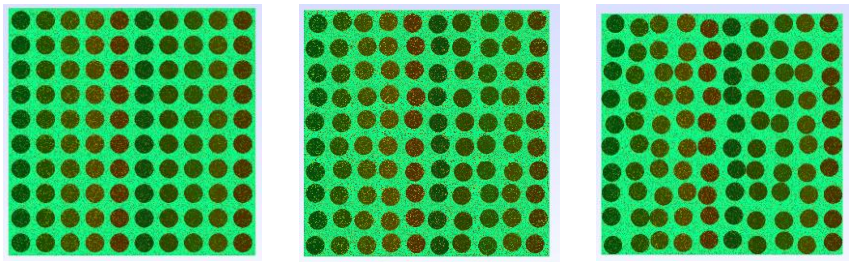


Figure 3.7 : Square packed to random position transformation for 0.45 volume fraction of fiber and with degree of randomness (a) 0 (b) 0.1 (c)0.25

- Cluster of fibers- Meshes with clustering of the fiber towards the central axis were also generated. The degree of shift towards the central axis, vertical or horizontal, is defined by the ratio of the distance the fibers changed position ($l_{cluster}$) from the square packed to the radius of the fiber (Figure 3.8). The degree of shift is higher for the fiber near to the central axis compared to the one near the boundaries. The general algorithm is presented in equation 3.20-3.23 where N_{fiber} is the number of fiber, $f_{shift}\sim(0 \rightarrow N_{fiber}-1)$, c is the coordinates with square packed. In the vertical direction, the change in position is governed by random factor in a way that it does not intersect with each other as shown in equation 3.23 where c_y is the y coordinate of square packed, rand $\sim(1 \rightarrow -1)$ and s is the maximum possible shift in vertical direction without intersection of surrounding fiber.

For fibers at central axis: $$l_{cluster} = 0 \quad (3.20)$$

For fibers on the left side of central axis: $$l_{cluster} = f_{shift}\, sin(\pi c/(2(N_{fiber}-1)10^{-5})) \quad (3.21)$$

For fibers on the right side of central axis: $$l_{cluster} = -f_{shift}\, sin(\pi c/(2(N_{fiber}-1)10^{-5})) \quad (3.22)$$

Vertical shift in position: $$y_{cluster} = c_y + (s\, rand) \quad (3.23)$$

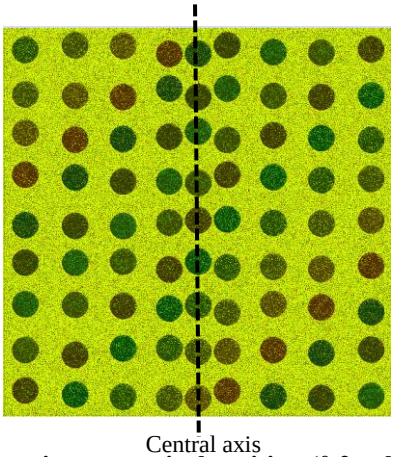


Figure 3.8 : Clustering on vertical position (0.2 volume fraction)

4.2 Boundary conditions

The homogenized REV represents a medium that has an overall thermal response representative of the macroscale and independent of the choice of boundary conditions (BC). However, in the case of CFRC, the locally heterogeneous thermal properties can lead to a strong thermal gradient or heat flux at the edges depending on the choice of BC. Therefore the question of a correct measurement of an effective thermal property of CFRC irrespective of the boundary condition is crucial. In the article by Jeulin [40], it was shown that if the length of the sample is greater than the diameter of the fiber, there are no fluctuations in the effective transversal thermal conductivity. However, at what exact factor the length should be increased, was not clearly discussed. Moreover, Kalamkarov et al. [30] and Hollister and Kikuchi [41] also show that the effect of boundary layers are more dominating when the REV is small. In his PhD dissertation, A. Matine [38] listed few methods present in the literature that deals with the boundary layer. However, he investigated that there is only one technique present that encounters the heat transfer study. This method remains very particular since it is based on an analytical solution obtained by the method of quadruples on a multilayered material. It cannot be generalized easily to different arrangement of fibers in a composite. Therefore he extended the models based on elasticity problem by H. Dumontet[42] and Arlequin[43] to deal with the edge effect in the context of periodic homogenization. Additionally, homogenization of the equation of transient heat conduction by the asymptotic expansion method was also done.

From these literature results, the presence of boundary layers was evident in the modeling of heat transfer in composite. It is therefore essential to choose properly the REV dimensions in a unidirectional composite depending on the chosen boundary conditions for homogenization. One of the controlling parameter is length, and thus to know the exact length of the sample necessary for effective properties to be independent of the boundary condition at the scale of REV is crucial.

In this preliminary study, the following boundary conditions were tested over various 3D meshes (section 4.1). It should be noted that for simplicity a 2D representation is selected for showing the boundary conditions.

- Dirichlet- Temperature is imposed over all boundaries Ψ^i with T=0 and T=1 on the two opposite faces of the sample depending on the desired effective conductivity estimation (Figure 3.9). Apart from the two faces, rest surfaces are imposed by a temperature gradient.

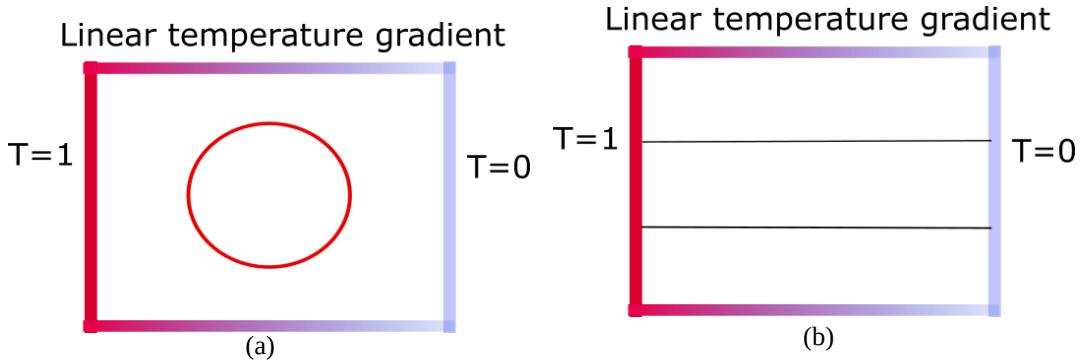


Figure 3.9 : Dirichlet boundary condition (a) transversal (b) axial

- Neumann- Flux (φ) is imposed over all boundaries $\Psi^i$where the opposite faces are at flux value of 1 and rest of the surfaces are under adiabatic condition.

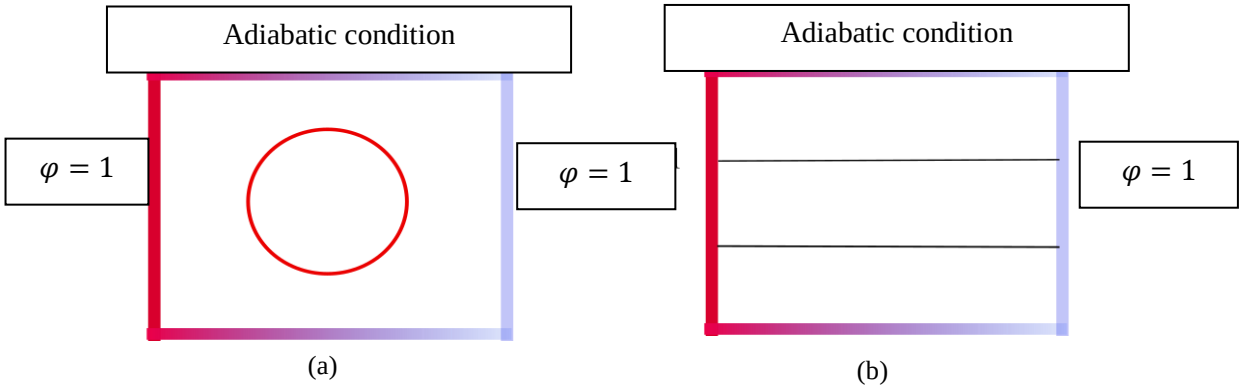


Figure 3.10 : Neumann boundary condition (a) transversal (b) axial

- Mixed- Similar to Figure 3.9, for mixed boundary condition, in this thesis the temperature is imposed on the surfaces where the desired gradient of temperature was required and the rest of the surfaces had adiabatic flux condition.

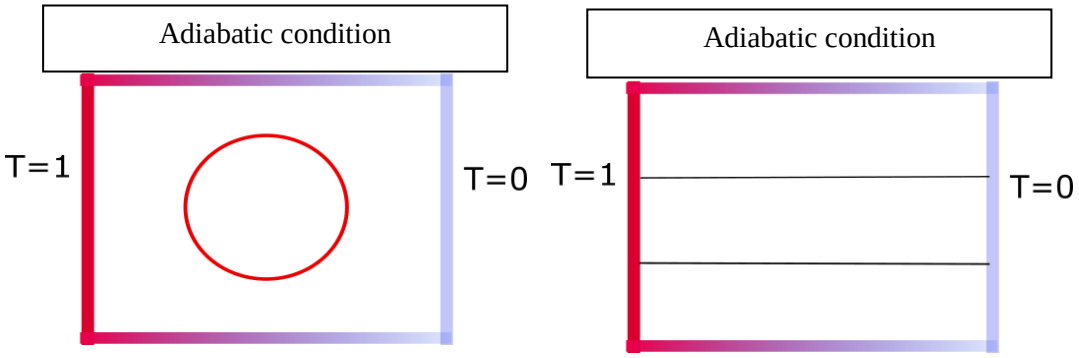


Figure 3.11 : Mixed boundary condition (a) transversal (b) axial

5. Results on Square Packed CFRC

5.1 Influence of Length on different Boundary conditions

In this section, the influence of change in length over the effective thermal conductivity tensor is discussed for various volume fractions of fibers. Different boundary conditions were tested. A square cell with volume fraction ranging from 0.2 to 0.6 were tested. The thermal conductivity of the material is as shown in table 3.1.

CFRC component[44]	Thermal conductivity (W $m^{-1}K^{-1}$)
Fiber	1.19 0 0 0 1.19 0 0 0 6.1
Matrix	0.22

Table 3.1: Material thermal conductivity

The diameter (D) of the fiber is set to 6.5µm, a quite realistic value for carbon fibers, and the length (L) is varied in such a way that the aspect ratio ($\sigma_r = L/D$) changes from 1 to 40 (Figure 3.12). Figure 3.13 shows the variation of effective axial thermal (K^*_{axial}) conductivity with change in aspect ratio for different volume fraction. Figure 3.14 shows the same for estimation of effective transversal thermal conductivity (K^*_{trans}). Please note that due to the particular geometry of tested REVs, the main axis of the conductivity tensor were assumed to be the ones of the physical frame used. The periodic approach is not sensitive to the orientation, but the simple analysis performed with the other boundary conditions would be slightly more complicated in case of an out-of-axis problem.

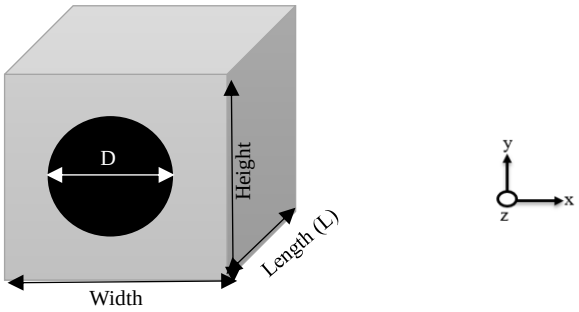
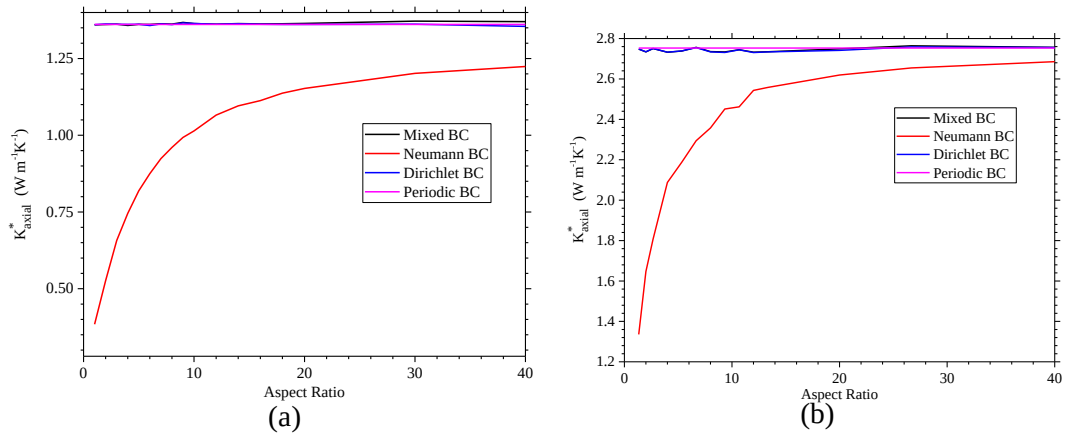
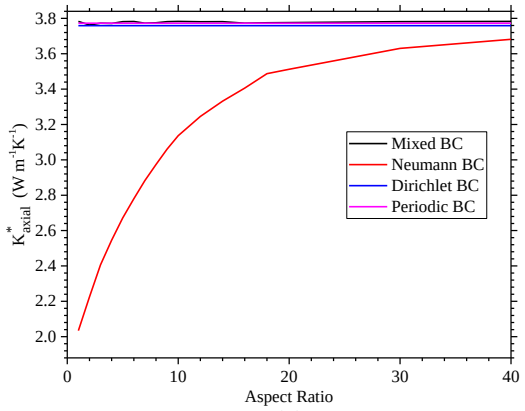


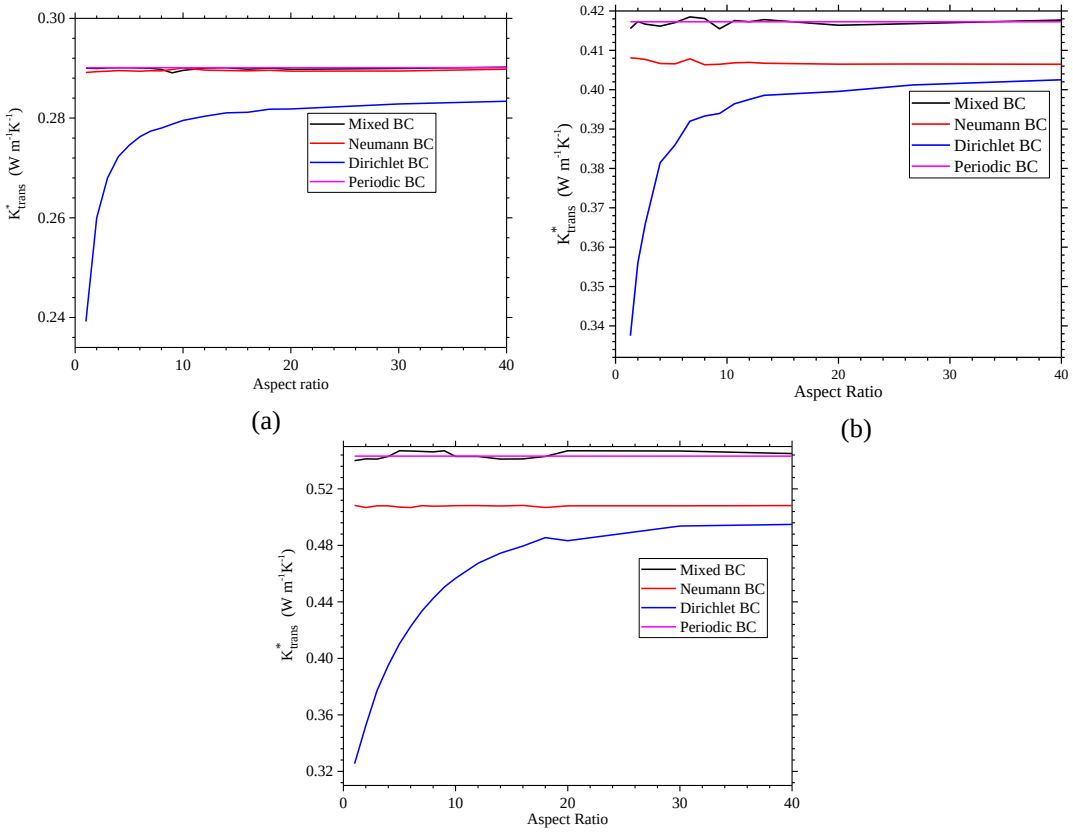
Figure 3.12 : Simple example of fiber in matrix





(c)

Figure 3.13: Variation of the effective axial thermal conductivity for different boundary conditions with change in the cell aspect ratio a_R and for volume fractions of (a)0.2 (b)0.45 (c)0.6.



(a) (b)

(c)

Figure 3.14 : Variation of the effective transversal thermal conductivity for different boundary conditions with change in the cell aspect ratio a_R and for volume fractions of (a)0.2 (b)0.45 (c)0.6

At the scale of REV, the effective properties should be independent of the length of the sample. However, it was observed that depending on the transversal or axial part of conductivity, there were certain boundary condition that were varying with the length. In particular for the estimation of axial thermal conductivity with the Neumann boundary condition and transversal thermal conductivity with the Dirichlet boundary condition are influenced by the length of the sample. However, it can be observed that after the aspect ratio of 20, the effective axial and radial thermal conductivity remain almost constant. Thus at this scale, there is no influence of boundary conditions on the estimation of thermal conductivity tensor. It can be seen that in case of transversal thermal conductivity, despite taking care of the length, the effective properties has

certain difference from the periodic approach. However mixed boundary condition is always giving constant effective properties and in good comparison with the periodic approach. Therefore, in general, the aspect ratio of 20 is sufficient for the current thermal contrast and this factor also remains the same irrespective to the change in volume fraction. Although for higher thermal contrast the edge effects would be more dominating thus the aspect ratio would significantly change.

The variation in the values of effective thermal conductivity in particular boundary conditions is due to the boundary effects that are dominating the heat flow. If we consider the results for the axial thermal conductivity as it can be seen from Figure 3.15. The temperature gradient at the surface has a sudden change (edge effect) in case of Neumann boundary condition when the length is small. With higher length the change in temperature gradient is present but due to increase in length, its overall effect on the volume is not dominant. This is the reason for the variation of results with length in Neumann boundary condition as the edge effect is dominant in small length. On the other hand in case of Dirichlet boundary condition, this problem is not present as the temperature is already predefined.

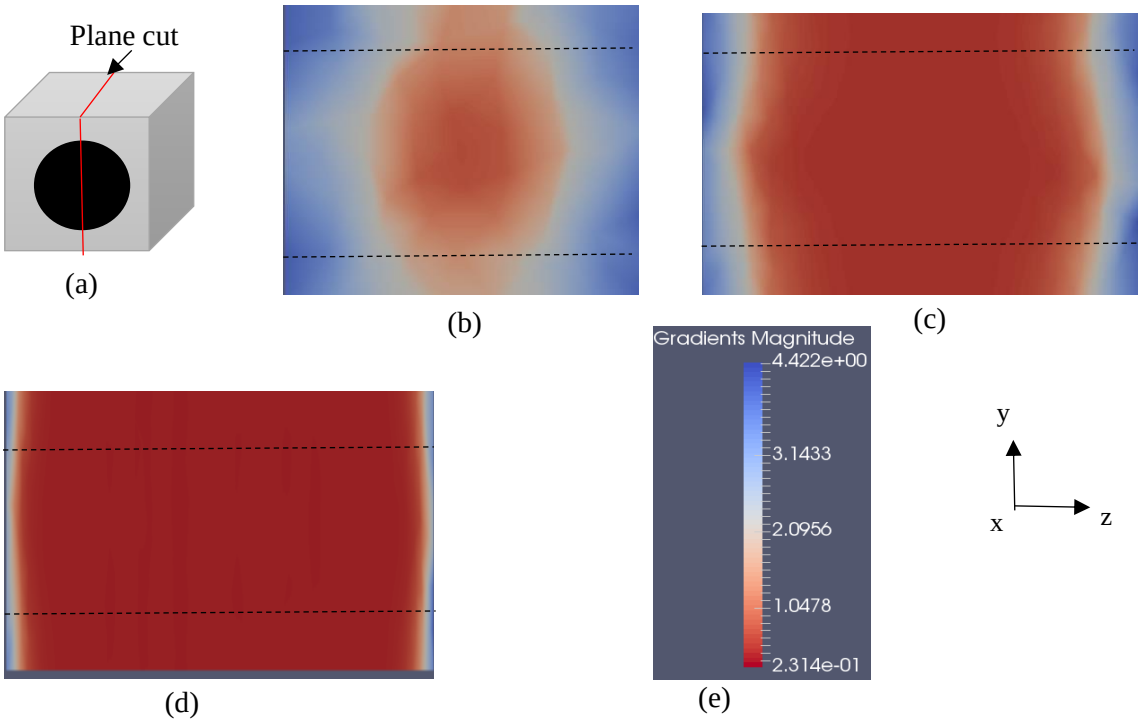


Figure 3.15 : Temperature gradient on the (a) cut plane along the fiber direction for axial thermal conductivity calculation with (b) small length (20µm). (c) Length 100µm (d) length 200µm (e) gradient scaling

Considering the case of transversal thermal conductivity, as shown in Figure 3.16 the variation in the result of the effective thermal conductivity in Dirichlet boundary condition is due to the positive and negative flux in the proximity of the fibers and matrix interface. This is expected to affect the temperature distribution in the middle. But if we take a longer length then this might not affect the temperature distribution in the core of the material. Therefore, considering good aspect ratio is crucial for estimation of effective thermal conductivity.

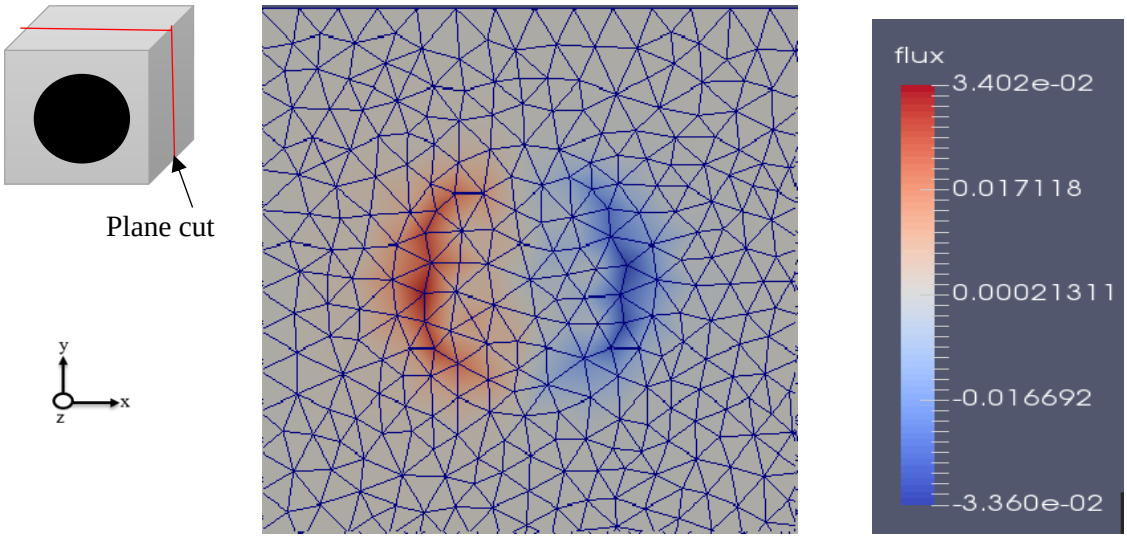


Figure 3.16 : Flux on the surface in case of Dirichlet boundary condition at the plane cut

5.2 Representative elementary volume of uniform square cell

In the previous section, the influence of the cell length on the homogenized conductivity tensor when using various boundary conditions was analyzed and it gave a certain aspect ratio factor in order to make accurate effective thermal conductivity tensor estimation. Keeping this preliminary assumption in consideration for all the geometries, representative elementary volume was determined. However, a REV determination for shorter lengths was also carried out. Figure 3.17 and 3.18 show the effective thermal conductivity tensor for different boundary conditions. Two lengths of meshes were considered depending on the aspect ratio of 5 and 30. Volume fractions from 0.2 to 0.6 were analyzed. The REV is determined by the size at which the effective thermal conductivity is constant. The size of the sample is defined by sample window ($\propto$) which is the square root of total number of fibers present ($\propto = \sqrt{n_{fibers}}$). The result of conductivity tensor at each $\propto$ is also compared with periodic boundary conditions. The periodic assumptions are very attractive since exact effective properties are computable for the most basic case.

From Figure 3.17, it can be observed that in the case of axial thermal conductivity, the Dirichlet, Mixed and Periodic boundary condition is giving similar result irrespective to the length of the sample. The deviation in the axial thermal conductivity value for multiple lengths with the Dirichlet and Mixed boundary conditions and increasing $\propto$ are shown by the error bar in each plot. With Neumann boundary condition at higher length or aspect ratio showed convergence of the conductivity value with increasing $\propto$. However, with the Neumann boundary condition, the shorter length geometry couldn't determine the REV. In case of transversal thermal conductivity (Figure 3.18), the determination of REV with Dirichlet has shown significant improvement with longer length mesh than a shorter one while rest boundary conditions gave a more or less similar value of effective transversal conductivity. These outcomes are constant for higher volume fraction also. Therefore, it can be concluded that the effective conductivity tensor depends not just on the size (width by height) of the microstructure considered, but also on its length and the boundary conditions.

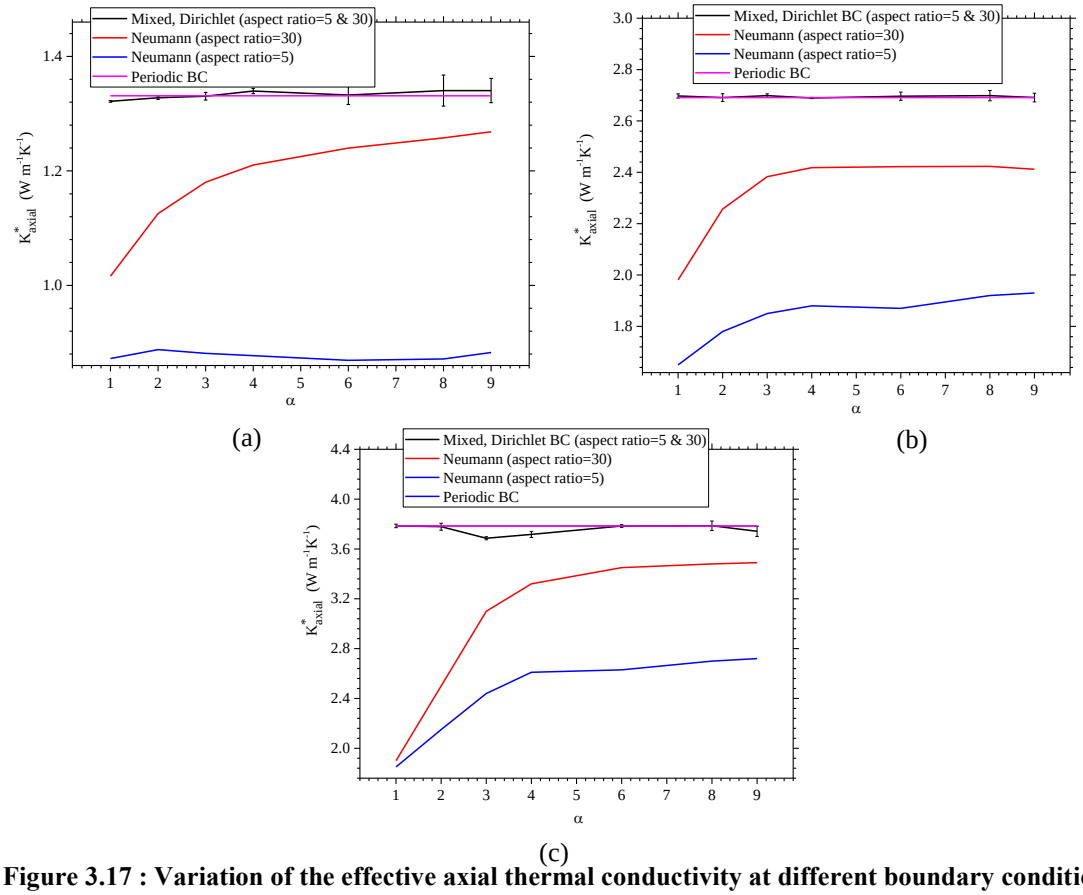


Figure 3.17 : Variation of the effective axial thermal conductivity at different boundary conditions with the number of fibers at different volume fraction (a) 0.2 (b) 0.45 (c) 0.6

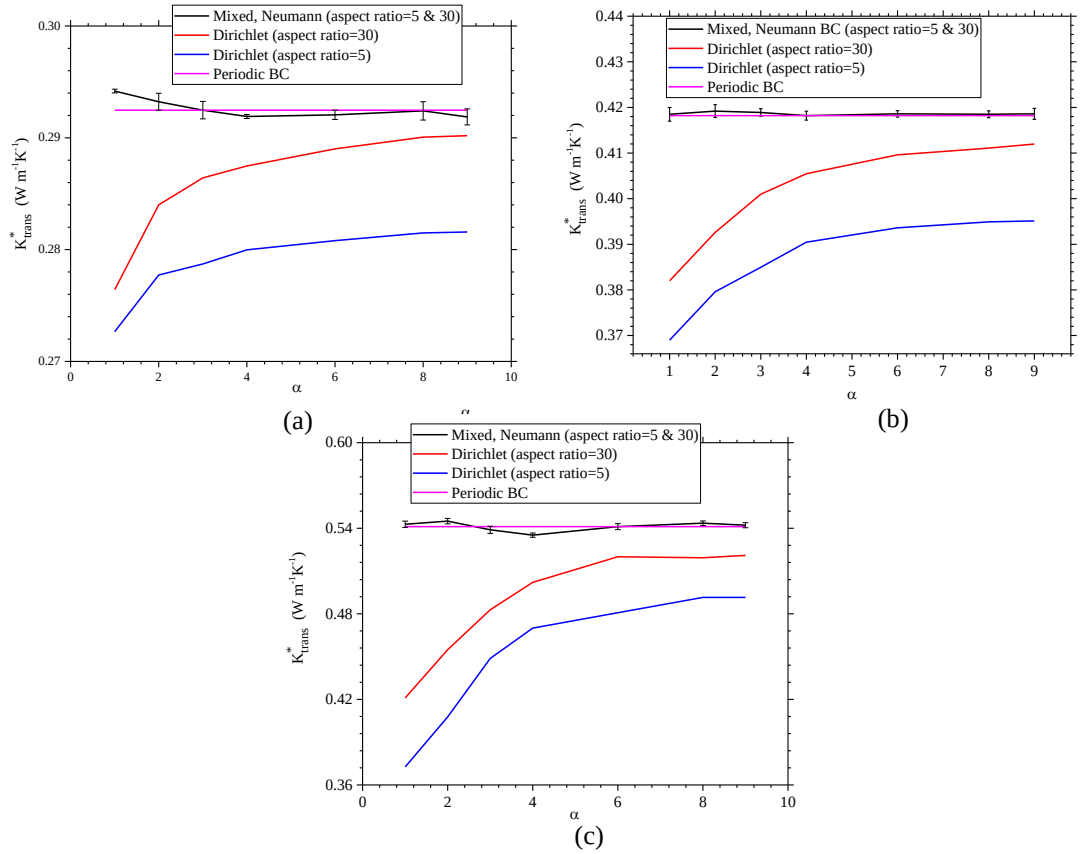
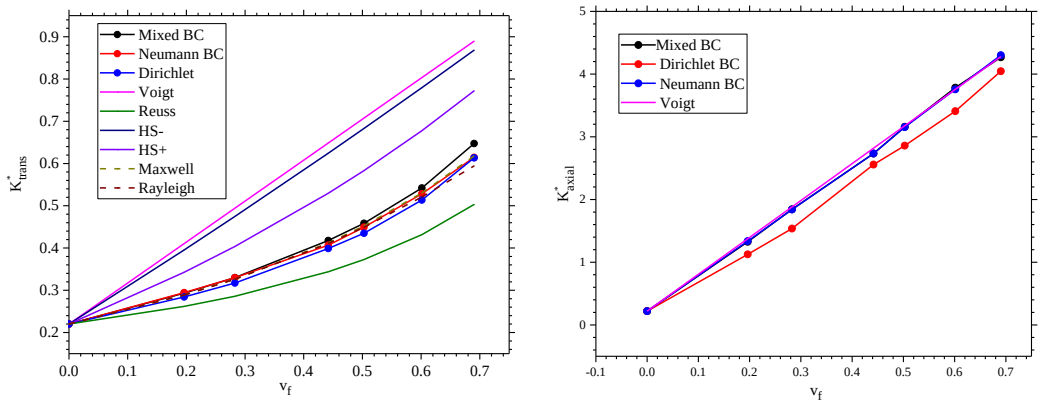


Figure 3.18 : Variation of the effective transversal thermal conductivity at different boundary conditions with the number of fibers at different volume fraction (a) 0.2 (b) 0.45 (c) 0.6

It can be realized that the edge effect serves as a prime factor in determining the effective thermal conductivity. It's important to note that the mixed boundary condition and periodic boundary condition don't show such a problem and should be preferred in any homogenization process. Nevertheless, the applicability of periodic boundary condition on the complex geometry is sometimes more difficult. Therefore, choosing a mixed boundary condition for different studies can be seemed interesting, provided the microstructure lies exactly in the axes of the used frame.

5.3 Influence of Volume fraction

At the scale of REV, it is important to study the influence of volume fraction of the fiber on the estimated anisotropic thermal conductivity tensor. The theoretical models discussed in section 2.4 have good efficiency in predicting the effective conductivity of the REV. However, it should be noted that these models are extensively used only in the case of transversal thermal conductivity. Figure 3.19 shows the effective thermal conductivity estimated numerically for different fiber volume fractions using the unit cell approach. In the case of transversal thermal conductivity, the numerical results are within the range of Voigt-Reuss bounds along with the Maxwell and Rayleigh model. Although, the prediction of literature about Hashin-Shtrikmann bound providing tighter range holds true in the result but the effective thermal conductivity estimated numerically is not within the bound. This could be due to the thermal contrast limitation of this model. However, the effective transversal thermal conductivity predicted by numerical model is in good agreement with the Rayleigh and Maxwell model and is in the bound of Voigt Reuss. In case of axial, the numerical results showed that the effective axial thermal conductivity is in proximity to the Voigt or mixing model, which is not surprising.



(a) (b)

Figure 3.19 : Variation of the effective (a) transversal (b) axial thermal conductivity at different boundary conditions with the volume fraction of fiber (aspect ratio of 20).

6. Results on Random distributed fibers in CFRC

6.1 Influence of Randomization and Clustering

Prior to this section, the computations were only conducted for the uniform square packed fibrous composite contrary to the reality where the position is not so strongly uniform. Therefore, it's essential to verify how the distribution of the fiber position, by randomization or clustering, can affect the effective property measurement. For simplification a position factor, $p_f = {l_{shift}}/{D}$ is defined which is the ratio of the shift ($l_{cluster}$ or l_{shift} depending on clustering and randomization) in the position of the fiber from the uniform square cell to the diameter of the fiber(D). At each p_f, multiple geometries (8 cases) were tested by choosing different random angular direction of movement (section 4.1). Figure 3.20(a), where calculations were performed for a fiber fraction of 0.45, shows that the axial effective thermal conductivity is independent of the change in position. This is due to the reason that in the axial direction, the fiber dominates the heat flow and no overall change in the heat current in case of axial conduction. However, in the case of effective transversal (Figure 3.20(b)) conductivity tensor, there is a small change (<5%) from the square packed cell for the estimation with an increase in the position factor of randomization and clustering (Figure 3.21). Though such an effect should be stronger for a higher contrast in the constituent properties, there is in practice no significant change in the result due to this randomization. This trend was also observed for different volume fraction. However in the current appraoch the limitations are fibers percolation cases could not be studied by the present approach because of meshing difficulties. More significant changes can be expected if a percolating path in the fibrous phase is reached, which can be the case at fiber fractions around 60% volume fraction.

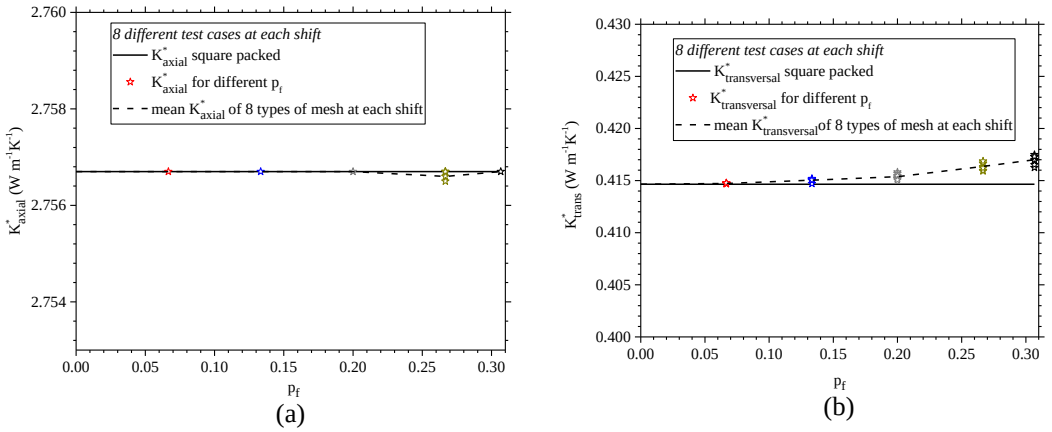


Figure 3.20 : Effect of randomization in the fiber position at different p_f on (a) axial (b) transversal thermal conductvity for fiber volume fraction of 0.45.

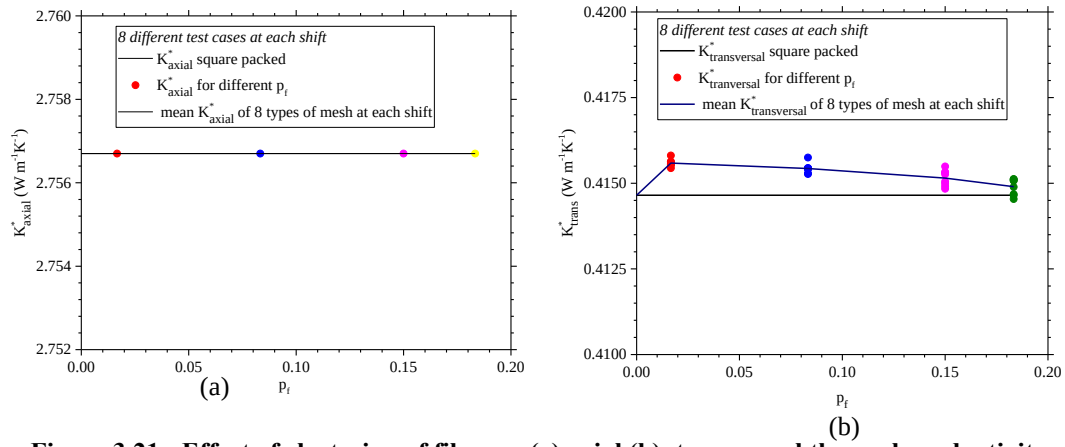
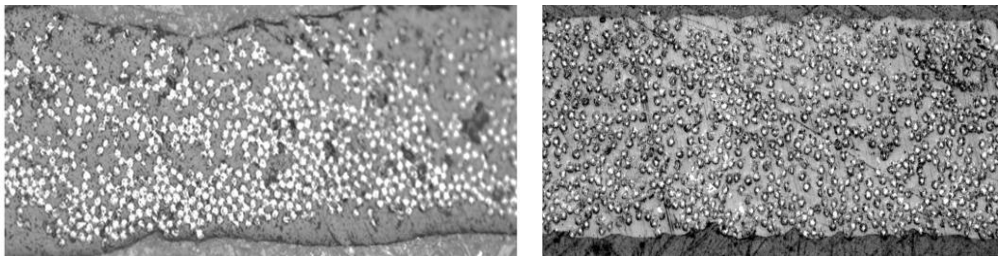


Figure 3.21 : Effect of clustering of fiber on (a) axial (b) transversal thermal conductivity

6.2 REV and Homogenization in tapes

A prepreg tape is a laminated pre-engineered material for the manufacturing of CFRC at macroscale. In advanced manufacturing processes such as AFP or ATP, the tapes are deposited one over another along different orientations to form a final laminate. The thermal properties of the constituents, which are AS4 fiber and PEEK matrix for these tapes (Table 3.1). Most of the research on the thermal behavior of tapes have the primary assumption of treating tapes as homogenous media (detailed discussion in Chapter 4). However, from the micrographs on these tapes (Figure 3.22), primarily shows that the homogeneity is yet questionable.



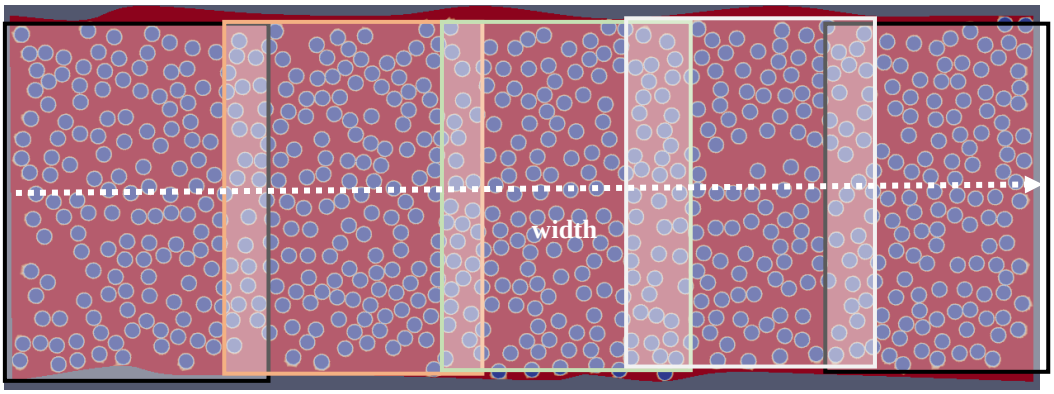
(a) (b)

Figure 3.22 : Microscopic image of (a) Solvay (b) Suprem tapes

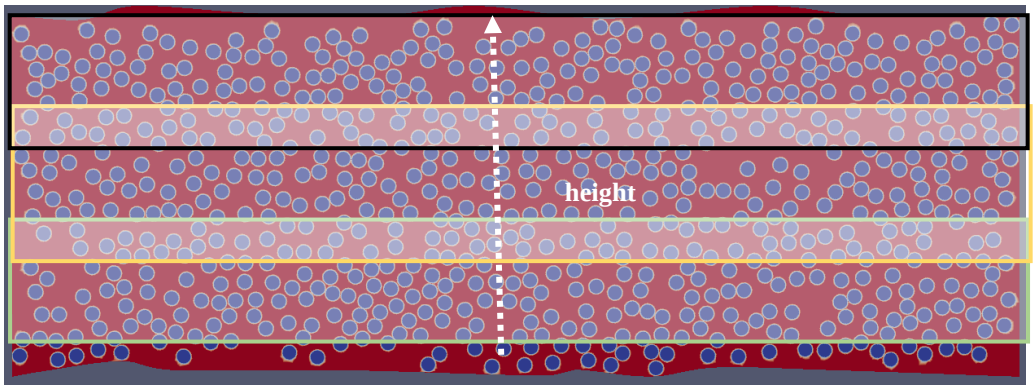
The huge difference in the distribution of fibers between the two commercial tapes, Solvay and Suprem, encourages to study the thermal REV of those microstructures, especially in transversal direction. A detailed description of the meshing from this microstructure is present in the upcoming chapter.

In this section, the effective transversal thermal conductivity prediction of the tapes are shown. This was done by scanning the tapes through different sections and performing unit cell approach over each section using mixed boundary condition depending on the desired direction (section 3.3). The number of sections chosen for scanning are reduced, attaining larger volume of tapes under consideration thus slowly moving towards the representative volume of the macroscale. Figure 3.23 shows an example of the scanning performed over Suprem tape through different sections or windows along the width and along the height. For both Solvay and Suprem tapes, the width of the window increased from 45µm to 400 µm and scanned through the overall

volume. Along the height, the window is increased from 20µm to 160µm. This size depends on the width and height of the mesh generated from the micrograph.



(a)

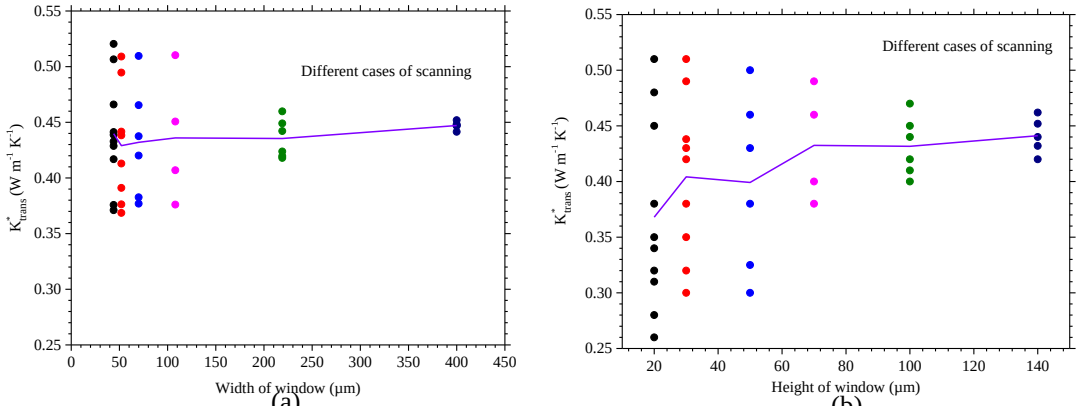


(b)

Figure 3.23 : Scanning of a Suprem tape along the (a) width (b) height

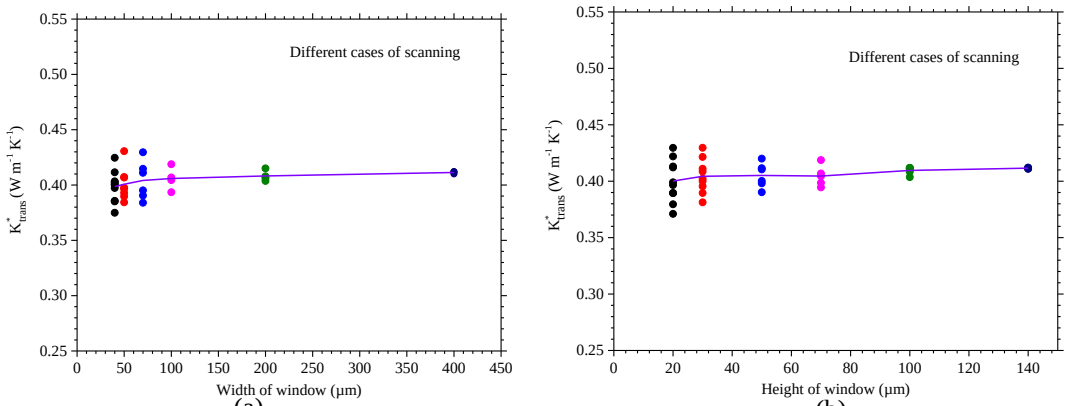
Figure 3.24 (a) and (b) shows the effective transversal thermal conductivity of windows scanned through the Solvay tape along width and height respectively. Figure 3.25 shows the same for Suprem tape. In case of Solvay tape, the scattering of effective transversal thermal conductivity is large, 0.37 – 0.53 W $m^{-1}K^{-1}$ at smaller window to 0.43-0.46 W $m^{-1}K^{-1}$ for a window of width nearly equal to the width of the mesh. The mean (–) of all data at different width of scanning showed more or less stable effective thermal conductivity. For scanning along the height, it can be observed that the scattering was increased (0.25-0.52). This is due to the inhomogeneity in the distribution of the fibers and matrix and especially along the height there is layer of only matrix present in the micrograph (Figure 3.22 (a)). Even the mean of data at different height of scanning had the highest scattering as compared to other cases where the mean is more or less stable. In contrary to this, the Suprem has rather homogenous distribution of fibers in the matrix (Figure 3.22 (b)). Therefore, it can be seen in Figure 3.25 that the scattering of the effective thermal conductivity is far less than the Solvay tape and at bigger window, both along the width and height, it has shown a rather constant value of conductivity for different section. Therefore, in case of Suprem the homogeneity is attained conveniently for a bigger window and the effective thermal conductivity is 0.41 W $m^{-1}K^{-1}$. The mean (–) of effective thermal conductivity estimated at different width or height had a stable result. Therefore the choice of the window size is crucial, that is large window had high computational cost but low error or else small window with higher

uncertainty. Further Figure 3.26 shows the variation of effective conductivity at different y depth of Solvay tape. It could be seen that the maximum effective conductivity is indeed at a particular depth for scanning with smaller height of window such as 20 and 30µm. This could be due to the localization in fiber distribution at a certain depth (leading to high conductivity) contrary to the other depths where the presence of matrix is dominating. Yet a further analysis on the distribution of fiber density in the tapes and its correlation with the conductivity would be interesting to solve in the near future.



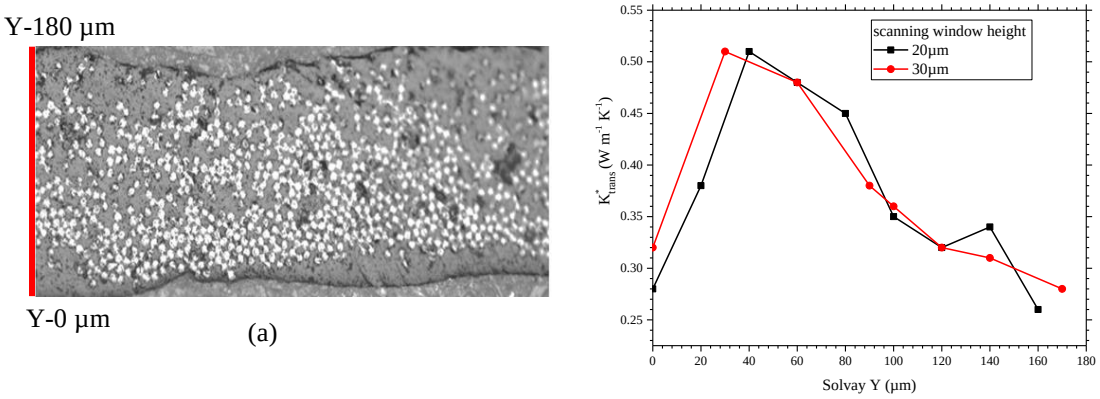
(a) (b)

Figure 3.24 : Effective tranversal thermal conductivity for Solvay tape by scanning window along different (a) width (b) height



(a) (b)

Figure 3.25 : Effective tranversal thermal conductivity for Suprem tape by scanning window along different (a) width (b) height



(a) (b)

Figure 3.26 : (a) Solvay tape at different Y (b)Effective tranversal thermal conductivity for Solvay tape at different scanning height window.

7. Partial Conclusion

The complexity in the real microstructure led to the inapplicability of the direct theoretical models. This chapter aimed to estimate the effective thermal properties of a mesoscale structure starting from the one with square packed to the real microstructure of the tapes. The homogenized medium generally has effective properties that remain constant with the change in the applied boundary condition. However, it was found out that the choice of the boundary condition plays an important role in the determination of effective properties as at certain boundary condition, the edge effect is dominant making wrongful prediction of effective properties. Studies were made for different volume fraction and it was found out that after a certain length of the geometry for each microstructure, defined by the cell aspect ratio, the effective properties are not influenced by the boundary condition. The mixed boundary conditions showed results not influenced by the length of the geometry. The smaller length also influences the determination of REV for different volume fraction.

Tests were also made on random distribution and there was no significant change in the conductivity tensor was observed as compared to square packed (<5%). Homogenization was also carried out on the Solvay and Suprem tapes used in the following chapter, with cells containing up to approximately 700 fibers. It was observed that the Suprem tapes are easily homogenizable due to the good distribution of the fibers in the matrix. However, the band or scattering of effective transversal conductivity in Solvay tapes were huge due to the irregularity in the fiber distribution. In the next chapter, a detailed description of the homogenizability of the tapes will be presented. And can be checked in that case that one needs almost the entire height of samples to get a stable (representative) answer. This of course includes all the possible edge effects and structure modifications in the vicinity of the upper and lower surfaces and is unfortunately the sign of a non homogenizable situation, where the microscale calculation is necessary.

References

[1] Fish J and Yu Q 2001 Multiscale Damage Modeling for Composite Materials : Theory and Computational Framework 2 . 0 Mathematical Homogenization for Damaged Composites *Int. J. Numer. Methods Eng.* **52** 161–91

[2] Gruer F O 2015 Multiscale numerical modelling of microstructured reinforced composites

[3] Yang L, Wu Z, Gao D and Liu X 2016 Microscopic damage mechanisms of fibre reinforced composite laminates subjected to low velocity impact *Comput. Mater. Sci.* **111** 148–56

[4] Mishnaevsky L L and Schmauder S 2009 Continuum Mesomechanical Finite Element Modeling in Materials Development: A State-of-the-Art Review *Appl. Mech. Rev.* **54** 49

[5] Selvakumar M, Ramkumar T and Chandrasekar P 2019 Thermal characterization of titanium--titanium boride composites *J. Therm. Anal. Calorim.* **136** 419–24

[6] Boussatour G, Cresson P Y, Genestie B, Joly N, Brun J F and Lasri T 2018 Measurement of the thermal conductivity of flexible biosourced polymers using the 3-omega method *Polym. Test.* **70** 503–10

[7] Wang R, Zobeiri H, Lin H, Qu W, Bai X, Deng C and Wang X 2019 Anisotropic thermal conductivities and structure in lignin-based microscale carbon fibers *Carbon N. Y.* **147** 58–69

[8] Liu J, Qu W, Xie Y, Zhu B, Wang T, Bai X and Wang X 2017 Thermal conductivity and annealing effect on structure of lignin-based microscale carbon fibers *Carbon N. Y.* **121** 35–47

[9] Srinivasan M, Maettig P, Glitza K W, Sanny B, Schumacher A, Duhovic M and Schuster J 2016 Out of Plane Thermal Conductivity of Carbon Fiber Reinforced Composite Filled with Diamond Powder *Open J. Compos. Mater.* **06** 41–57

[10] Gori F and Corasaniti S 2014 Effective thermal conductivity of composites *Int. J. Heat Mass Transf.* **77** 653–61

[11] Goyhénèche J M and Cosculluela A 2005 A multiscale model for the effective thermal conductivity tensor of a stratified composite material *Int. J. Thermophys.* **26** 191–202

[12] Plana V 2003 *Caractérisation par méthode inverse et modélisation des propriétés thermophysiques orthotropes des matériaux composites* (L'ecole national superieure de l'aeronautique de l'espace)

[13] Li Q 2006 Homogenization for composite material properties using smoothed finite element method 1–40

[14] Thomas M 2008 Propriétés thermiques de matériaux composites : caractérisation expérimentale et approche microstructurale *Ec. Polytech. l'Université Nantes* 253

[15] Moussaddy H 2013 *A New Definition of the Representative Volument Element in Numerical Homogenization Problems and its Application to the Performance Evaluation of Analytical Homogenization Models.* (Universite de Montreal)

[16] Hill R 1963 Elastic properties of reinforced solids: Some theoretical principles *J. Mech. Phys. Solids* **11** 357–72

[17] Drugan W J and Willis J R 1996 A micromechanics-based nonlocal constitutive equation and estimates of representative volume element size for elastic composites *J. Mech. Phys. Solids* **44** 497–524

[18] Gusev A A 1997 Representative volume element size for elastic composites: A numerical study *J. Mech. Phys. Solids* **45** 1449–59

[19] Jiang M, Jasiuk I and Ostoja-Starzewski M 2002 Apparent thermal conductivity of

periodic two-dimensional composites *Comput. Mater. Sci.* **25** 329–38

[20] Ostoja-Starzewski M 2006 Material spatial randomness: From statistical to representative volume element *Probabilistic Eng. Mech.* **21** 112–32

[21] Moussaddy H 2013 A New Definition of the Representative Volument Element in Numerical Homogenization Problems and its Application to the Performance Evaluation of Analytical Homogenization Models. *Thesis*

[22] Kouznetsova V, Brekelmans W A M and Baaijens F P T 2001 Approach to micro-macro modeling of heterogeneous materials *Comput. Mech.* **27** 37–48

[23] Hasselman D P H and Johnson L F 1987 Effective Thermal Conductivity of Composites with Interfacial Thermal Barrier Resistance *J. Compos. Mater.* **21** 508–15

[24] Noh H G, Lee J H, Kang H C and Park H S 2017 Effective Thermal Conductivity and Diffusivity of Containment Wall for Nuclear Power Plant OPR1000 *Nucl. Eng. Technol.* **49** 459–65

[25] Pietrak K and Wiśniewski T 2015 A review of models for effective thermal conductivity of composite materials *J. Power Technol.* **95** 14–24

[26] Tandon G P and Weng G J 1984 The effect of aspect ratio of inclusions on the elastic properties of unidirectionally aligned composites *Polym. Compos.* **5** 327–33

[27] Mori T and Tanaka K 1973 Average stress in matrix and average elastic energy of materials with misfitting inclusions *Acta Metall.* **21** 571–574

[28] Castaneda P, Telega J J and Gambin B 2003 Nonlinear Homogenization and its Applications to Composites, Polycrystals and Smart Materials *NATO Advanced Research Workshop* (Warsaw, Poland)

[29] Benveniste Y 1987 A NEW APPROACH TO THE APPLICATION OF MORI-TANAKA'S THEORY IN COMPOSITE MATERIALS *Mech. Mater.* **6** 147–57

[30] Kalamkarov A L, Andrianov I V. and Danishevs'kyy V V. 2009 Asymptotic Homogenization of Composite Materials and Structures *Appl. Mech. Rev.* **62** 030802

[31] Chen Q, Wang G, Chen X and Geng J 2017 Finite-volume homogenization of elastic/viscoelastic periodic materials *Compos. Struct.* **182** 457–70

[32] Brockenbrough J R, Suresh S and Wienecke H A 1991 Deformation of metal-matrix composites with continuous fibers: geometrical effects of fiber distribution and shape *Acta Metall. Mater.* **39** 735–52

[33] Michel J C, Moulinec H and Suquet P 1999 Effective properties of composite materials with periodic microstructure: A computational approach *Comput. Methods Appl. Mech. Eng.* **172** 109–43

[34] Honle S 1998 *Micromechanical Modelling of Deformation and Fracture of Graded WC/Co Hard Metals* (University of Stuttgart)

[35] Trias D 2005 *Analysis and Simulation of Transverse Random Fracture of Long Fibre Reinforced Composites*

[36] Dong M and Schmauder S 1998 Erratum to " Transverse mechanical behaviour of fiber reinforced composites : FE modelling with embedded cell models " **0256** 1998

[37] Knight M G, Wrobel L C and Henshall J L 2003 Micromechanical response of fibre-reinforced materials using the boundary element technique *Compos. Struct.* **62** 341–52

[38] Matine A 2013 *Homogénéisation des transferts thermiques par développements asymptotiques dans des structures composites avec prise en compte des effets de bords* (Polytech Nantes)

[39] Mael Peron 2016 *Mesure et modélisation des phénomènes de retaits anisotropes dans les matériaux composites durant leur mise en forme* (University of Nantes)

[40] Jeulin D 2001 *Homogénisation en mécanique des matériaux (tome1)* (Hermes, France)

[41] Hollister S J and Kikuchi N 1992 A comparison of homogenization and standard mechanics analyses for periodic porous composites *Comput. Mech.* **10** 73–95

[42] Dumontet H 1990 *Homogeneisation et effets de bords dans les materiaux composites* (L'université Pierre et Marie Curie Paris)

[43] Rateau G 2003 *Méthode Arlequin pour les problèmes mécaniques multi-échelles : applications à des problèmes de jonction et de fissuration de structures élancées* (Ecole centrale de Paris)

[44] Le Louet Violaine 2018 *Etude du comportement thermique de bandes composites pre-impregnees au cours du procede de fabrication AFP avec chauffage laser* (Universite de Nantes, France)

Chapter 4

Thermal behavior of tapes in automated tape placement at the scale of fibers

1. Introduction **92**
2. Literature Review on AFP **93**
2.1 Typical AFP process: 93
2.2 Thermoplastic over thermoset matrix: 94
2.3 Temperature driven AFP process: 95
2.4 Literature on thermal modeling of the AFP process: 96
3. Experimental Setup **97**
3.1 Measurement of Average Top Surface Temperature 99
4. Micro-scale numerical modelling on the tapes **100**
4.1 Motivations 100
4.2 Image Processing 101
5. Heat source distribution **104**
6. Numerical model **105**
6.1 Material Properties 106
6.2 Averaging technique for temperature measurement by numerical model 107
6.2 Mesh and Time Convergence 109
7. Results by numerical modeling **110**
7.1 Heat flow by μ-calculation 110
7.2 Temperature variation along the height 112
7.3 Temperature variation of the top surface with time 113
7.4 Influence of rear face contact on temperature measurement on the tops surface 114
9. Partial Conclusion **116**
References **118**

1. Introduction

The huge demand for composite materials in multiple industrial sectors such as automobile, aeronautics, construction and many more, as mentioned in chapter 1, led to the necessity of advanced manufacturing techniques. Traditional methods are time consuming as well as economically expensive due to the involvement of human labor. Additionally, the reduction of mechanical strength due to the inaccuracies such as voids and deformities during production is also problematic. In the past few decades, there are developments of specific processes, especially automated one, which would satisfy the need of high production of composite with better accuracy. Industrially, the widely accepted mechanized manufacturing techniques are Filament Winding (FW), Automated Tape layup (ATL) and Automated Fiber placement (AFP) [1]. FW has multiple filaments, winding over a rotating mandrel in a different orientation to produce circular or oval sectioned components. Regardless of the stagnant growth in the past, FW is being employed in multiple industries with the surge of automation software and machinery [2] . However, its use is limited to a particular shape unlike the ATL and AFP techniques, used for fabrication of large uniaxial work pieces and for production of complex shapes respectively[3]. The implementation concept remains however common to both techniques. It is based on the successive stacking in a mold layers of unidirectional carbon fibers thin (around 150µm) pre-impregnated thermosetting matrix.

Research on this technique (AFP) is widely focused on the macro scale behavior of the composite as discussed in section 2. This chapter focuses on overcoming certain limitations of the previous researches (section 2) that can be achieved by studying the thermal behavior of the tape during an AFP process at the microscale. In order to fulfill this objective, the in-house experimental bench used in the thesis of Violaine Le Louët is described in section 3. However, our motivation was to understand numerically what is happening at the scale of single tape (section 4.1). A three dimensional (3D) meshes are generated from optical microscopic images (section 4.2). In this work, we consider the case where the laser heating has a normal incidence with respect to the top surface of the tape. Similar to a ray tracing technique, the zones of the fibers impacted by the laser rays are first detected (section 4). It should be noted that the current study does not consider reflection from the fiber surface. Fibers are considered to be an absorbing medium and the matrix was assumed to be transparent[4]. The heat source distribution for different tapes while heating with the laser are discussed in details in section 5.

The rear side of the tape accounts for the roughness of the imperfect contact with the steel bench. The transient heat transfer equation is solved by FEM (section 6) over the tape volume for a total time period of 200 ms out of which the tape was heated by a laser beam for 25 ms. Multiple numerical results such as average temperature along the depth of the tape, the influence of RTC on the average temperature estimation, along with a comparison of the average surface temperature observed during experiments and numerical model is shown in section 7.

2. Literature Review on AFP

2.1 Typical AFP process:

A typical AFP process involves the use of a motorized placement head to place the composite prepreg tapes layer by layer to build up a final laminate after passing through heating, consolidation and cooling phase (Figure 4.1). The bonding of the surfaces involves intimate contact, realized by pressure application (roller), during heating by a given source. Previously, hot gas torch was used as a heat source due to their low cost but the processing costs were higher as it needed a nitrogen environment for preventing oxidation. Furthermore the overall heating was limited because of this convective mode of heating. Therefore, recently laser diode with higher energy density and instantaneous response with better process control, have come to the use [7][8]. The heating phase should be long enough to ensure the melting temperature is reached. Furthermore, the overheating of the sample should be avoided as it might cause a degradation in the tape because of chain scission primarily in the carbonyl linkage leading to crosslinking reactions[6].

Subsequently with heating, there is pressing by a roller in the consolidation phase and later releasing the laminate to cool under atmospheric condition. The roller can be a simple cylindrical shape or conformable rollers that assist in placement on a curved surface [9]. The strength of the laminate is high when the bonding between the substrate and tape becomes strong. This is possible due to the decrease in the polymer viscosity during heating and increases the chances of better contact at the interface, also known as intimate contact. This highly depends on the surface constraints, and the applied temperature and pressure [10]. Moreover, the intermolecular diffusion of the interface with intimate contact between the substrate and the tape due to autohesion increases the overall strength of the laminate[11]. Thus the phenomena of heating, pressing and autohesion are highly correlated.

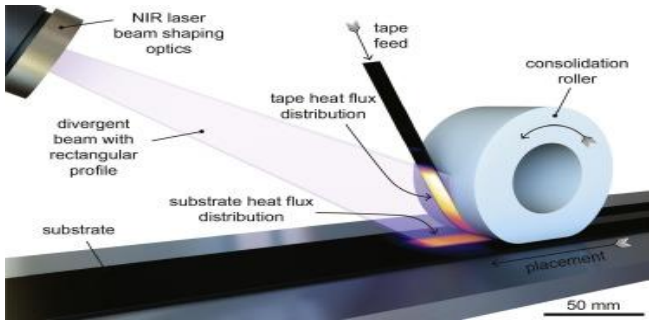


Figure 4.1: Schematic diagram of AFP process[8]

The different benefits of the AFP manufacturing technique make it stand out among other manufacturing techniques. These are[5][6]:

- Complex structure manufacturing
- Accurate fiber placement and quality improvements
- Quality improvements
- Labor-saving
- Low mold production time

Regardless of these benefits, the automation manufacturing techniques can suffer from energy inefficiency, economic incompetence and time-consuming depending on the choice of thermoset as the matrix.

2.2 Thermoplastic over thermoset matrix:

At the consolidation phase of AFP, the matrix of the prepreg and the substrate bond together by crosslinking at the interface. The thermoset matrix goes through an irreversible polymerization during the bonding. The substrate becomes much stiffer than its upcoming tape, making the bonding and passing to the mold rather difficult. The difficulty also arises if the matrix is semi-crystalline as it necessitates the use of higher processing temperature and the final product quality is highly susceptible to the thermal environment [12].

The thermoset matrix is generally cured in an autoclave under a controlled environment of temperature and pressure to remove the voids and guarantee a higher product quality. However, this operation is quite expensive and is currently motivating researches to transform it to out-of-Autoclave (OoA) state [13–15]. Besides the choice of OoA, a great industrial interest is present in changing the matrix to a thermoplastic material. The advantages of thermoplastic materials over the thermosets are[6][16–18]:

- Short cycle time as no curing and refrigeration are required.
- Recyclability makes it near infinite shelf life.
- Extreme toughness and higher fracture resistance.
- Stable Tg (glass transition temperature).
- Low level of moisture uptake.
- Higher chemical stability.
- Higher resistance to impacts

Table 4.1 shows a comparison of a few properties between thermoplastic and thermoset matrices.

Type	Matrix	Ultimate tensile stress (MPa)	Module of Traction (MPa)	Density	Glass transition temperature	Fusion temperature
Thermoset	Epoxy	80	3600	1.3	180	N/A
Thermoplastic	PPS	65	3800	1.35	90	283
	PEEK	100	3600	1.3	143	343
	PEKK	110	4400	1.27	162	305-360

Table 4.1: Comparison of properties between thermoset and thermoplastic materials [19]

The lack of autoclave in the thermoplastic composite always leads to an increase in void growth that ultimately leads to defects such as porosities and lowers final quality of the product. Currently, the parts made by placing thermoplastic strips always require a post-consolidation autoclave. In the thesis of Kok [17], various models that define the growth of the voids were studied. He consolidated the prepreg tape in-situ that is during placement, eliminating the expensive post consolidation step. Currently, thermoplastic is being used in various parts in an airplane such as hoses[20], welded ribs, stamp formed clips[17] and many more. Yet its acceptance to replace the thermoset composite in large sized components is rather slow[6][17]. This can be possible by better understanding each phenomenon involved during the manufacturing of thermoplastic composite by the AFP process.

2.3 Temperature driven AFP process:

The general objective of the AFP process is to have a final product with void content near to zero with strong inter-laminar bonding. In reality, it is difficult to fulfill due to multiple phenomena such as porosity rate, residual stresses, degradation happening at the scale of not only the substrate but also the prepreg. Thus the overall AFP process is controlled at multi-scale. These parameters are influenced by the type of raw material used, the removal speed, pressure or temperature fields as discussed in the thesis of V. Le Louët [19].

Mechanisms involved: The characteristics of the matrix and fibers used are decisive for the properties of the final piece. The mechanical strength of the final laminate highly depends on the following factors as discussed in her thesis:

Steps	**Heating**	**Consolidation**	**Cooling**
	Fusion	Contact development	Complete Crystallization
	Degradation Start of void growth	Healing Void compression Beginning of Crystallization	Residual Stresses

Table 4.2: An overview of mechanism during each step of AFP

Processing parameters: The rate of deposition should be controlled as faster deposition could lead to weak bonding during the consolidation step and finally a product with low mechanical strength. The pressure applied to the laminate during consolidation should also be monitored carefully as insufficient pressure increase the growth of void and excess pressure can

cause damage to the fibers. Pressure above 0.4 MPa [21] and below 20 MPa[22] is suitable for proper quality of the final product.

The temperature control of the AFP process not only defines its thermal but also the mechanical behavior of the final laminate. Beyond a sufficient heat input, it is the entire thermal history of the material that must be known and controlled to meet the specifications of manufacture of a laminate. Each step present in the AFP process starting from heating; consolidation parameters such as void growth, intimate contact development, healing, and crystallization are temperature dependent factors. Therefore, in this thesis we focus on the numerical thermal analysis of the tape in an AFP process.

2.4 Literature on thermal modeling of the AFP process:

Experimenting at very fine scales comes with the sensitivity issues of the measuring instrument and requires specific experimental setups. Therefore, in this thesis, a numerical approach is chosen that would have the capability to understand the intrinsic behavior of the tapes during AFP process. There are numerous studies present in the literature that are dedicated to the macroscale thermal study of an AFP process. In the year 1992, Mantell and Springer [23] created a 2D thermochemical model for consolidation, residual stress and bonding during an AFP process. The actual temperature distribution on the top of the ply was not discussed. The heat capacity and thermal conductivity were kept constant before the glass transition temperature. Later in the year 1998, Sarrazin and Springer [24], by assuming uniform heating of the composite, focused their work on the thermochemical and mechanical modeling of the ATL. They also assumed that the specific heat capacity and the thermal conductivity are linearly dependent on temperature. Similarly, most of the research works are based on the strong assumption of uniform heating at the interface with complete absorption of energy where the tapes are acting as a homogenous medium and the maximum temperature is at the top surface [25–29].

Various studies were also conducted on the estimation of the exact energy absorbed by the tape after accounting reflectance from the surface of the fibers. Grove estimated the heat distribution input by accounting the reflectance of the laser heat source at the tape surface. He estimated the surface flux distribution with a 2D ray-tracing pattern on a merely specular surface. In the year 2015, Stokes-Griffin and Compston published two articles. In the first one [30], the effect of reflectance by changing the angle of laser impact on the surface was estimated using an optical ray-tracing model (less than 15% reflective energy until 55° of the angle of incidence of laser). In the second paper [11], a 3D ray-tracing model was developed that captured the anisotropic scattering during the AFP process. They assume the tapes are acting as an equivalent homogeneous surface sized to reproduce the optical behavior of the beam over the composite. The thermal model takes into care the change of thermal properties with temperature. However, there was a strong assumption of perfect contact between the coming prepreg and the substrate that could affect the overall temperature distribution. Barasinski[10] introduced multiple configurations to deal with the thermal contact resistance between the layers due to imperfect

bonding. However, no comparison with the experimental measurements was shown. In the year 2018, Kollmannsberger et al. [31] developed a 2D model to take into consideration all the global parameters such as non-uniform heat input by laser, a thermodynamic model including temperature-dependent material properties, and thermal contact resistance between the layers.

However, what is happening at the scale of single tape was never discussed by any of the research articles. Mostly the surface is assumed to be uniformly heated and the tapes are acting as a homogenous medium. Nevertheless, at the micro-scale, experimentally there is a huge difficulty in predicting the real thermal behavior inside the tape. Direct temperature measurement during the AFP process is often difficult due to the lack of confidence regarding the intrusiveness of the sensor between thin composite tapes (~500µm). In the thesis of Le Louët [19], the research group developed a specific bench aiming to experimentally determine what a prepreg tape did undergo during a deposition in terms of temperature. It was observed that with the classical model assuming tape as a homogenous medium, there was a bad prediction of the maximum temperature reached by the surface, as measured with an infrared camera. AFP being highly dependent on the thermal history of the tapes or prepreg, the exact prediction of the temperature during the process is widely essential or else the quality of the final product can get hampered. Moreover, in the literature, there seems to be no work present that focuses on the real microstructure.

3. Experimental Setup

In the thesis of V. Le Louët [19], an experimental bench was designed to reproduce and characterize the thermal exchanges happening at the scale of one ply to another during the AFP process. The realistic representation of the thermal history not only depends on the heating of the top surface but also on the cooling by the steel bench present at the rear end. The thermal contact resistance between the tape and the substrate highly affects the cooling rate. Thus the objective of her thesis was to observe the various parameters influencing the heating of a composite heated by a laser diode, such as surface temperature rise, flow transmitted to the fold and the tape/tool interface behavior.

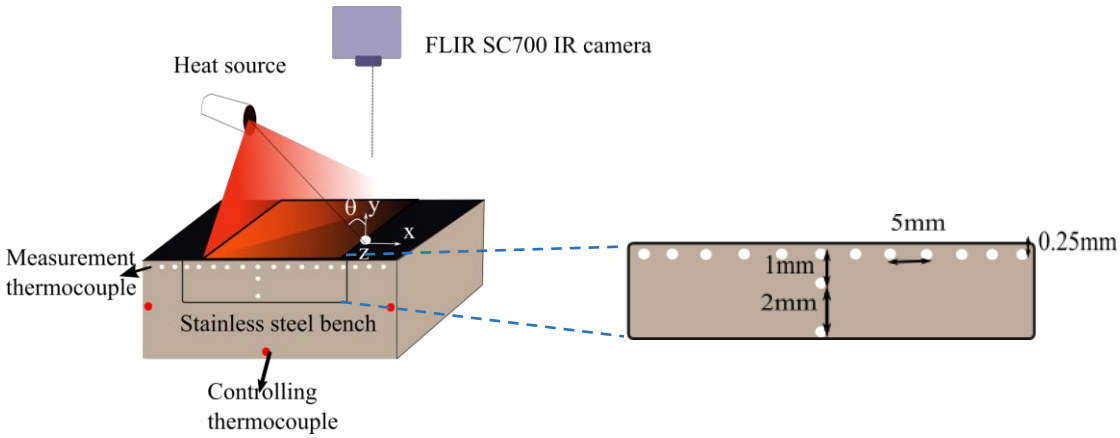


Figure 4.2: Schematic diagram of the experimental setup

Figure 4.2 represents the schematic diagram of the experimental bench. A tape is held on metal support and heated by a laser diode placed at an angle θ. The radiative properties of the tape and the microstructural arrangement of the carbon fibers, decides the surface temperature distribution and the flux that is absorbed. The heat is then passed through the depth of the tape by conduction and then cooled by the contact rear side zones of the tape with the steel bench. Different aspects of the experimental setup are described in the following:

Tape: The materials selected for this study were composed of pre-impregnated unidirectional carbon fibers surrounded by a PEEK (Poly Ether Ether Ketone) polymer matrix. Two types of composite by a different supplier, APC2 Solvay and Suprem^{TM}, were tested with the experimental bench. A detailed description of the material properties are given in the upcoming sections.

Steel Bench: With the objective of a 1D heat flow in the thickness, two identical stainless steel benches of type Z35CD17 (AFNOR) with dimensions 20mm by 6mm were used on the rear side of the tape.

Thermocouples: Multiple thermocouples of type K with diameter 25 µm are placed in the drilled channels on the steel bench near to the tape interface. The end of thermocouple sheath is welded to the metal frame. Two additional coaxial thermocouples were welded at 1.25 mm and 3.25 mm in the center, in order to realize a flux sensor. Three 1mm diameter control thermocouples were placed to measure the bottom and side face temperatures of the steel.

Laser Diode: The laser is driven in power and time by an analog signal between 0 and 10 V to provide a set point between 0 and 100% of the maximum power of the laser equal to 2 kW. The minimum power is set to 10% of the maximum value. A complete characterization of the laser heat source was done in the thesis of Le Louet. The principle of the diode lasers rests on the combination of many individual beams of low density. The integrated laser beam projected on the surface consists of uniformly distributed wavelengths between 900 and 1100 nm. It was estimated that a total heat flux of 1.8 MW.m^{-2} was projected by the laser to the tape [19] at the minimum power of the laser.

Thermal Camera: A FLIR SC700 thermal camera is held perpendicular to the tape with a metal bracket whose position could be adjusted. The temperature is measured by the thermal camera using the emitted radiation (1.5 to 5.1 µm wavelength) which is ultimately related to the temperature of the surface depending on the emissivity of the surface. The emissivity of the material in this wavelength range was measured to be around 0.9. The use of the thermal camera makes it possible to obtain a record of the evolution of the surface temperature rendered in an image. The measurement of temperature was performed by the software Altair. The measurement is made with a lens of 50 mm. The maximum image size is 320 by 240 pixels. The distance between the camera lens and the frame is 51 cm.

3.1 Measurement of Average Top Surface Temperature

Heating tests were carried out on tapes produced by Solvay and Suprem. It was envisaged that the very fast temperature rises at the surface during heating of 25 ms were likely to produce strong thermal gradients in the thickness of the fold that would lead to thermomechanical deformations. Figure 4.3 represents the temperature over time of different points of the illuminated area averaged on a square zone of dimensions 5 x 5 mm^2. Figure 4.3 shows the average temperature measured experimentally for Solvay and Suprem. It appears that at each point the change of slope during cooling takes place at different times, ultimately a different cooling rate for Solvay. Moreover, the maximum temperature reached during heating is also different. Supreme tapes had approximately homogenous behavior in terms of temperature distribution for different points.

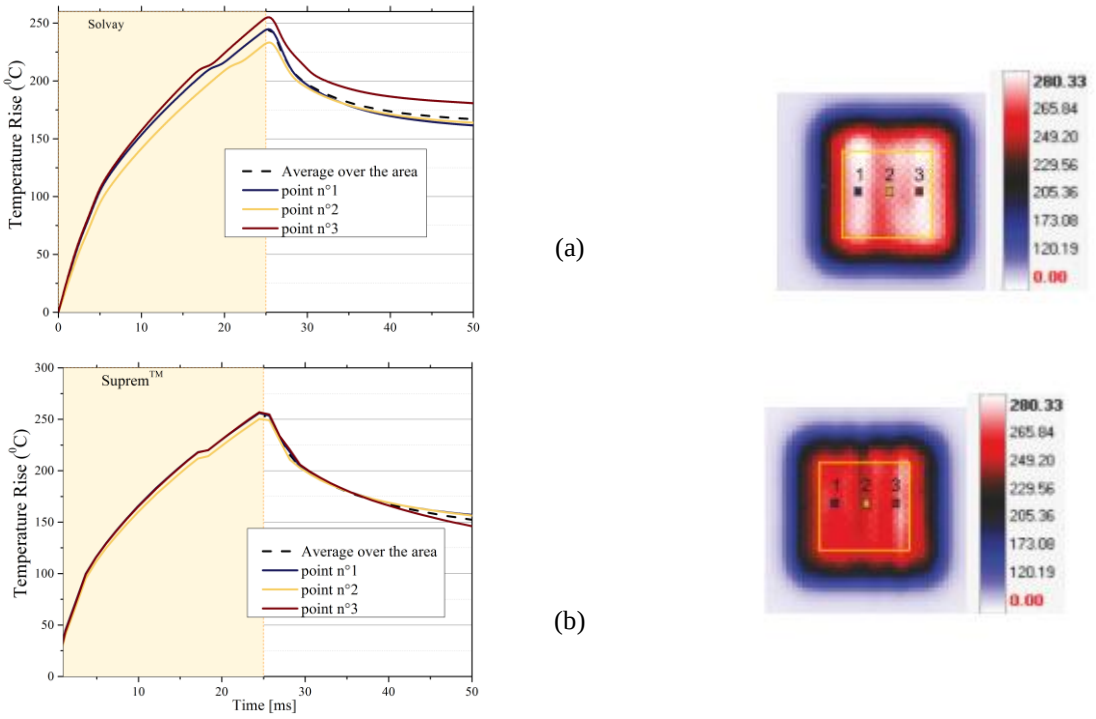


Figure 4.3: Evolution of top surface temperature with time at different points (1,2,3) in a tape (a)Solvay (b) Suprem

4. Micro-scale numerical modelling on the tapes

4.1 Motivations

During the experiments, heating tests were reproduced for multiple samples and it was observed that the thermal response are different for two materials under the same heating condition despite identical chemical and optical properties. The study of surface temperature profiles highlighted the divergence between the homogeneous surface model and measurements by an infrared camera, during heating and the first instants of the cooling phase. The origin of this difference prompts to investigate the mechanisms of absorption of the laser flux on the surface and the microstructure of the folds. In our initial hypothesis, the major difference between the two types of tapes lies in the arrangement of the fibers and the rear side contact quality with the steel bench. Because of the surface roughness and depending on the number of effective points of contact, the heat flow takes preferential paths outside the one-dimensional axis, which is dominated by the boundary shape and by fiber distribution. Thus, the flow lines will converge on fiber-rich contact areas (Figure 4.4).

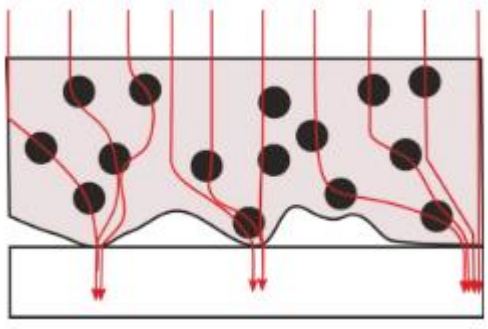


Figure 4.4: Schematic representation of flux transmission along the contact of tape and bench

Therefore in this thesis, the motivation is to study the thermal behavior of the tape, Suprem and Solvay, at microscale during AFP process by numerical modeling in order to check the validity of some physical assumptions about the micro-mechanisms of the heat transfer inside tapes. It would give us the ability to predict the physics happening at the scale of a single tape. The infrared camera could observe the top surface temperature of the tape but understanding the phenomena happening inside the tape is rather difficult, especially regarding the influence of the non-perfect contact between the tape and the steel. Geometries in resemblance with the real micrograph of the tape could help the study of influence of the contacts on overall temperature distribution. Analyzing different microstructure and observing how the arrangement of fiber distribution could affect the overall temperature distribution along the thickness. In the literature, little to no attention was given to the question about the appropriateness of homogenous heat transfer models along the thickness of the tape. This could be answered by solving the transient heat transfer of the tape during the AFP process at the microscale.

4.2 Image Processing

Preliminary objective was to form a mesh for the finite element analysis with a maximum resemblance with the real microstructure. This could be approached by taking a microscopic images of the different section of tapes for proceeding image analysis for generating mesh. The two tapes were cut into small pieces along the perpendicular direction to the fiber. This was fixed in vertical position with the help of adhesive in a small container and then the liquid resin was poured in the container until the top surface of the tapes are covered in the resin (Figure 4.5 (a)). After the resin was dried, the support was removed from the container and then polished with different grade of sand paper starting from a particle size of 120 and then slowly going until 1200 in order to get the clear sample for taking images under microscope (Figure 4.5 (b)).

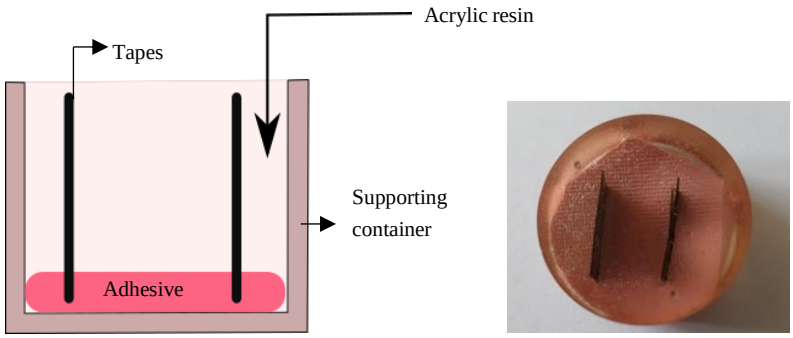
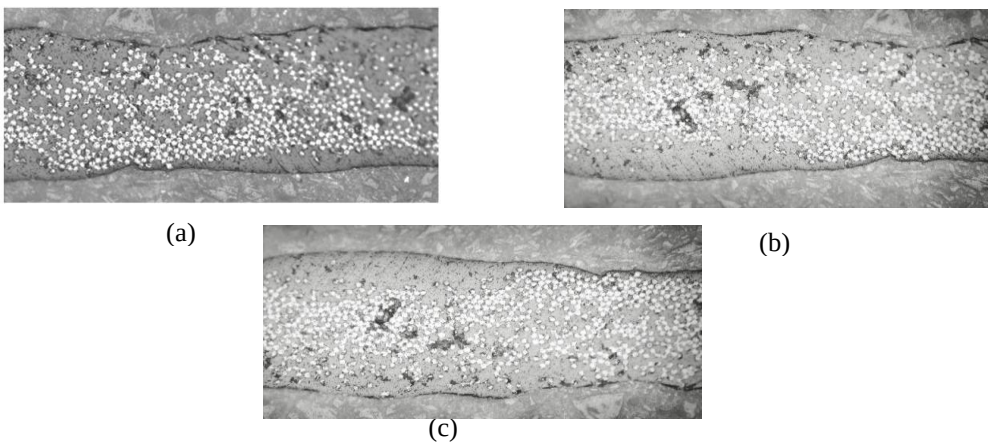


Figure 4.5: (a) Preparation of the sample (b) Sample of Solvay and Supreme for optical microscope visualization

4.2.1 Microstructures of Solvay and Suprem tapes

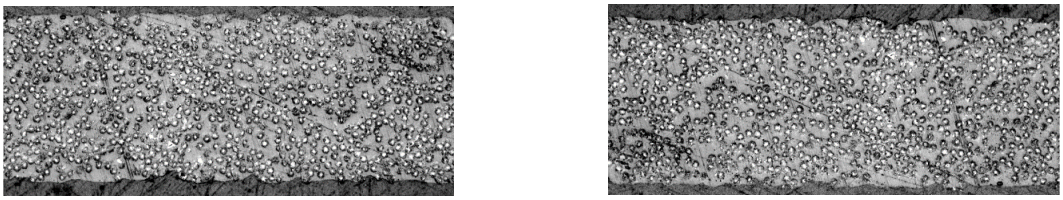
Different micrographs (Figure 4.6, 4.7) were obtained by scanning the tapes with the help of an Optical Microscope (OLYMPUS BX61) at 20X zoom. It can be observed from the microstructures that for Solvay the arrangements of fibers are highly inhomogeneous. The fibers were packed in a way that leaves areas rich in the matrix with no fiber in the thickness. Porosities can also be observed in some places but they won't be considered here for modeling. Contrary to the Solvay, Suprem tapes are rather homogenous in the distribution of the fibers in the matrix. Clearly, the two types of plies have very different microstructural arrangements for an identical AS4 carbon fiber content.



(a) (b)

(c)

Figure 4.6: Microstructure of different sections of the Solvay tape (a) Solvay 1 (b) Solvay 2 (c) Solvay 3



(a) (b)

Figure 4.7: Microstructure of different sections of the Suprem tape (a) Suprem 1 (b) Suprem 2

4.2.2 Geometrical modeling with Hough Transform

The geometries were generated from the microstructures by initially getting the information about the center of each fiber. A Matlab code transforms the micrograph into binary images and with the help of Hough transform, it segments the circles from the outside plane. In 1962, Paul Hough [32] developed this algorithm to detect geometric features like straight lines in digital images that is widely used in the sector of computer visions. Later it was used to spot higher order analytical shapes such as circle or ellipse [33][34][32]. In the thesis of M. Thomas[35], the Hough's transform portrayed higher efficiency of detection in comparison to different morphological tools. The Hough transform can be a powerful tool. Specifying the radii range of fibers, it is then possible to detect the individual fibers on a grayscale or binary image. One can find on freeware Matlab routines present in the central file exchange website that uses Hough transform to detect circular shapes in a grayscale image.



Figure 4.8: Hough's algorithm over coins

Figure 4.8 shows the example of Hough's transformation over bunch of coins and detecting the edges of the coins. These images had a quite defined edges therefore exact detection was possible. In the microstructure of the tape, there were multiple regions with dust or improper matrix impregnation that results in loss in detection of certain fiber as shown in Figure 4.9. However, this algorithm can detect the fibers that are not exactly circular and even in the area with blurry images and has shown low sensitivity to noise as compared to other detection techniques [35]. Therefore Hough's transformation was used for the fiber center detection of the microstructures. It ultimately gave the pixel position for the center of the fibers that are present in the tape. The algorithm for circle detection is detailed in the Appendix.

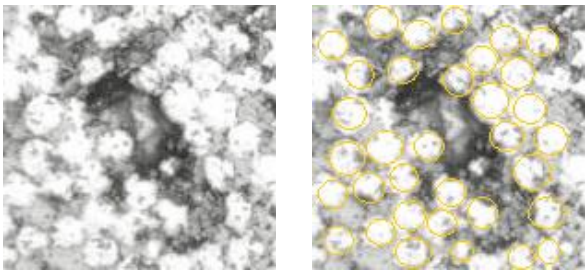
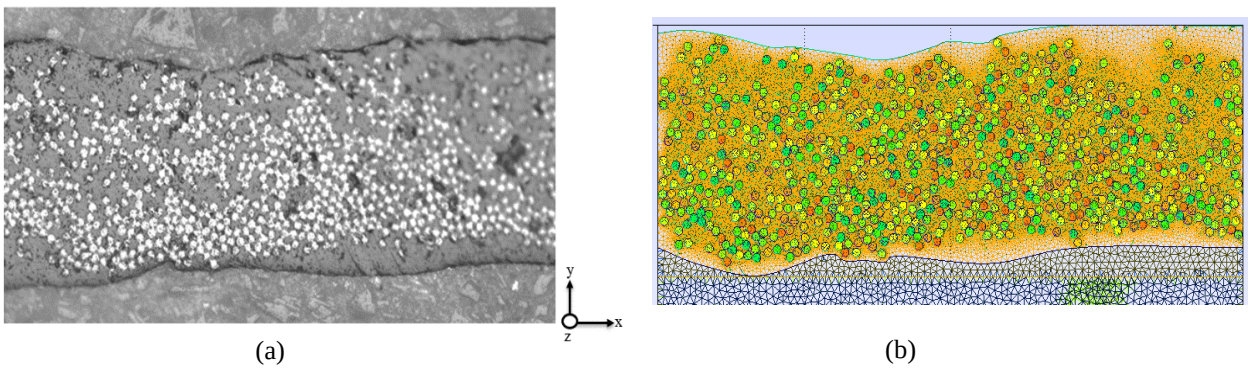


Figure 4.9: Hough's algorithm over a small section of the tape.

After the pixels have been stored, the data is converted to the Cartesian coordinate system. For a 20x zoom, a multiplication factor of 0.1693e-6 to x and y positions gives us the x and y coordinates for the fiber center. For the detection of the edges of the microstructure ImageJ is used and the coordinates of the boundaries are also stored. Then a Matlab code was generated which can create the .geo file for Gmsh from the coordinates of the fibers and the boundaries. In that code one function was added that could generate the region of air and steel on the rear side of the tape. The region of contact depends on the boundaries of each tape. A detailed algorithm is presented in the Appendix.

4.2.3 Meshing for FEM model

Initially, geometries and meshes are created by the FEM meshing tool Gmsh with Frontal 2D and 3D algorithm. In our case, the Solvay and Suprem mesh consists of surface element as 3 node triangle and volume element as 4 node tetrahedron. This mesh is later used for detection of the elements of the fibers surface that are getting impacted by the laser. It is based on a simple optical model that finds the elements in direct exposure to the perpendicular hitting laser, each of these elements being given a different physical tag or region name. The tagged elements later can act as a heat source (Q_{Laser}) for the 25ms of heating in the solver of FreeFem++. The algorithm for element detection is presented in the Appendix.



(a) (b)

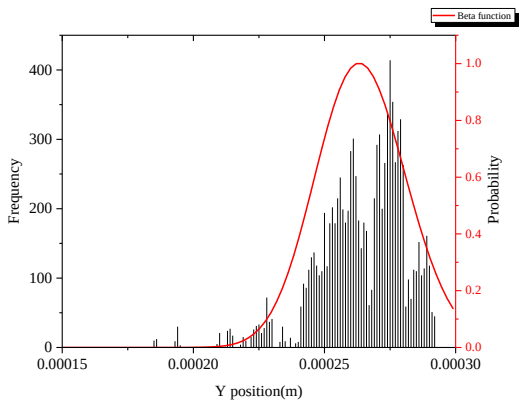
Figure 4.10: (a) Microstructure of Solvay 1 (b) Corresponding mesh

5. Heat source distribution

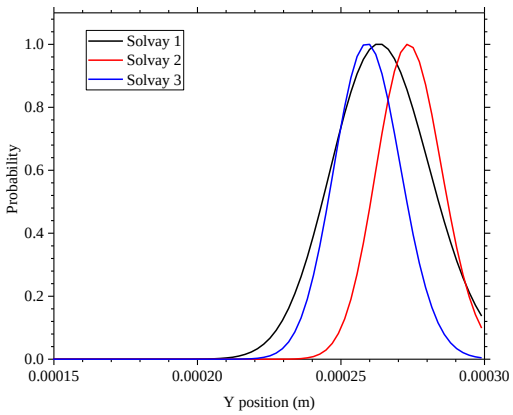
Once the meshing is done, the first point of interest is exact region of absorption of heat over the scattered fiber in the tape. The heat source distribution along the height of the microstructures are determined by knowing the frequency or number of elements that are getting impacted by the laser at a particular height (y) of the tape. This can help in understanding the heat transfer inside the volume of the microstructure. Figure 4.11(a) shows the frequency distribution of Solvay 1. It was observed that due to the presence of certain thickness of PEEK matrix alone at the top and disparity of the fibers along the volume directed to maximum absorption of heat at a certain depth below the surface. This frequency distribution was fitted by the Matlab fitting tool in order to get a function that can perfectly describe the laser absorption zone. Apparently, the fitting with a beta function better defines the heat source distribution. This beta function is defined by the following integral term:

$$\beta(x,y) = \int_0^1 t^{\beta_x - 1}(1-t)^{\beta_y - 1} \tag{4.1}$$

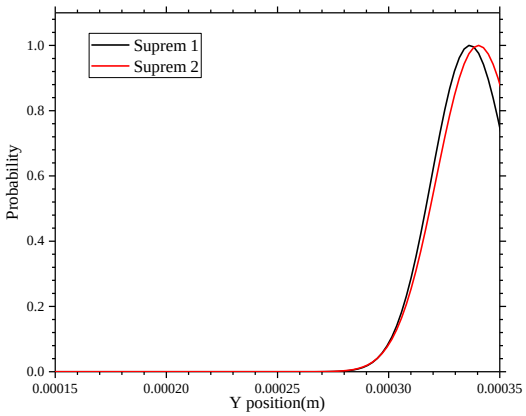
where β_x and β_y can be real number that defines the shape of this continuous function. Similarly, different microstructures for Solvay were tested and is shown in Figure 4.11(b). It was observed that the heat source distribution could change significantly depending on the distribution of the fibers with maximum heat absorption around 25-50µm inside the tape. This makes the assumption of the tape as homogenous media quite questionable as that would lead to maximum absorption of laser heat on the top surface. Figure 4.11(c) shows the distribution for a Suprem tape and it can be seen that the maximum heat absorption is near to the edge of the top surface (~8µm inside). Even from our initial observation of the microstructure, it was observed that the Suprem tape has a rather homogenous and dense distribution of fibers throughout the microstructure. Thus making a similar heat source distribution for a different section of the tape. In order to better understand the thermal behavior of a tape at micro scale, a temperature distribution study along the depth would be necessary and thus a detailed solving of the heat transfer equation.



(a)



(b)



(c)

Sample	β_x	β_y
Solvay 1	235	$9\ 10^5$
Solvay 2	269	$1.4\ 10^6$
Solvay 3	757	$2.3\ 10^6$
Suprem 1	295	$9.8\ 10^5$
Suprem 2	340	$9.9\ 10^5$

(d)

Figure 4.11: Heat source distribution for different microstructures: (a) Solvay 1, frequency of absorption and fitting with beta function, (b) Different Solvay microstructure, (c) Suprem, (d) values of β_x and β_y for different beta function fitting

6. Numerical model

As discussed previously, this thesis aims in solving the transient heat transfer problem of projected laser on the single tape. Mesh corresponding to the microscopic images of the tape was generated (section 5.3). The fiber surfaces impacted by the laser acts as a heating source and the distribution of this source was an important criterion to determine the behavior of the tapes during heating. The temperature distribution of the tape was calculated by solving the transient problem through FEM and average temperature at a particular height was calculated by an averaging scheme described in section (section 6.2).

Figure 4.12 shows a schematic diagram for the basic idea of the model for tapes with direct laser heating, resistance due to imperfect contact by imposing presence of air and cooling by the steel bench on the rear side.

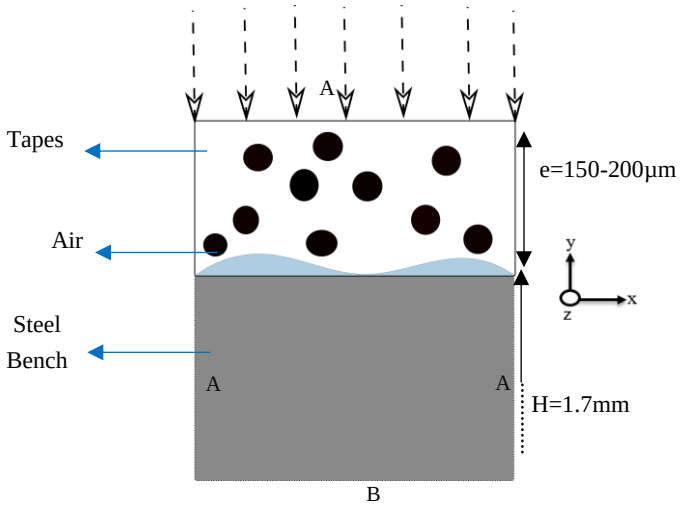


Figure 4.12: Schematic representation of heating of tape

The laser beam at $\theta = 0$ is assumed to be coming perpendicular to the surface with a uniform flux of 1.8MW.m^{-2} (Q_{Laser}) [19]. The matrix is transparent to the laser wavelength and fibers are assumed to have a uniform absorption coefficient of 90% of the laser heating. This approach does not account for the reflectivity from the fiber surface with the incidence angle nor the internal reflections between fibers. The air gap and non-smooth surface between the tape and steel act as the thermal contact resistance by giving added roughness. No additional contact resistance is added at the level of contact between the polymer and the steel. Consider a composite ply of thickness *e* kept in contact with the surface of the steel frame of height *H*. The transient heat transfer equation (4.2) is solved for temperature T using finite element method with the boundary conditions given in (4.3). ρC_p is the volumetric heat capacity, and k is the thermal conductivity.

$$\rho C_p \frac{\partial T}{\partial t} - \boldsymbol{\nabla}.(k\boldsymbol{\nabla}T) = Q_{Laser} \tag{4.2}$$

$$\begin{cases} Top\ surface:\ 'A', -k\boldsymbol{\nabla}T = \mathbf{0} \\ Lower\ surface\ 'B': T = 293K \\ Initial\ condition: T(\boldsymbol{x}, 0) = 293K \end{cases} \tag{4.3}$$

FreeFem++ is used to solve this PDE. This equation is transformed into its weak form, assembled and then solved by the standard generalized minimum residual iterative method.

6.1 Material Properties

The tapes are composed of pre-impregnated unidirectional carbon fibers AS4, surrounded by a polymer matrix PEEK (Poly Ether Ether Ketone). Although there is uncertainty in the diameter of AS4 carbon fibers along the length, as shown in chapter 1, for simplicity a constant diameter of 6.5µm is chosen for the numerical simulation. For the microstructural analysis, it is important to consider the thermal anisotropic nature of the fiber. The value of the thermal conductivity of each component was obtained from the literature. In the article of Kollmansberger [31], the measured heat capacity of the carbon fiber are rather constant for temperature up to 470 K.

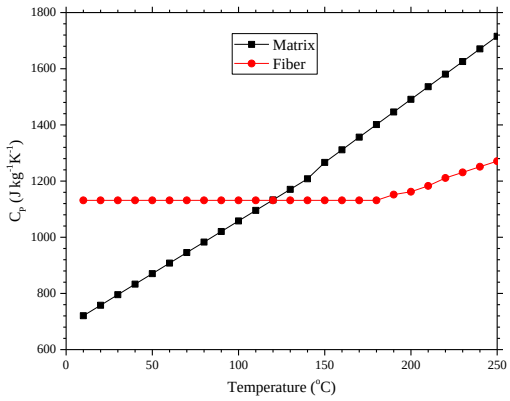


Figure 4.13: Variation of specific heat of the matrix and fiber with temperature.

The heat capacity of the matrix was measured with the help of Differential Scanning Calorimetry in the thesis of Le Louët. A cycle at a heating speed of 5K/min was chosen for the measurement of heat capacity as a function of temperature. Figure 4.13 shows the linear interpolation of the heat capacity of the PEEK 150G matrix measured by DSC. Table 4.3 shows the material properties such as thermal conductivity, heat capacity and density of the fibers and matrix along with the air present at the interface and the stainless steel bench of type AFNOR Z35CD17. The data of each component are obtained either from literature or data sheets of the provider.

Thermal Properties	**Fiber (AS4)**	**Matrix (PEEK)** [19]	**Air**[36]	**Steel** [19]
k(W m^{-1}K^{-1})	6.1 Longitudinal [19] 1.19 Transversal	0.22	0.028	23.5
C_p(J kg^{-1}K^{-1})	1100 [31]	683+3.75*T (T<143°C) 593+4.49*T (T>143°C)	1006	480
ρ(kg m^{-3})	1790 [37]	1320	1.1	7700

Table 4.3: Thermal properties implemented in numerical model for fiber, matrix, air and steel

6.2 Averaging technique for temperature measurement by numerical model

One of the issues of the numerical study is to calculate averages (temperature, heat flux) at one surface or at a particular height *y* of the sample. Just like the homogenization approach discussed in chapter 4, the idea is here to analyze in a simple manner the averaged 1D behavior in the transverse direction of tapes. Doing so, one expects to be able to study the homogenized continuous thermal behavior of the tapes in the process conditions and to give the way towards a continuous modeling, probably including the microstructural effects remarked previously.

Surface-averages calculation is possible by the open-source visualization tool Paraview. However, its applicability is limited to the surface at a particular height or by manually changing the coordinate *y*. Such an approach would be unreasonably time consuming. The storage of temperature files as vtk files (~145mb) for each time step is also challenging in terms of memory. Fortunately, the FreeFem++ tool itself provides a quite efficient solution for this problem, making use of a grid technique for the averaging. Figure 4.14 shows an example of a circular cross-section and how the data at each grid point in the circular cross-section could be collected. The mean of all the data of *n* number of nodes present inside the circle gives the average temperature at the surface.

$$T_{avg} = \left(\sum_{i=1}^{n} T_i \right) / n \tag{4.4}$$

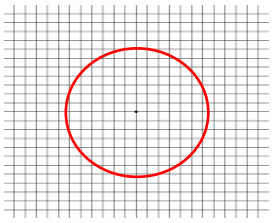


Figure 4.14: Circular cross section with grids.

As visible from Eq.4.4, this approach is not a proper average in the sense of the finite elements method, but we take advantage here of the regularity in the grid where temperatures are simply interpolated by the FreeFem++ basic functions depending on the solution of the temperature. A comparison of the average temperature estimation from Paraview and direct grid technique was done on a 3D cube (1m X 1m X 1m) (Figure 4.15(a)). It can be seen from the Figure 4.15(b) that the average temperature measured at different *y* by our grid technique is highly consistent with the Paraview results with a condition of sufficient density of grids. However, it's also essential to make sure that the grid density is high enough for the average temperature to remain independent of it. This was verified by applying FEM model over a Solvay mesh and then using grid technique to estimate the average temperature along the depth. Different grid density starting from 20 X 20 to 250 X 250 nodes were analyzed. It can be seen that beyond 100 X 100, the average temperature does not change further by increasing the grid density. It is also in excellent comparison with the results from Paraview (Figure 4.15(c)). This finally validates the use of the so-called grid technique for the rest of the results discussed thereafter.

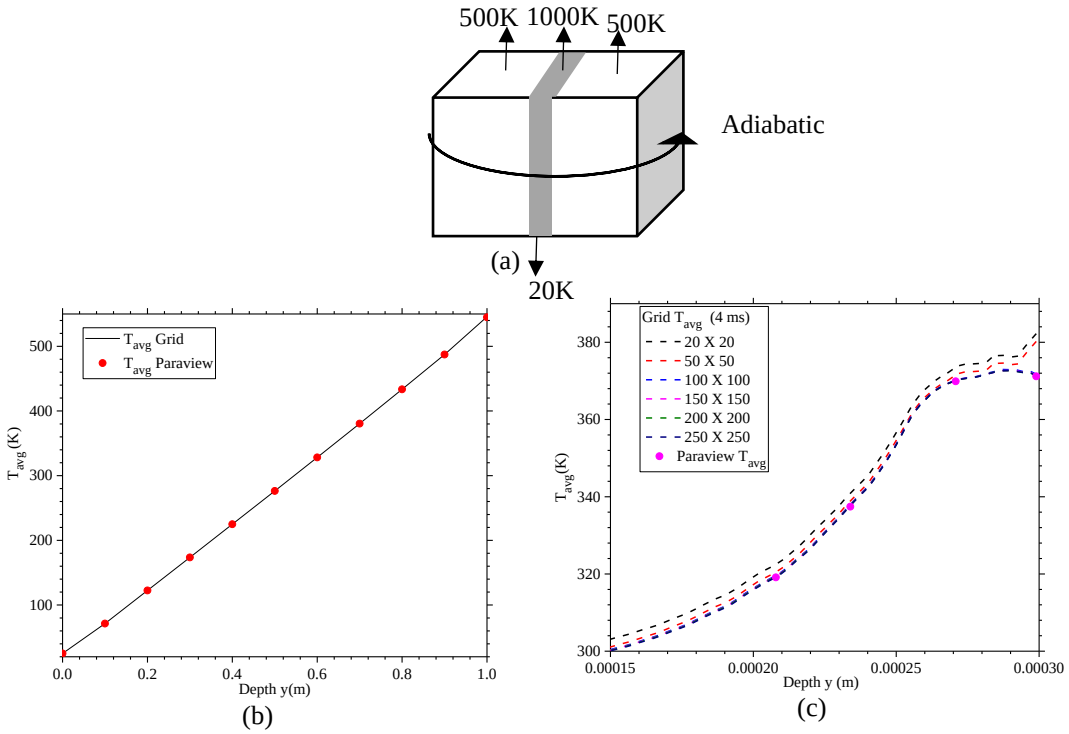
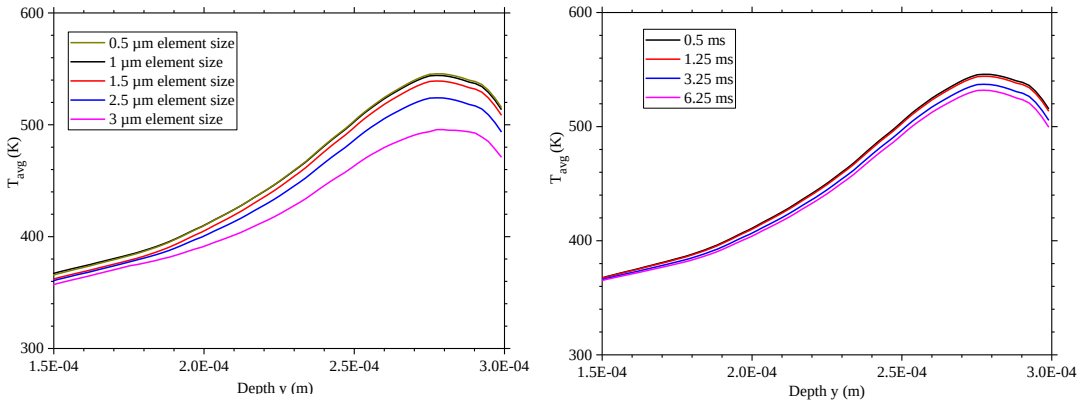


Figure 4.15: (a) Cubical geometry (b) Average temperature by Paraview and Grid technique (c) Average temperature on Solvay1 by Grid technique

6.2 Mesh and Time Convergence

The finite element method is chosen in order to solve the various problems posed. The searched fields are thus discretized spatially. It is the same for the time scale. Before exploiting the global model, it is necessary to check the convergence of these two discretizations. Convergence in mesh is verified by performing simulations using different meshes, from coarser to finer. In this case, the size of the element edge was the controlling parameter as it varied from 0.5µm (higher mesh density) to 3µm (lower mesh density) for different meshes (Figure 4.16). The average temperature along the depth was estimated for different mesh size by solving the numerical model for heat transfer problem over the tapes in AFP. It was concluded that the element edge size of 1µm is sufficient to obtain an average temperature that doesn't change with further densifying the mesh with smaller elements. On the contrary, further decreasing the element size would lead to increase in the computational cost of overall simulation. In view of these results we will take, for the rest of the calculations, the discretization of the mesh with 1µm of element edge size.

For the convergence of time, we performed several simulations on the mesh (1µm element size) with multiple time steps (0.5 – 6.25 ms) for solving the average temperature after 25ms of heating. From these results, it is observed that the time step has marginal influence on the results and 1ms of time step is sufficient to limit the error in average temperature estimation.



(a) (b)

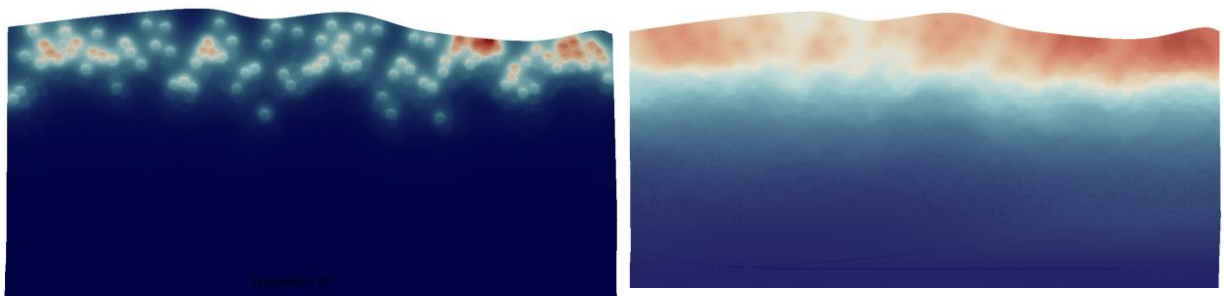
Figure 4.16: (a) Time convergence (b) Mesh convergence by estimation of Average temperature at 25ms

7. Results by numerical modeling

In this section, our FreeFem++ code was used to solve the transient heat equation (section 6) for different meshes (section 4.2) in resemblance to the microstructures presented above. The visualization of heat flow diagram at different time steps is presented along with the heat flux streamlines to understand how intimate contact can influence the overall heat flow in the tape. The influence of the RTC on the average temperature estimation is also shown. The calculated average temperature is compared with the experimental results.

7.1 Heat flow by µ-calculation

Figure 4.17 represents the temperature distribution in Solvay tape at different time steps that could help in the visualization of what is happening at the micro scale. During initial heating by laser, the fibers that are facing the laser are getting heated until 25 ms and then the natural cooling begins. The fiber distribution in the microstructure is the controlling parameter as the fibers have nearly 10 times the thermal conductivity of the matrix. Figure 4.17(a) shows the impact of the laser at the beginning of the heating phase (0.5ms). Later the heat is diffusing throughout the tape depending on the fiber distribution as it can be seen from Figure 4.17(c) that right side has a higher temperature due to denser fiber fraction. Figure 4.17(d) shows the cooling at 50ms due to the steel bench present at the rear side. Figure 4.18 shows the streamlines of heat flux in y direction (along the depth) showing the dominating direction of the heat flow at different time steps. The stream lines were generated using stream tracer function present in Paraview. As predicted in the initial hypothesis, there is a constriction of heat flow which is mainly dominated by the intimate contact and, in less significant way, by the fibers distribution. The constriction of the streamlines at the rear side confirms the presence of the 2D heat flow as the streamlines are not straight. Instead the streamlines goes through a preferential path that is dominated by the presence of fibers in proximity with each other towards the contact point. There is also a greater influence of air present in the contact zone. For initial time period, the heat flux contribution at the constriction zone was less than 2% than the maximum heat flux present on the top. However with increasing time especially after 30ms, the effect of heat flux at constriction zone is influencing the cooling of the top surface of the tape predominantly.



(a) (b)

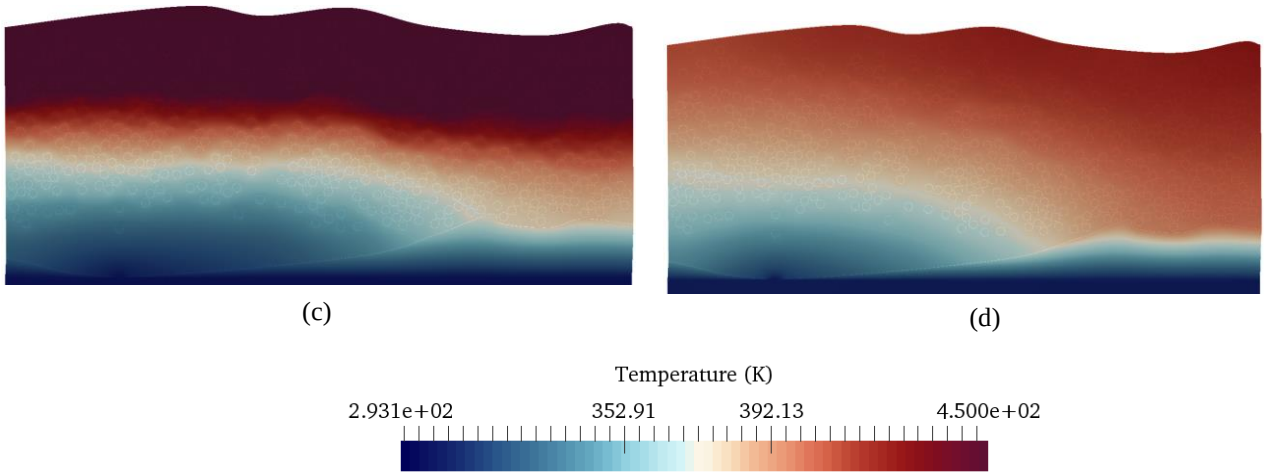


Figure 4.17: Temperature and Heat flow in Solvay 2 for (a) 0.5ms (b) 15ms (c) 25ms (d) 50ms (e) Temperature scale

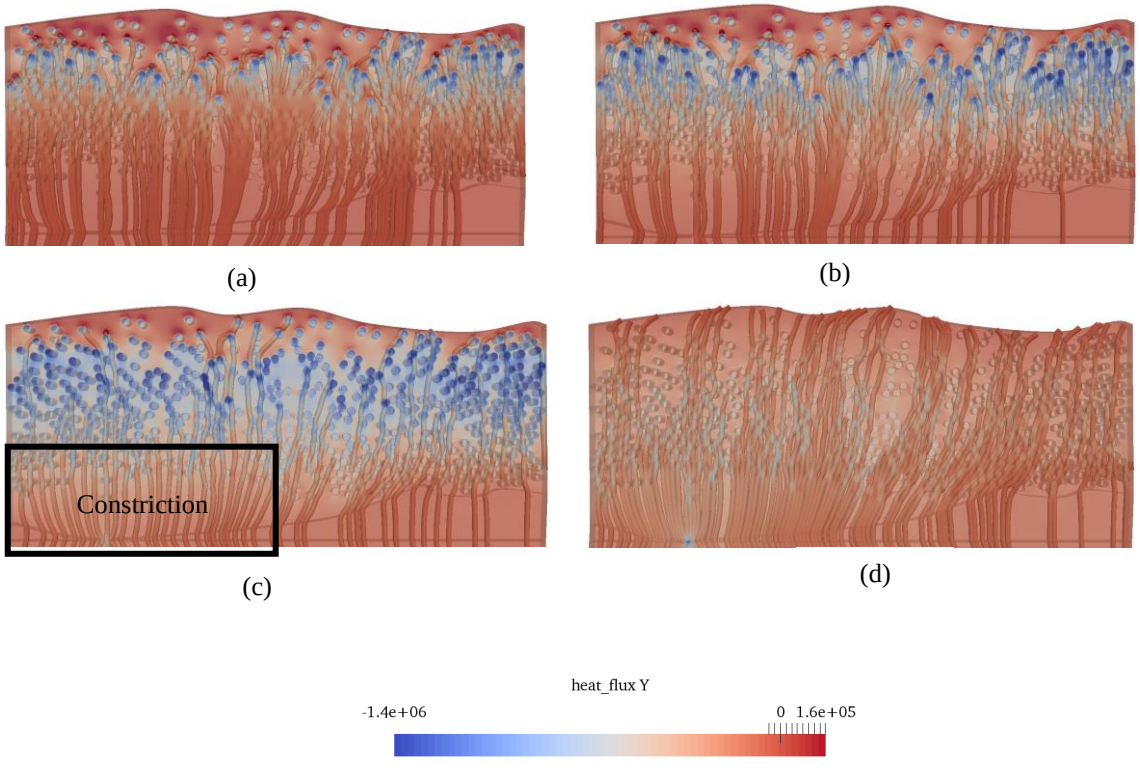


Figure 4.18: Flux lines at different time steps (a) 5ms (b) 10ms (c) 25ms (d) 40ms (e) flux scale for the above figures

7.2 Temperature variation along the height

The difficulty of the AFP process is the measurement of the volume temperature distribution inside the tape due to its small size. This is numerically possible by the measurement of average temperature at a particular height *y* and then calculating the evolution of the temperature along the height. The average temperature is measured based on the grid technique at a particular height *y* (section 6.2). Figure 4.19(a) shows the average temperature as a function of height (y) of the tape for different microstructures of Solvay tape. It can be seen that the maximum temperature is in little depths inside the surface (~25µm). This is contrary to the assumption of homogenous behavior of the tape leading to the maximum temperature located at the surface as widely used in the literature for AFP process[11][8]. It should also be noted that the speed of change in temperature for Solvay 3 is higher than Solvay 2 as the tape becomes in contact with the steel. This is due to the presence of the layer of matrix in Solvay 2 that is resisting the heat diffusion. The Solvay 3 has more fiber density near the rear side thus the diffusion of heat is faster. Moreover, the depth of the maximum temperature varies depending on the microstructure distribution that also affects the heat source distribution. Figure 4.19 (b) presents the temperature distribution for Suprem tape and it can be seen that although the maximum temperature is very close to the surface temperature. The microstructure is much more homogeneous therefore the temperature distribution is similar for both samples.

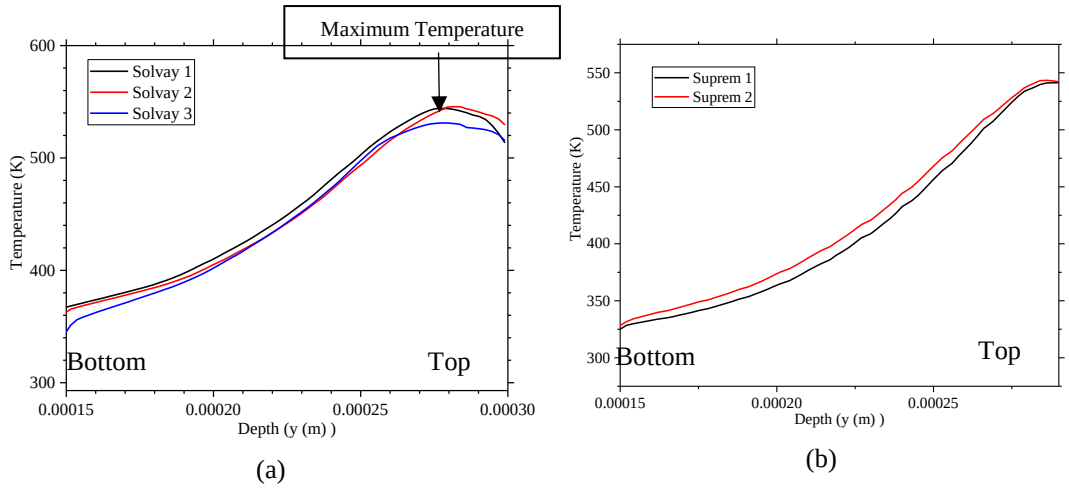


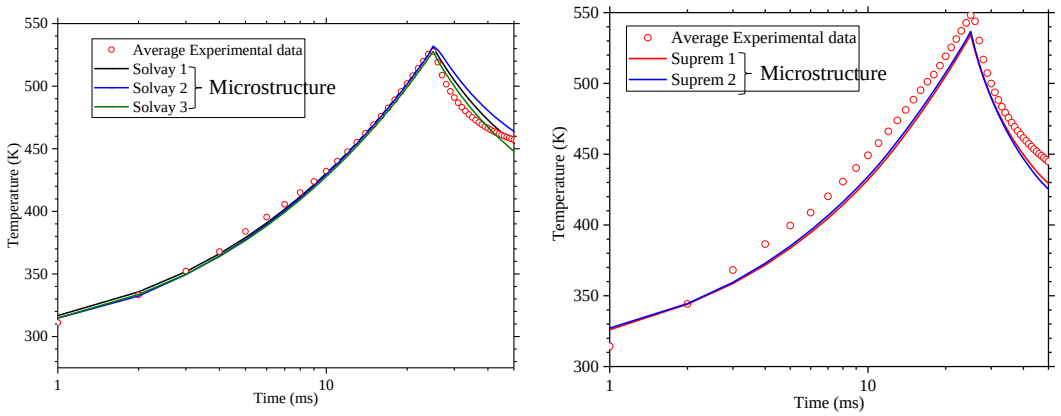
Figure 4.19: Average temperature distribution along y at 25 ms (a) Solvay (b) Suprem

7.3 Temperature variation of the top surface with time

In this section, the temperature change observed by the infrared camera during experiments is compared with the surface temperature obtained by the numerical model. Figure 4.20(a) shows the temperature of the tape surface for a time period of 50 ms for different recorded microstructures of Solvay tape. For the heating time of 25 ms, there is an excellent agreement with the experimental results for each microstructure. This strongly confirms our physical assumptions about the mechanisms of heating in prepreg tapes. However, the cooling rate is still slower for the numerical simulations in comparison to the experimental measurements. This could be due to the fact that during the heating time, the temperature is dominated by laser heating. When laser heating is stopped, rest physical constraint such as volume fraction, fiber distribution are also playing an important role. Moreover, during the image analysis in this thesis there was a loss of certain fibers. Therefore, the penetration of laser heating was deeper in the volume leading to the slower cooling in the tape. Figure 4.20(b) shows the temperature change for the Suprem tape. It was observed that the surface temperature after 25ms of heating of the Suprem tapes is higher than the Solvay. It was because in Suprem tapes the absorption of the heat is closer to the surface, due to the uniform distribution of fibers.

Furthermore, it is important to see that the temperature of the top surface is approximately 260°C in comparison with the bench temperature at 20°C. The thermal diffusivity of the material in the thickness being small, the temperature difference between the two faces of the tape is important as it would result in a high thermal gradient. The thermal state disparity between the lower and upper faces is likely to induce thermomechanical deformations and detachment of the fold during heating. This phenomenon was observed experimentally by Le Louët, but was checked to be maximum before reaching the maximum temperature.

Figure 4.20 (c) (d) shows the normalized representation of temperature up to 50ms. It can be observed that with Solvay tape, the beginning of cooling is yet faster than the numerical. However with the Suprem tape there is a good agreement can be observed between numerical and experimental.



(a) (b)

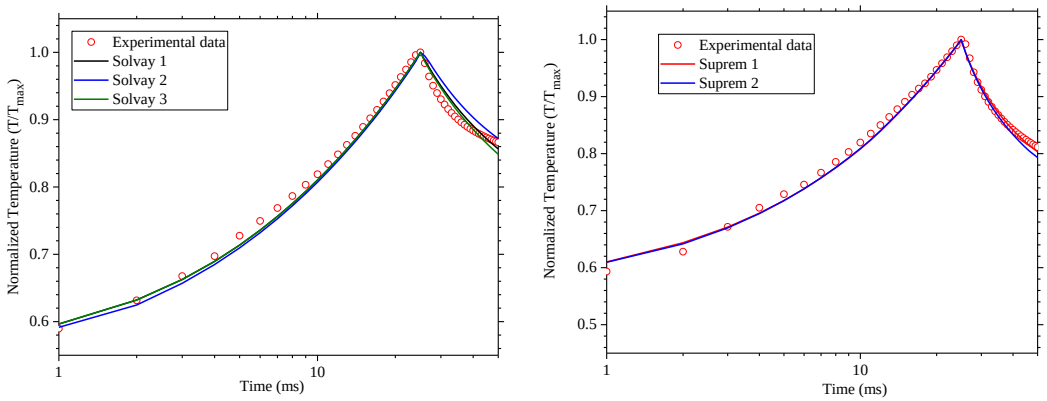


Figure 4.20: Comparison of average temperature of the top surface with experimental readings by the Infrared camera (a) Solvay (b) Suprem. Normalized temperature for (a) Solvay (d) Suprem

7.4 Influence of rear face contact on temperature measurement on the tops surface

The influence of non-perfect contact was evident in the flux lines distribution in Figure 4.19. However, it is necessary to analyze how variation in contact would influence the average surface temperature estimation, especially in Solvay tapes as the microstructure suggests huge change in the rear contact zone. Figure 4.21 represents the average temperature estimated by the numerical model for a different type of contact over the same microstructure. Figure 4.21(a) shows different contact type established on the increased gap (2-10µm) between the steel and tape as compared to what was present based on real microstructure. It can be observed that for a time period of 50 ms, there is no significant change in the average temperature apart from a slight change in the maximum temperature at 25ms (<4%). However, a huge influence could be observed in the prediction of cooling rate after 50ms. It can be due to the reason that after 50 ms, the forward face temperature is affected by backside heat transfer and cools slowly. Figure 4.21(b) presents the influence of increasing the number of contact points as compared to the real case of micrograph. However with the increasing contact point has less influence on the overall top surface temperature.

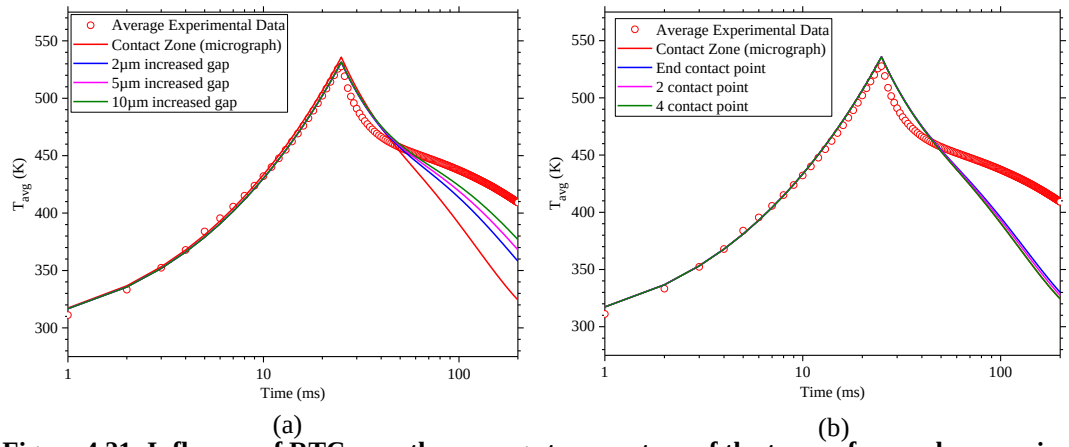
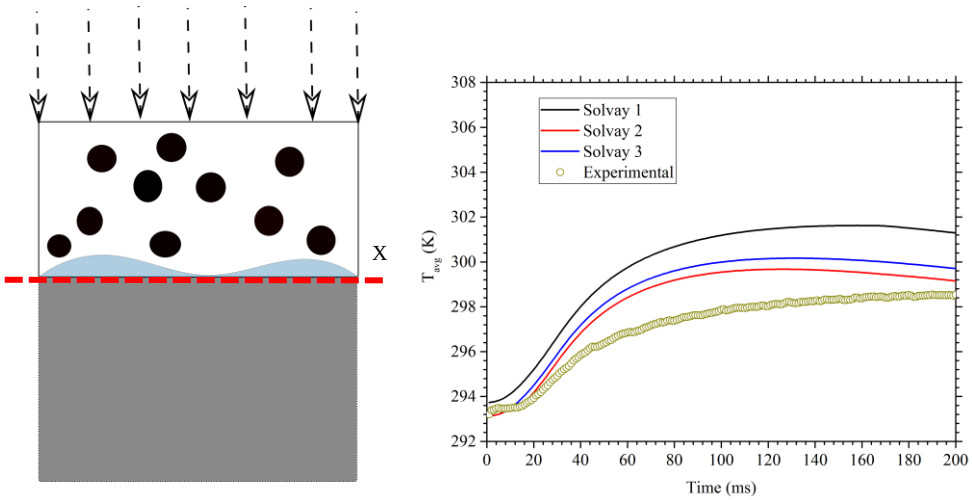


Figure 4.21: Influence of RTC over the average temperature of the top surface and comparison with the experimental readings by the Infrared camera

The experiments also measured the temperature at the steel bench present just near the contact with the tape. The three thermocouples were placed in steel at different length of 0.25mm 1.25mm and 3.25mm as shown in Figure 4.2. By solving the inverse problem, the temperature as well as the heat flux in the steel just near to the rear side of the tape was retrieved experimentally. Figure 4.22(a) shows its comparison with the numerical simulation results of the average temperature on the region in steel present just near the rear side of the tape at X (Figure 4.22(b)) for different microstructure. It can be seen that the temperature on the rear side is in maximum difference of 4K from the experimental value. It is important to note that the temperature measured differs depending on the microstructure. For example, Solvay 1 is heating more as compared to the other microstructure due to the presence of high number of fibers near to the rear side and lesser zone with just matrix. From this, it can be seen that the temperature on the rear side is influenced by the type of contact and also on the distribution of the fibers near the contact zone.



(a) (b)

Figure 4.22: (a) Schematic diagram of the zone where average temperature is measured (b) Average temperature near the contact zone with time

9. Partial Conclusion

The objective of this study was to understand the thermal behavior of tape at microscale after a short exposition to a high density laser on its surface. Experimental measurement at this small scale is intrinsically difficult due to the sensitivity of the measuring instrument. Therefore, a 3D thermal model was developed to better understand the different parameters involved that can influence the tapes heated by a laser source. Through this numerical study, different microstructures of Solvay tape and Suprem tape were tested in the AFP process. Meshes in resemblance to the multiple microstructures of Solvay and Suprem were generated using Hough's algorithm in Matlab. The zones impacted by the laser were tagged as the heat source region by a similar ray tracing technique with the assumption of no reflection. During the image analysis there was a loss of fiber volume fraction due to the lack of higher quality of micrograph.

The heat source distribution of each microstructure was presented. It was observed that the scattering of the fiber position can highly influence the thickness of the tape with maximum heat absorption. Moreover, the width of this source distribution also depends on the type of microstructure, for example for Solvay the heat source is relatively sparse in comparison with the Supreme tape. It is important to note that in the Suprem tape, the heat source distribution is more or less similar due to its homogenous fiber distribution. Through numerical simulation, it was also observed that the heat flux lines go through a preferential path outside the one-dimensional axis depending on the point of contact of the tape with the steel.

Furthermore, the temperature distribution along the thickness of the tape showed that the tape does not follow the assumption of a homogeneous medium, as mentioned in multiple researches. This inhomogeneity leads to the presence of maximum temperature at certain depth inside the tape depending on the type of microstructure. It can also be observed that the presence of a wide matrix region, in case of Solvay, on the top surface or bottom can highly influence the heating or cooling rate. This is due to the fact that the matrix layer increases the capacitive effects inside the fibrous medium.

During the experiments, the tape was heated by laser for 25 ms and then cooled naturally. The average temperature observed by the infrared camera was thus compared to the numerical result of surface temperature. In the case of Solvay tapes, the temperature predicted by the numerical model during the heating is in good agreement for all types of microstructure. On the contrary, while cooling, initially the cooling is faster than the numerical result for 50 ms but later experimentally the cooling is slower. Additionally, the cooling rate is changing due to the higher differences in Solvay tapes microstructures. The Solvay tape has varied contact zones from one microstructure to another. Similarly, for the Suprem tapes, the temperature estimated by numerical model showed less heating than the experimental one. Certain microstructural effects, such as fiber distribution, matrix layer, intimate contact zone, the volume fraction of the fibers, can be the reason for this discrepancy. Moreover, the reflection is also neglected in the current tests as in reality the experiments were done with laser heating at an angle of 10° from the vertical

position. The inter-reflection can affect the overall heat source distribution, thus influencing the overall temperature distribution. All these factors lead to the non-full quantification of the real problem. This can be a part of future perspective where a more sophisticated images or overall image analysis approach could be selected for countering the microstructural effects. Additionally, a complete thermal model encountering the reflection and inter-reflection could improve the current model further.

References

[1] Frketic J, Dickens T and Ramakrishnan S 2017 Automated manufacturing and processing of fiber-reinforced polymer (FRP) composites: An additive review of contemporary and modern techniques for advanced materials manufacturing *Addit. Manuf.* **14** 69–86

[2] Skinner M L 2006 Trends, advances and innovations in filament winding *Reinf. Plast.* **50** 28–33

[3] Beakou A, Cano M, Le Cam J B and Verney V 2011 Modelling slit tape buckling during automated prepreg manufacturing: A local approach *Compos. Struct.* **93** 2628–35

[4] Le Louët V, Rousseau B, Le Corre S, Boyard N, Tardif X, Delmas J and Delaunay D 2017 Directional spectral reflectivity measurements of a carbon fibre reinforced composite up to 450 °C *Int. J. Heat Mass Transf.* **112** 882–90

[5] Raspall F, Velu R and Vaheed N M 2019 Fabrication of complex 3D composites by fusing automated fiber placement (AFP) and additive manufacturing (AM) technologies *Adv. Manuf. Polym. Compos. Sci.* **5** 6–16

[6] August Z, Ostrander G, Michasiow J and Hauber D 2014 Recent developments in automated fiber placement of thermoplastic composites *Autom. Dyn.* **50** 30–7

[7] R. Schledjewski A M 2009 Thermplastic Tape Placement by Means of Diode Laser Heating *International Sampe Symposium and Exhibition.* (Covina, CA: Society for the Advancement of Material and Process Engineering) p 222

[8] Stokes-Griffin C M, Matuszyk T I, Compston P and Cardew-Hall M J 2012 *Modelling the Automated Tape Placement of Thermoplastic Composites with In-Situ Consolidation*

[9] Lamontia M a, Gruber M B, Funck S B, Waibel B J, Cope R D D, Systems A, Drive S and Hulcher B 2003 Developing a Contoured Deposition Head for in Situ Tape Laying and Fiber Placement *Nasa* 1–15

[10] Leon A, Perez M, Barasinski A, Abisset-Chavanne E, Defoort B and Chinesta F 2019 Multi-Scale Modeling and Simulation of Thermoplastic Automated Tape Placement: Effects of Metallic Particles Reinforcement on Part Consolidation *Nanomaterials* **9** 695

[11] Stokes-Griffin C M and Compston P 2015 A combined optical-thermal model for near-infrared laser heating of thermoplastic composites in an automated tape placement process *Compos. Part A Appl. Sci. Manuf.* **75** 104–15

[12] Grove S M 1988 Thermal modelling of tape laying with continuous carbon fibre-reinforced thermoplastic *Composites* **19** 367–75

[13] Louët V Le, Corre S, Boyard N, Delaunay D and Tardif X 2017 Development of an Experimental Bench for Analysing Heat Transfer During the Tape Placement of Carbon / Peek Composites *Iccm 21* 20–5

[14] Szcesny M, Heieck F, Carosella S, Middendorf P, Sehrschön H and Schneiderbauer M 2017 The advanced ply placement process–an innovative direct 3D placement technology for plies and tapes *Adv. Manuf. Polym. Compos. Sci.* **3** 2–9

[15] Madhok K S 2013 *Comparative Characterization of Out-of- Autoclave Materials Made*

By Automated Fiber Placement and Hand-Lay-Up Processes (Quebec, Canada)

[16] da Costa A P, Botelho E C, Costa M L, Narita N E and Tarpani J R 2012 A review of welding technologies for thermoplastic composites in aerospace applications *J. Aerosp. Technol. Manag.* **4** 255–65

[17] Kok T 2018 *On the consolidation quality in laser assisted fiber placement: the role of the heating phase*(University of Twente)

[18] Yakout M and Elbestawi M 2017 Additive Manufacturing of Composite Materials: An Overview Optimization of drilling process View project Additive Manufacturing Fabrication of Lightweight Composites View project

[19] Le Louet Violaine 2018 *Etude du comportement thermique de bandes composites pre-impregnees au cours du procede de fabrication AFP avec chauffage laser* (Universite de Nantes, France)

[20] Zhou Z 2019 Patent Application Publication (10) Pub . No . : US 2019 / 0075021 A1 **1**

[21] Lee, S.-Y., Springer G S 1990 Filament Winding Cylinders: III. Selection of the Process Variables *J. Compos. Mater.* 1344–66

[22] Il, W., & Springer G S 1987 A Model of the Manufacturing Process of Thermoplastic Matrix Composites. *J. Compos. Mater.* **21** 1017–55

[23] Mantell S 1992 Manufacturing Process Models for Thermoplastic Composites *J. Compos. Mater.* **26** 2348–77

[24] H. Sarrazin G S S 1995 Thermochemical and Mechanical Aspects of Composite Tape Laying *J. Compos. Mater.* **29** 1908–1943

[25] Pitchumani R, Ranganathan S, Don R C, Gillespie J W and Lamontia M A 1996 Analysis of transport phenomena governing interfacial bonding and void dynamics during thermoplastic tow-placement *Int. J. Heat Mass Transf.* **39** 1883–97

[26] Sonmez F O and Akbulut M 2007 Process optimization of tape placement for thermoplastic composites *Compos. Part A Appl. Sci. Manuf.* **38** 2013–23

[27] Lemarchand F, Beauchêne P, Laine B and Chinesta F 2007 A Multi-scale Method to Predict Residual Stress Appearance in the Process of on-line Consolidation of Thermoplastic Composites *Int. J. Form. Process.* **10** 471–98

[28] Tierney J and Gillespie J W 2003 Modeling of Heat Transfer and Void Dynamics for the Thermoplastic Composite Tow-Placement Process *J. Compos. Mater.* **37** 1745–68

[29] Sonmez F O and Hahn H T 1997 Modeling of heat transfer and crystallization in thermoplastic composite tape placement process *J. Thermoplast. Compos. Mater.* **10** 198–240

[30] Stokes-Griffin C M and Compston P 2016 An inverse model for optimisation of laser heat flux distributions in an automated laser tape placement process for carbon-fibre/PEEK *Compos. Part A Appl. Sci. Manuf.* **88** 190–7

[31] Kollmannsberger A, Lichtinger R, Hohenester F, Ebel C and Drechsler K 2018 Numerical analysis of the temperature profile during the laser-assisted automated fiber placement of

CFRP tapes with thermoplastic matrix *J. Thermoplast. Compos. Mater.* **31** 1563–86

[32] Hart P E and Hart P 2009 How the Hough Transform Was Invented Editor ' s introduction *IEEE Signal Process. Mag.* 18–22

[33] Davies E R 1988 A modified Hough scheme for general circle location *Pattern Recognit. Lett.* **7** 37–43

[34] Davies E R 1989 Finding ellipses using the generalised Hough transform *Pattern Recognit. Lett.* **9** 87–96

[35] Thomas M 2008 Propriétés thermiques de matériaux composites : caractérisation expérimentale et approche microstructurale *Ec. Polytech. l'Université Nantes* 253

[36] Cengel Y and Boles M 2014 Appendix 1 - Property tables and charts (SI units) *Heat Transf. A Prat. Approach* 992

[37] Liang J 2014 *Experimental measurement and modeling of thermal conductivities of carbon fibers and their composites modified with carbon nanofibers* (University of Oklahoma)

General Conclusion and Perspectives

The primary objective of this thesis focused on the estimation of the thermal property starting from the scale of a single fiber to the actual microstructure of the composite.

The **first chapter** introduced the 3ω method for the estimation of longitudinal thermal conductivity and volumetric heat capacity of a single fiber. Initially, it discussed various approaches present in the literature for the measurement of longitudinal thermal conductivity and the advantages of using 3ω method over other approaches for single fiber. The 3ω method was successfully used in the literature for single fiber, but, the analytical model for the 3ω response of voltage was always simplified in order to apply for estimation of thermal conductivity and heat capacity individually at different frequency ranges. Bringing a new contribution in this field, we focused in this thesis on the measurement of longitudinal thermal conductivity and volumetric heat capacity simultaneously from a single working frequency range. This was made possible by a sensitivity analysis over the wire or fiber-like filament. In this approach, a frequency window was selected where the 3ω voltage response was highly sensitive to small change with the unknown parameters. It showed that the length of the sample controls also the frequency window. For the testing sample chromel wire, carbon fiber type FT300B and FT800H, a length of about 1.5 mm was chosen in such a way that the sensitivity is high in the frequency range of 1-100Hz.

The analytical model from Lu[1] is the outcome of multiple assumptions that motivated the development of a numerical model to check the applicability of the analytical model to our experiments. Under vacuum, the comparison showed a good agreement between analytical and numerical models. The numerical model can take into account convective losses and showed, in this case, a huge drop (1/8) in the value of 3ω voltage response. The quantification of this drop was crucial and needed to be analyzed through experiments. The 3ω method under vacuum was initially validated with the thermal property estimation of a single chromel wire and showed good agreement with the results from the literature. Measurements were also performed for experiments under atmospheric conditions to quantify the influence of convective losses in the thermal property measurement using the analytical model. It showed an increase in the estimated thermal conductivity value by 390% from the literature if the convective loss are neglected under atmospheric condition. It was not possible to quantify the convective heat transfer coefficient *h*. Indeed multiple correlations could not provide enough accuracy on *h* value. In addition, the other alternative which consisted in estimating the *h* values simultaneously with the thermal conductivity was not possible due to strong correlation between the thermal conductivity and heat transfer coefficient. The use of vacuum was therefore shown to be unavoidable.

The thermal properties of two commercial carbon fibers, Toray FT300B and FT800H, were also measured with our 3ω method and were shown to be in good agreement with the data provided

by the supplier. A detailed uncertainty analysis for each known parameter measurement along with the effect of the thermal contact resistance between fiber and sample holder was also provided.

The **second chapter** extended the application of the 3ω method for measurement of thermal conductivity in the radial direction of a single fiber leading to the characterization of the complete conductivity tensor of fibers, well known to be anisotropic materials. The idea was to place the fiber in de-ionized water surrounding to induce radial heat transfer (heat sink effect) while maintaining electrical insulation. The experimental setup was similar to the longitudinal one except that the fiber was placed in the de-ionized water. Initially, a 1D radial analytical model along with a 1D radial finite difference model were developed for this experimental situation. Preliminary results with the experiments and fitting analytical model showed non-accurate fittings thus a non-proper estimation of the radial thermal conductivity. Moreover, the sensitivity analysis showed that the 3ω voltage response was much less sensitive (<0.06) to the radial thermal conductivity than to the longitudinal one. With the help of a 2D heat transfer model, a much better fitting was obtained for the one could not neglect the longitudinal transfer contribution to the temperature measurement. The experimental results for single fiber type FT300B were therefore fitted with the 2D FEM heat transfer model by imposing the longitudinal thermal conductivity obtained from chapter 1 results. The estimated radial thermal conductivity of FT300B carbon fiber was found about 10 times lower than the axial one and showed a much larger scattering due to the smaller sensitivity coefficients. It was also observed that the sensitivity of the voltage measurement to the radial thermal conductivity could be improved by choosing a surrounding medium that would have a higher thermal conductivity.

The **third chapter** focused on effective thermal conductivity calculation at the mesoscale of the CFRC. In the literature, there are theoretical models present that work with various strong assumptions, which is not valid for the real composite. Therefore, numerical homogenization models using the actual microstructure of the material were developed. The bibliographic study showed a choice of the appropriate scale of heterogeneity and the importance of the representative elementary volume and the boundary conditions applied to calculate the effective thermal properties. In this chapter, multiple meshes with different types of distribution of the fibers starting from square packed, random and clustered were studied. Initially, the influence of samples length on the estimation of the effective thermal conductivity tensor for various boundary conditions were analyzed. It was found out that the length of the microstructure also plays an important role depending on the considered direction with respect to fibers and on the chosen type of boundary conditions. Neuman and Dirichlet boundary conditions type were shown to be non-adapted to an efficient determination of effective properties for they induce edge effects whose length may be difficult to predict.

The influence of volume fraction on the effective thermal conductivity were also analyzed that contains the effective thermal conductivity estimation by different theoretical models such as Voigt-Reuss, Hashin-Shtrikmann, Maxwell, and Rayleigh. This was compared with the one estimated numerically by implementation of different boundary conditions. Moreover, the impact of different

fiber distributions no significant change as compared to a square cell. At a bigger scale of the composite such as tapes, the existence and size of a REV was analyzed for different commercial tapes, Solvay and Suprem. This was crucial as advanced manufacturing technique like automated fiber placement (AFP) consider that the tapes are homogenous with linear temperature distribution while heating. It was found out that the Suprem tapes were easily homogenizable due to the good distribution of the fibers in the matrix contrary to the Solvay. Due to the lack of appropriate distribution of the fiber in the composite, scattering of effective transversal conductivity in Solvay tapes were huge and it was to determine the REV. Our study shows the existence of a strong transversal conductivity gradient in the thickness of Solvay that suggests a non homogenizable situation.

The **fourth chapter** focused on the thermal behavior of the tapes during the AFP process as the final laminate of this manufacturing process is highly dependent on its thermal history. In particular, the understanding and mastery of heat transfer at the scale of a single tape alone were essential for better analysis of the composite quality. Initially, meshes in close resemblance with the real tapes (Solvay and Suprem) were generated with the defined heated zones or elements by the laser. Heat source distribution for each mesh was represented. In case of Solvay tape, the heat source distribution was highly dependent on the tape microstructures (non-uniform fiber distribution) contrary to the Suprem tape where it showed rather uniform heat source distribution. A 3D thermal model for the laser heating of a composite tape was established.

The simulation results for temperature distribution through the thickness of the tape confirmed that the maximum temperature was inside the volume of the tape rather than at the surface specifically for Solvay tape. This distribution along the thickness was also highly dependent on the type of microstructure. Additionally, the numerical analysis also showed that the heat transfer had preferential paths that depend on the fiber homogeneity in the composite and degree of contact of the external faces of tapes. Particularly in the study of the Solvay tapes, results showed that the establishment time of the flux at the interface with the steel substrate could be long, as suggested in the experimental work of Violaine Le Louët [2]. Simulation results were also compared to her experimental ones on the same materials. Results for both tapes were consistent with the experimental results during the heating, thus confirming our basic physical assumptions at the microscopic scale. A slight discrepancy was nevertheless observed during the cooling, but this could be due to the fact that there is a loss of fiber fraction during image analysis or simplification of the contact zone or due to the assumption of no reflection during heating.

This thesis focused on multiscale study towards thermal characterization of carbon fiber reinforced composite. The area of this objective is quite vast and yet multiple aspects are remaining that requires further attention in research.

- Microscale: Although in this thesis, the anisotropic thermal conductivity tensor was measured yet the radial thermal conductivity has huge uncertainty in the result. As discussed previously, use of a higher conductivity surrounding medium such as phase change material could result in better measurement of radial thermal conductivity. Moreover, at the microscale, there are local factors such as the interphase of fiber/matrix or contact fiber/fiber that is still needed to be characterized.
- Homogenization at Mesoscale: Homogenization of more complex microstructures such as orientation or interphase contact needs to be done in the future.
- Tapes in Automated Fiber Placement (AFP): Improvement scope is present in terms of similarity of mesh with the real microstructure. A better quality of image could be advantageous in countering the loss of fiber volume fraction. Moreover, the reflection was also neglected in the current tests. The inter-reflection can affect the overall heat source distribution, thus influencing the overall temperature distribution. With the preliminary data of heat source distribution and estimated effective property of the tapes, a simple 1D continuous model can be developed in near future for prediction of temperature distribution in the tape during AFP.

---

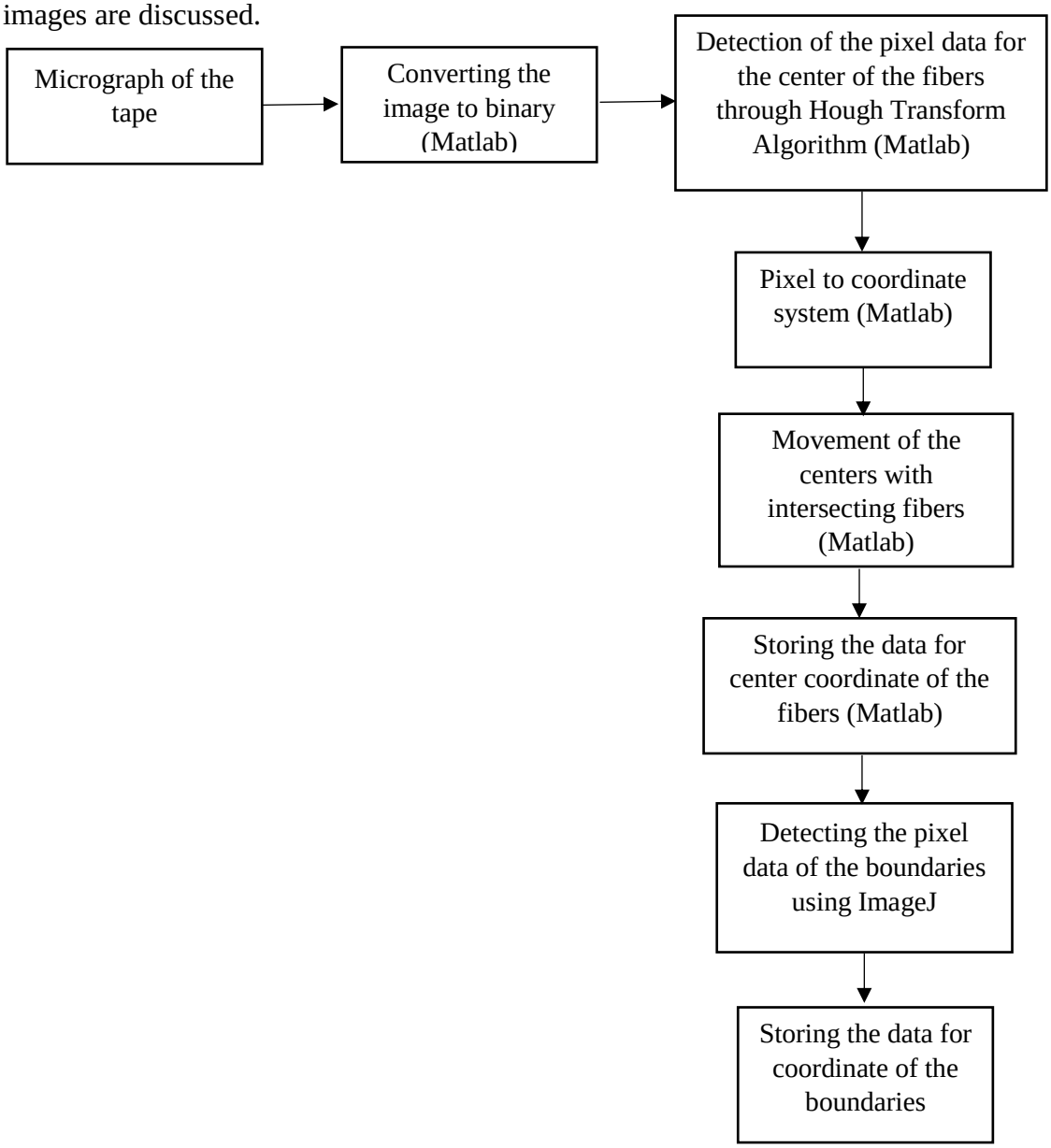
[1] Lu L, Yi W and Zhang D L 2001 3ω method for specific heat and thermal conductivity measurements *Rev. Sci. Instrum.* **72** 2996–3003

[2] Le Louet Violaine 2018 *Etude du comportement thermique de bandes composites pre-impregnees au cours du procede de fabrication AFP avec chauffage laser* (Universite de Nantes, France)

Appendices

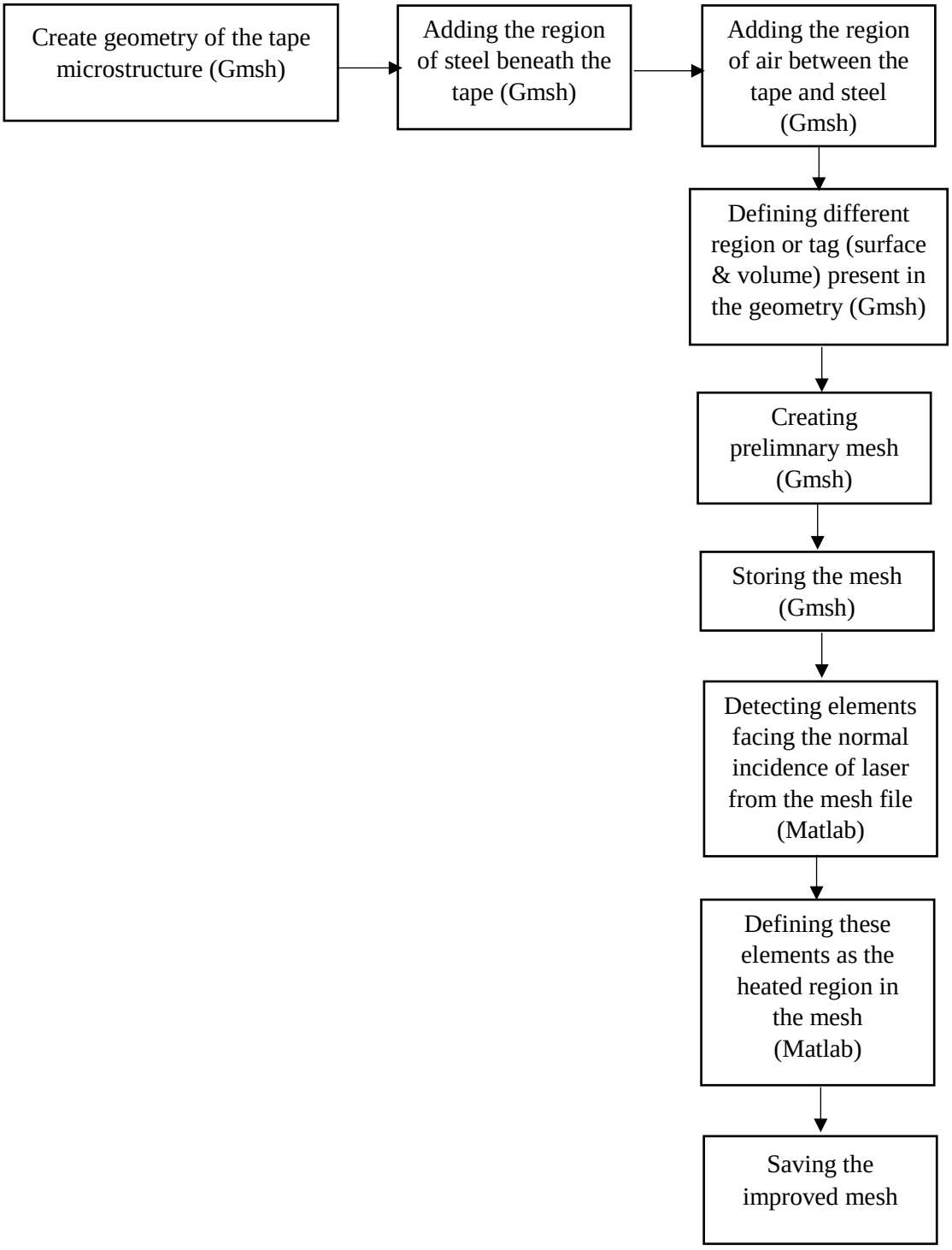
A. Algorithm for Fiber Detection

In this section of appendix, the circular fiber detection from the microscopic images are discussed.



B. Algorithm for Mesh generation

The center position of the fiber and coordinates of boundary points detected by the above algorithm is used to create geometry in Gmsh. After meshing the geometery, the elements hit by the laser (normal incidence) are detected by following algorithm.



UNIVERSITE BRETAGNE SCIENCES LOIRE POUR L'INGENIEUR

UNIVERSITÉ DE NANTES

Titre : De la détermination des propriétés thermiques des fibres à la modélisation multi-échelles du transfert de chaleur dans les composites

Mots clés : la méthode 3ω, conductivité anisotropie, homogénéisation, AFP

Résumé: La prédiction de la conductivité effective des composites nécessitent des informations aux petites échelles et le développement de modèles pertinents. Dans notre travail, la méthode 3ω est utilisée pour estimer la conductivité thermique axiale et radiale ainsi que la capacité thermique volumique de fibres de carbone. En utilisant des modèles analytique et numérique, une analyse de sensibilité est effectuée pour choisir une plage de fréquence de travail appropriée. Une source de courant constante sur la méthode 3ω utilisé pour mesurer la conductivité thermique de chromel et de fibres de carbone de type FT300B et FT800H. Les conductivités thermiques axiales estimées sont en accord avec les valeurs de la littérature. La conductivité thermique radiale estimée pour la fibre de carbone FT300B est 10 fois inférieure à la valeur axial et affiche une incertitude bien plus incertitude bien plus grande en raison de faibles coefficients de sensibilité La conductivité thermique effective a été calculée à l'aide d'une technique d'homogénéisation pour des microstructures avec des carrées uniformes (100 fibres) et bandes de composites (700 fibres). Un modèle thermique 3D est développé pour la simulation de la dépose de bandes chauffées par une source laser dans placement automatique de fibres (AFP). Des maillages adaptés aux microstructures des bandes Solvay et Suprem sont générés. La distribution de la source de chaleur dans le composite au cours de sa fabrication a été calculée. Son influence sur la distribution de la température montre une forte inhomogénéité de la température à l'intérieur de la bande. La température moyenne calculée est comparée aux résultats expérimentaux. Les résultats confirment le besoin de modèles continus spécifiques.

Title : From the determination of thermal properties of fibers to multiscale modeling of heat transfer in composites

Keywords : 3ω method, Anisotropic conductivity, homogenization, AFP

Abstract: The prediction of effective thermal properties of composite requires information at small scale and also appropriate numerical 3D models able to account explicitly the local distribution of fibers. In our work, the 3ω method is used for estimating the axial and radial thermal conductivities and volumetric heat capacity of single carbon fiber. Using analytical and numerical models, a sensitivity analysis is performed for choosing a proper frequency range. A constant current source with differential and lock-in amplifiers are used to measure the thermal conductivity of chromel, and FT300B, FT800H carbon fibers. The measured axial thermal conductivities are in good comparison with the literature values. The estimated radial thermal conductivity of FT300B carbon fiber is 10 times lower than the axial one and shows much larger confidence band due to smaller. sensitivity coefficients. The computation of the effective thermal conductivity by homogenization technique is done for uniform square cell microstructures (100 fibers) along with composite tapes (700 fibers). The effective properties of tapes are interesting for advanced manufacturing techniques such as Automated Fiber Placement (AFP). A 3D thermal model is developed for the tapes heated by a laser source. Meshes in resemblance to the multiple microstructures of Solvay and Suprem tapes are generated. The heat source distribution within the composite during manufacturing is presented and the temperature distribution shows a strong inhomogeneity of the temperature inside the tape. The calculated average temperature is compared with the experimental results. Results confirm the need for specific continuous models.